Title

Unraveling the complex dynamics of energy, water, and carbon fluxes in an irrigated alfalfa field

Permalink

Author

Wang, Tianxin

Publication Date

2024

Unraveling the complex dynamics of energy, water, and carbon fluxes
in an irrigated alfalfa field

By

Tianxin Wang

A dissertation submitted in partial satisfaction of the

requirements for the degree of

Doctor of Philosophy

in

Environmental Science, Policy and Management

in the

Graduate division

of the

University of California, Berkeley

Committee in charge:

Professor Dennis D. Baldocchi, Chair
Professor Manuela Girotto
Professor Lara M. Kueppers

Spring 2024

Unraveling the complex dynamics of energy, water, and carbon fluxes
in an irrigated alfalfa field

Abstract

Unraveling the complex dynamics of energy, water, and carbon fluxes
in an irrigated alfalfa field

by

Tianxin Wang

Doctor of Philosophy in Environmental Science, Policy and Management

University of California, Berkeley

Professor Dennis Baldocchi, Chair

Alfalfa agriculture is a natural laboratory for studying land-atmosphere interactions due to its homogeneity and fluctuating leaf area index from periodic cuttings throughout the year. However, a few problems exist, which are the objectives of this thesis: 1) measuring energy and water fluxes in-situ can be very expensive (~$50K); 2) spatiotemporal heterogeneity could bring in unexpected quantities (e.g., heat and moisture) into the field, distorting the fluxes of energy and water; and 3) long term carbon and water budgets remain largely unknown for irrigated alfalfa in California. In the following, I used a combination of eddy covariance measurements and satellite remote sensing to investigate these problems.

The first chapter is on the development of cost-effective measurements for sensible (H) and latent heat fluxes (λE). I deployed the variance-Bowen ratio technique in an irrigated alfalfa field, and measured H and λE using only a sonic anemometer and an air temperature and relative humidity sensor (T-RH). Measured H and λE were validated against eddy covariance measurements, where H showed strong agreement (slope = 0.98, R^2 = 0.96, n = 3726), while λE showed good agreement (slope = 0.89, R^2 = 0.91, n = 3773). Thermal remote sensing observations from The ECOsystem Spaceborne Thermal Radiometer Experiment on Space Station (ECOSTRESS) and existing tower array showed that the uncertainty in λE was attributed to a product of horizontal heat and moisture advection from upwind fields. Based on our results, the variance-Bowen ratio technique is a robust, inexpensive, yet user-friendly approach to measure sensible and latent heat flux. The utility of this approach could extend to measure horizontal heat advection and provide sensor networks of energy and water fluxes for calibrating/validating remote sensing models.

The second chapter re-evaluated the theoretical limitation of eddy covariance given the spatiotemporal heterogeneity at the site region. Specifically, I focused on the assumed negligible horizontal heat and moisture advection and measured them with tower arrays and profile measurements. Results showed local and non-local processes affected land-atmosphere interactions. Locally, competing process was observed between atmospheric demand and stomatal regulation. As a result of the upwind λE, advection humidified the atmosphere and increased stomatal opening, but λE was suppressed with a lowered atmospheric demand. Non-

locally, spectral analysis revealed that low frequency (i.e., large) eddies contributed high heat and moisture advection. Thermal imagery from ECOSTRESS and Landsat 8/9 showed that these large eddies were generated over the upwind surface, and they were independent of the local boundary layer conditions. Hence, λE was enhanced through this non-local transport of heat and moisture. Lastly, by conditionally including the advective fluxes in the turbulence budget, the energy balance closure improved from 89% to 97% ($r^2 = 0.97$, $p<0.001$) over 37 days.

The third chapter explored how water scarcity affects alfalfa's ability to consistently provide high yields and serve as a robust carbon sink. Long-term eddy covariance data of energy, water, and carbon fluxes were used over the course of 7 years. In 2022, net ecosystem exchange (-175 g C m^{-2} y^{-1}) and evaporation (722 mm y^{-1}) suddenly declined, compared to the average value of net ecosystem exchange at -544 g C m^{-2} y^{-1} and evaporation at 861 mm y^{-1}. This result showed that water stress greatly impacted carbon and water budgets during the active summer growing season in 2022. Specifically, limited water supply from record-low springtime precipitation and irrigation curtailment impeded crop growth, leading to higher stomatal closure and a consequent decrease in carbon sink strength and evaporation throughout this year.

This thesis addressed key challenges in understanding the land-atmosphere interactions in alfalfa agriculture. The simple and cost-alternative sensors developed in Chapter 1 allow researchers to measure fluxes everywhere, all the time across key ecosystems. Missing fluxes quantified in Chapter 2 highlights the significance of advection in land-atmosphere interactions. Lastly, long-term flux budgets assessed in Chapter 3 underscores the vulnerability of agricultural systems.

"I allow myself to fail, I allow myself to break and I'm thankful
for the lessons that I learn."
– Lady Gaga

To Stefani Germanotta (Lady Gaga),

who taught me to fight for my dreams, fiercely and passionately

Table of Contents

List of Figures

Chapter 1 - Handily measuring sensible and latent heat exchanges at great bargain: a test of the variance-Bowen ratio approach

Chapter 2 - How advection affects the surface energy balance and its closure at an irrigated alfalfa field

Chapter 3 - Water scarcity in semi-arid California compromises perennial alfalfa's high yield and carbon sinking potentials

List of Tables

Chapter 3 - Water scarcity in semi-arid California compromises perennial alfalfa's high yield and carbon sinking potentials

Acknowledgement

It seems as yesterday that I joined UC Berkeley for my PhD… Now, four short years later, staring out the Hilgard window in front of my computer, I am surrounded by bittersweet feelings. Perhaps we will save the sadness for another day, and I will say that it has been a memorable journey. This lively campus has enchanted many of us, and I want to thank UC Berkeley for allowing me to explore new opportunities in science and myself. To this day, I owe my gratitude to the many people who have made this a memorable journey.

To mom and dad, who gave me the chance:
Words cannot express my gratitude for your unconditional love, support, and encouragement. As eons shall pass, I could not have asked for more perfect parents!

To my friends who sheltered me countlessly during turbulent times:
Jessica DeGroot, Roby Dorzebach, Michael Odell, Ashely Shaffer, Dr. Grace Carlson, Leonardo Cascão, Marianne Cowherd:
You all have been the fundamental force that provided continuity and serenity in my life. **Jess and Roby**, over the whole spectrum from the happiest moments to some tough stuff, you have given me unparalleled support. **Mike and Ashley**, you two rock, thank you for being authentic, and most importantly, for being brutally honest with me when I needed. **Leo**, you are just outright amazing, and thank you for constantly pushing me outside of my comfort zone. **Grace**, I am so happy for your achievements, and I am grateful for your kindness, empathy, and honesty. **Marianne**, you showed me courage and that fearless optimism. Oh, and few more noteworthy folks: **Kelcey Tern, Sylvain Labedens, Jon Ho**. This has been a fun ride, thank you all!

To colleagues who helped my professional trajectory:
Dr. Kanishka Mallick, Prof. Alexander Knohl, Prof. Ariane Arias-Ortiz, Joe Verfaille, Daphne Szutu, Dr. Martha Anderson, Prof. Yun Yang, Prof. Joshua Fisher
The Biomet people are one of the most inspiring, fun, and exciting groups to work with. **Kanishka and Alex** were always in the lab, we would spend the first half-hour chatting on science and life, and I certainly have learned a lot from both of you; **Ari**, you are just awesome like a ray of sunshine, period. **Joe and Daphne**, you made my research project possible, and I would not be that advection guru without your expertise. **Martha, Yun, and Josh**, I am so happy that we were able to continue collaborating, and I thank you for your guidance and inspiration. I also want to thank **Prof. Whendee Silver, Prof. Manuela Girotto, and Prof. Lara Kueppers** who taught me how to think.

To the legends who shaped me, Prof. Dennis Baldocchi, and Stefani Germanotta (Lady Gaga): these two people are like Rockstars, encompassing the spectrum from academic excellence all the way to altruism. I cannot, EVER, express my gratitude towards the kindness you have bestowed upon me! Perhaps in the end only one of you may read this, but why not?!

My advisor, **Prof. Dennis Baldocchi**, has been a pivotal force for my professional development. From the start of my program, during quarantine era, he has been very attentive with my goals, and his support was unparalleled, which helped me secure the NASA FINESST grant that supported my PhD. From the stupidest to the less stupid questions and countless manuscript drafts, he was patient and encouraging, which helped me learn the lesson of **"go back to first principle and think about the so what of your questions"**. His visionary thinking and commitment, in the **"Physics win, and biology is how it's done"** world, have transformed my view of science that good science can come from the simplest question and curiosity. He led by example and showed me how to be a good scientist, perhaps more importantly he also allowed me to be me, which made me feel the extreme sense of belonging. When I had to deal with some personal issues, he was understanding, open to listening, and encouraged me to take time to get well. We often like to think we have come far with mental health issues with some slogans and statistics, but how on earth can we go beyond this? Undoubtedly, Dennis has been the one that showed up with his actions and leadership. Suffice to say, I am indebted to you, for everything!

Stefani Germanotta, or Lady Gaga, may be the non-orthodox one here. But if you know me, you know her significance in my life. She has been a beacon of hope and support to me (though I have to confess that I am currently listening to Florence + The Machine and Fleet Foxes as I am writing this). At the Chromatica Ball in Fenway, she showed me the beautiful journey from trauma to healing. From her personal experience, she exemplified that it is okay to have feelings, to break, to seek help. She helped me understand that my biggest enemy is me, and my self-worth is determined by me, not by depending on others. And this is oddly my unpopular opinion on her song "Stupid Love", which I see as a liberation of myself from my fears, a celebration of my differences, and a rejoice of shining in my own way. This goes without saying that she also taught me to fight, relentlessly for my passion and the people I care for deeply. She often talks about her inspiration, but perhaps without knowing, she impacted the soul of someone who was struggling, hopeless, and exhausted. **Thank you, Joanne, for your kindness, dedication, and inspiration to me! To this dancefloor I fought for, I will never forget that when life gave me a hundred million reasons to walk away, you helped me see that I am the one good reason to keep on fighting!** So yes, she may not read this, but I need to put this out here, for others who feel as if their head is stuck in a cycle, just as how I used to feel…

Chapter 1 - Handily measuring sensible and latent heat exchanges at great bargain: a test of the variance-Bowen ratio approach[1]

Abstract

Eddy covariance has been the gold standard used to quantify on-farm crop water use and validate evapotranspiration and remote sensing models, but it comes with a high cost. Development of surface renewal allowed cheaper implementations, but it still requires complex data processing. Additionally, the thermocouple used in this method is vulnerable to breakage. With the depleting water resources in the western U.S., there needs to be a method that is cost-effective and simple to quantify water use across wide range of crops. Here, we employed the variance-Bowen ratio approach at an alfalfa site to measure sensible and latent heat flux (λE) using 1) a sonic anemometer and 2) an air temperature and relative humidity sensor (T-RH). The variance-based sensible heat flux, using a sonic anemometer and a T-RH sensor, agreed strongly (slope = 0.98, R^2 = 0.96, n = 3726) with eddy covariance. The modified-Bowen-based latent heat flux (λE_β) also showed very good results (slope = 0.89, R^2 = 0.91, n = 3773) with some uncertainty. We then assessed cases where λE_β performed lesser based on heat advection measurements and remote sensing observations from ECOSTRESS. The problematic λE_β was attributed as a product of the advection of heat and moisture from upwind fields because the assumed equal diffusion of heat and water no longer stands under advection. Overall, our results suggest that the variance-Bowen ratio is a robust, inexpensive, yet user-friendly approach to measure sensible and latent heat flux. Given its cheap price, this approach also has the potential for measuring horizontal heat advection and validating remote sensing models across many different crop types and ecosystems. Furthermore, the inclusion of advection measurement could be crucial in addressing certain remote sensing models (i.e. DisALEXI and PT-JPL) as they systematically omit any advection components.

1.1. Introduction

California, which supports over $50 billion economic value in agriculture (CDFA, 2019), is facing novel challenges to manage its water demand due to the increased interannual variability in precipitation, more extreme droughts, changes in temperatures caused by climate change (Lund et al., 2018; Pathak et al., 2018). In our biosphere, where "everything flows, and nothing abides, everything gives way, and nothing stays fixed" (Heraclitus, ~500 BC), accurate estimation of evaporation remains to be a historical challenge for the hydrology and remote sensing communities (Baldocchi et al., 2019; Fisher et al., 2017).

One of the ways to monitor on-farm water use is through eddy covariance (Alfieri et al., 2018), which uses sonic anemometers (Kaimal and Businger, 1963) and infrared gas analyzers (Auble and Meyers, 1992) to directly measure the trace gases and energy fluxes exchange between biosphere and atmosphere (Baldocchi, 2014; Baldocchi et al., 1988). More specifically for water use, eddy covariance measures the vertical wind velocity and water vapor fluctuations to estimate latent heat flux (Burba and Anderson, 2010). Since this latent heat flux density is representative of the ensemble exchanges of soil and vegetation, the term evaporation is used in this paper when referring to water loss measured by eddy covariance. Based on theory, eddy covariance assumes horizontal homogeneity and steady-state conditions, which neglects the effects of heat and moisture advection (Paw U et al., 2000), but it provides accurate and continuous estimates of heat and trace gas fluxes (Baldocchi, 2020). Yet this gold standard measurement comes at a cost on the order of $25,000 to $50,000 for sensors alone (Hill et al., 2017), a price not everyone could afford, especially considering the additional cost of ancillary data (e.g. net radiation and ground heat flux).

Recent development of surface renewal aimed to address this by specifically targeting the price tag issue (Snyder et al., 1996; Suvočarev et al., 2019). This development enabled the use of only fine-wire thermocouples to derive sensible and latent heat flux (Parry et al., 2019). It can provide desirable results similar to eddy covariance, but notably, the fine-wire thermocouple derived sensible heat flux here is often constrained and calibrated by a coefficient value to derive the actual sensible heat flux. This coefficient value is the regression line against the sonic anemometer measured sensible heat flux, and then the latent heat flux can be calculated as the residual of energy balance (Parry et al., 2019).

As different sites experience varying phenology from management practices (e.g. planting, irrigation scheduling, and cultivars), the coefficient values can be site-specific, which in turn had been reported in literature (Shapland et al., 2014). To address the calibration necessity, two school of approaches emerged as to either employ the similarity theory with surface renewal analysis (Castellví, 2004), or compensate the frequency response of the fine-wire thermocouple (Shapland et al., 2014). Specifically, to avoid the traditional calibration against eddy covariance, Castellvi (2004) estimated calibration coefficient to derive sensible and latent heat flux independently, and this method has been proven possible over a rice field (Castellví et al., 2006) and a peach orchard (Suvočarev et al., 2014). However, this dependency of similarity theory adds another layer of complication for the data processing. Due to the need of a calibration-free procedure, Shapland et al. (2012a, 2012b) proposed a novel approach to represent the flux carrying turbulence without any calibrations under the hypothesis that the small-scale turbulence would be mixed within the larger scale coherent structures. Building upon this

approach, Shapland et al. (2014) used the lag domain to directly compensate the frequency response of thermocouple, and they found good results with reasonable errors within the uncertainty of micrometeorological measurements. Certainly, this approach resolves the calibration need of surface renewal, but not as user-friendly as this still requires in-depth knowledge on ramp characteristics of turbulence and frequency response of thermocouple (Shapland et al., 2014; Van Atta, 1977).

Aside from the calibration, a typical surface renewal setup includes a net radiometer, a sonic anemometer, a fine-wire thermocouple, soil heat flux plates and soil temperature probes (McElrone et al., 2013; Parry et al., 2019). Specifically, fine-wire thermocouples have limitations due to the thermal inertia, radiation error (i.e. solar loading), and sensor vulnerability from breakage (Foken and Bange, 2021; McElrone et al., 2013).

In short, the eddy covariance method offers a direct and accurate measurement of flux exchanges between the biosphere and atmosphere (Baldocchi, 2020), but it is very expensive. Surface renewal operates with a cheaper technique by using fine wire thermocouples (Shapland et al., 2013), but this technique neglects the moisture effect and requires detailed knowledge to derive fluxes independently (Castellví, 2004; Shapland et al., 2014). Evidentially, we seem to have arrived at a crossroad where we have to choose… or maybe standing in the path between the two methods, could there be an alternative measurement that is cost-effective, independent, but also user-friendly?

Originally used in Wesely (1988) to estimate pollutant fluxes (e.g. ozone and sulfur dioxide), the variance and modified Bowen ratio technique offers potential to achieve the objectives for estimating sensible and latent heat flux. However, one important assumption to note is that the modified Bowen ratio still assumes that the source and sink of heat and water are identical (Lindberg et al., 2002; Meyers et al., 1996). In a homogeneous and evaporating surface, heat and water diffusions can be assumed uniform, where the source and sink of scalars are co-located. Under this assumption, studies have shown that there is a strong correlation between the temperature and humidity fluctuations and the corresponding flux carrying eddies (Kustas et al., 1994; Stewart et al., 1994; Weaver, 1990; Wesely and Hicks, 1978). This enables us to estimate fluxes by sampling the variance, the flux-variance method (Tillman, 1972). Here specifically, the flux of heat (F_T) or water (F_q) can be estimated from the standard deviation of temperature (σ_T) or humidity (σ_q), and a more detailed application of this approach is presented in section 2.2.

Behind the novelty of the variance Bowen ratio approach is the obvious yet simple step of storing and collecting variance data, which most meteorological stations discard, but does this simplicity translate to efficiency? Inspired by the variance work for quantifying dry deposition using slow and noisy sensors (Wesely, 1988), and surface renewal that requires fast response data as well as higher order statistics (Shapland et al., 2014), our work seeks the middle ground to use a simple and cost-effective method that can be used for farmlands and provide broad ground truth data for networks, such as OpenET (Melton et al., 2021). In this study, we employ the variance Bowen ratio approach at an irrigated alfalfa site and compare the results with the eddy covariance data. Unlike previous studies, we also discussed the influence of horizontal sensible heat advection on this approach. This provides explicit testing on the use of this

3

approach to obtain sensible and latent heat flux, as well as highlighting the effects of advection on surface energy balance flux measurements in semi-arid environments.

1.2. Method

1.2.1. Site description and data collection

The alfalfa site (Lat: 38.0992, Lon: -121.4993, AmeriFlux ID: US-Bi1) sits on the Bouldin Island, located in the Sacramento-San Joaquin River Delta. Historically, the Delta encompassed ~1,400 km^2 of wetland (Atwater et al., 1979; Cloern and Jassby, 2012) that has been converted to agricultural land over 150 years. The alfalfa site is irrigated with a ditch adjacent to the field, and the soil type at the site is a Ryde-Peltier complex with less than 10% of organic matter.
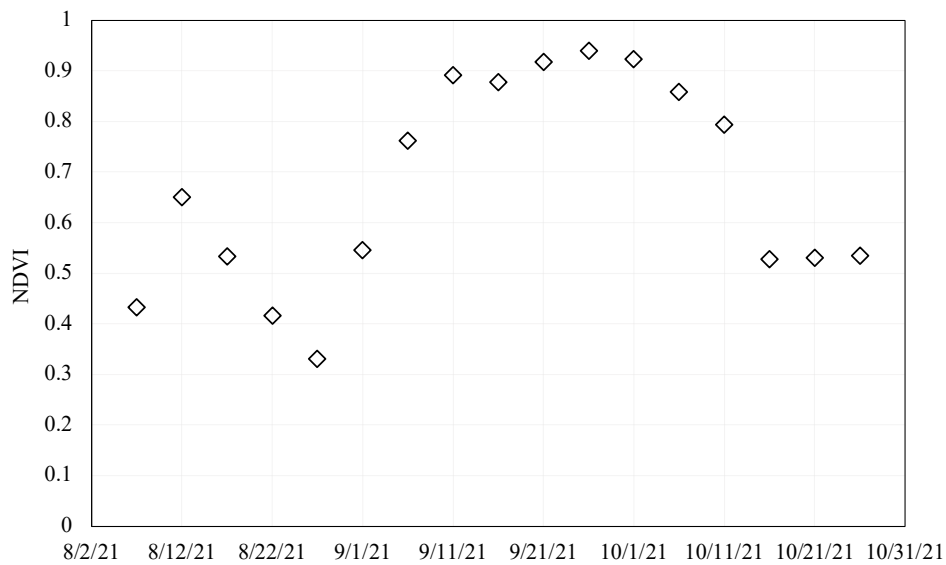
Figure 1. 1. Field averaged NDVI observed by Sentinel-2.

Data was collected at the alfalfa site from Aug 5th to Nov 1st, 2021. On average, the prevailing wind is from the west-northwest region. At this site, the alfalfa goes through periodic cutting throughout the year and grazing in the winter months. During the study, the field went through two cuttings, shown by the Normalized Difference Vegetation Index (NDVI) values measured at the flux tower and observed by Sentinel-2 (Figure 1. 1).

As mentioned before, different agricultural management could initiate different energy exchanges whether locally or regionally. With the help of the remote sensing data from Sentinel-2, we also observed differences in field characteristics between our site and the upwind regions (Figure 1. 2A). Directly upwind (right side of the cyan line), the adjacent alfalfa fields went through different growing stages. Further upwind (left side of the cyan line), the fully grown corn fields (Figure 1. 2A: 2021-08-22) started harvesting gradually (Figure 1. 2A: 2021-09-06 and 2021-09-11). Then, all the corn fields were fully harvested and left bare from 2021-09-16 and onwards (Figure 1. 2A).

Figure 1. 2A. NDVI scenes (10 m) during the study period showing the dynamics of the vegetation status for by the alfalfa site (red) and its the upwind fields. The cyan colored line separates the upwind boundary with alfalfa fields on its right and corn fields on its left. All scenes were generated using Sentinel-2 (surface reflectance) on Google Earth Engine.

At this site, eddy covariance (20 Hz) as well as meteorological data were collected, and the data can be downloaded on AmeriFlux (Site ID: US-Bi1, DOI: https://doi.org/10.17190/AMF/1480317). The sensors used in this study along with their information can be found in Table 1. 1.

Table 1. 1. A table showing the sensors used in this study as well as their location and corresponding data. The (+) sign indicates height above ground and (–) sign indicates depth below ground.

Sensor name	Height (+) or depth (-)	Sampling frequency	Corresponding data
Sonic anemometer (WindMaster 1590)	+3.9 m	20 Hz	Sensible heat flux (H)
Gas analyzer (LI-7500)	+3.9 m	20 Hz	Latent heat flux (λE)
Net radiometer (NR-01)	+2.7 m	0.1 Hz	Net radiation (R_{NET})
Temperature and Relative humidity (HMP155)	+3.5 m	0.1 Hz	Air temperature (T) and relative humidity (RH)
Soil moisture (CS655)	-0.02 m	0.1 Hz	Soil moisture (VWC)
Soil heat flux (HFP01)	-0.02 m	0.1 Hz	Ground heat flux at depth (G_d)
Soil temperature (thermocouple)	-0.02 m	0.1 Hz	Soil temperature (T_{soil})

A 3D ultrasonic anemometer (WindMaster 1590, Gill Instruments Ltd) was used to measure horizontal (u), lateral (v), and vertical (w) wind components on x, y, and z directions, respectively. An open path infrared gas analyzer (LI-7500, Li-COR) was used to measure water vapor molar densities. For high frequency data, we applied a despiking algorithm to filter spikes in all wind components (u, v, w) and the speed of sound with a range 6 times the variance on a 3-minute moving window (Detto et al., 2010, p. 2; Vickers and Mahrt, 1997). Then we performed coordinate rotation where any tilt errors are minimized (vertical axis is orthogonal to horizontal and lateral axis) and the mean vertical velocity is zero (Wilczak et al., 2001). To account for the physical separation distance between the sonic anemometer and the gas analyzer, we computed the time lag to correct for any delays between the two instruments. Additionally, during the sampling period, we removed any fast frequency data associated with rain events.

Alongside of the eddy covariance sensors, meteorological data were collected at 0.1 Hz (once every 10 seconds). An air temperature and relative humidity sensor (HMP155, Vaisala) was deployed to measure air temperature and relative humidity. The HMP155 was housed inside of a fan-aspirated multi-plated shield to represent ambient air condition and prevent solar heating. The net radiation (R_{NET}) was measured with a 4-way net radiometer including the incoming and outgoing components of the shortwave and longwave radiation.

Three ground heat flux plates were buried at 2 cm to measure the heat flux at this depth (G_d). In conjunction, three pairs of soil moisture sensors (VWC) and thermocouples (T_{soil}) were also buried at 2 cm to account for the heat storage between the plate and the surface (G_s) using the calorimetric method (Buchan, 2000; Sauer, 2002). Specifically, the VWC and T_{soil} were used to obtain the volumetric heat capacity (C_{soil}) and time rate of change of the soil temperature ($\partial T_{soil}/\partial t$), respectively (Eq.1 a). Then the average of the three pairs (i.e. G_d and G_s) were computed to obtain the storage corrected ground heat flux (G) in Eq.1 b:

$$G_s = 0.02 \text{ (m)} * C_{soil}(\text{J m}^{-3}\text{ K}^{-1}) * \frac{\partial T_{soil}}{\partial t}(\text{K s}^{-1}) \qquad \text{Eq.1 a}$$

$$G = G_d + G_s \qquad \text{Eq.1 b}$$

One aspect to note is that the soil measurements in our study are buried at a shallower depth compared to Fuchs and Tanner (1968), who recommend a depth between 5-10 cm. For a deeper depth, one must account for storage by knowing the soil temperature, soil moisture, and bulk density at multiple depths. While we do measure soil temperature across different depths, it is challenging to measure soil moisture and bulk density at various depths, especially for long term studies. Additionally, with the storage from the layer above, a deeper depth could be susceptible to heat flux divergence, which may lead to large degree of uncertainty (Fuchs and Tanner, 1968). As a result, the soil heat flux measurements were buried at a shallow depth of 2 cm to obtain the ground heat flux and heat storage.

1.2.2. The variance Bowen ratio technique

From Wesely (1988), there are three emerging variance approaches: 1) a simple standard deviation ratio approach ($F_T = F_q \cdot \sigma_T/\sigma_q$); 2) a correlation coefficient (R_{xx}) approach ($F_T = R_{wT}\sigma_w\sigma_T$ and $F_q = R_{wq}\sigma_w\sigma_q$), where the correlation coefficient is evaluated through atmospheric stability; 3) a normalized standard deviation approach, constrained by atmospheric stability and friction velocity. From these available options, the first approach requires a priori of one of the fluxes, and the last approach requires understanding and knowledge of stability and turbulent statistics, hence, hindering the user-friendly side of operational use.

For the second approach, we can assume a similarity in turbulence exchange coefficients between the two quantities (i.e. $R_{wT} = R_{wq}$), cancelling out the correlation coefficients. Then, we arrive to a formula, where the ratio of the two fluxes (i.e. F_T/F_q) equals to the ratio of the two standard deviations (i.e. σ_T/σ_q). Under the assumption of equal diffusion in heat and water, this approach also represents the modified Bowen ratio approach discussed in Meyers et al. (1996). Once the Bowen ratio is solved (Eq. 3), the moisture correction in Eq. 2 can be accounted for, and the kinematic heat flux is derived as shown in Eq. 4 (Mauder and Foken, 2011; Schotanus et al., 1983).

As shown in Eq.2, The sonic kinematic heat flux ($\overline{w'T_s'}$) includes mixed information on kinematic heat flux ($\overline{w'T'}$), moisture flux ($\overline{w'q'}$), and crosswind flux ($\overline{u'w'}$). Since crosswind corrections are applied internally to modern sonic anemometers, we can then remove the last term in Eq.2.

$$\overline{w'T_s'} = \overline{w'T'} + 0.51 \cdot \overline{T} \cdot \overline{w'q'} - 2\frac{\overline{Tq}}{c^2}\overline{u'w'} \qquad \text{Eq.2}$$

But $\overline{w'T'}$ and $\overline{w'q'}$ are still unknown. While the former can be obtained easily with a temperature sensor, the latter can be obtained via Bowen ratio as:

$$\beta = \frac{H}{\lambda E} = \frac{Cp \cdot \rho \cdot \overline{w'T'}}{\lambda \cdot \rho \cdot \overline{w'q'}} = \frac{Cp}{\lambda} \cdot \frac{r_{wT} \cdot \sigma_w \cdot \sigma_T}{r_{wq} \cdot \sigma_w \cdot \sigma_q} = \frac{Cp}{\lambda} \cdot \frac{\sigma_T}{\sigma_q} \qquad \text{Eq.3}$$

where β is Bowen ratio, λE is latent heat flux, Cp is specific heat of air (J kg^{-1} K^{-1}), ρ is the moist air density (kg m^{-3}), λ is the latent heat of vaporization (J kg^{-1}), w is the vertical wind velocity (m s^{-1}), r is the correlation coefficient, σ is the standard deviation. Assuming a perfect correlation (i.e. equal diffusion) of heat and water (Katul et al., 1995), we cancel out terms into the last term in Eq.3. Then, with algebraic manipulation, we substitute the moisture flux with kinematic heat flux $\left(\overline{w'q'} = \dfrac{Cp}{\lambda} \cdot \dfrac{\overline{w'T'}}{\beta}\right)$, and rewrite Eq.2 as:

$$\overline{w'T'} = \frac{\overline{w'T_s'}}{1 + \dfrac{0.51 \cdot Cp \cdot \overline{\overline{T}}}{\lambda \cdot \beta}} \qquad \text{Eq.4}$$

We used the last term of Eq.3 to obtain the Bowen ratio from the temperature and relative humidity sensor, where the standard deviation of T and q are needed. Since HMP155 outputs temperature and relative humidity, the standard deviation of T was computed directly. For the standard deviation of q, we converted relative humidity to q and then sampled the standard deviation using saturation vapor pressure and measured relative humidity.

1.2.3. Deriving sensible heat flux and latent heat flux

To minimize corrections needed on the variance-Bowen ratio approach, we only applied necessary correction, such as de-spiking and filtering of the rain data. From the HMP155, we sampled the mean air temperature and computed the actual vapor pressure and the density of moist air, ρ (kg m^{-3}). Then we derived sensible heat flux using the moisture accounted kinematic heat flux from Eq.4 as:

$$H_{VB} = \rho \cdot C_p \cdot \overline{w'T'} \qquad \text{Eq.5}$$

from this sensible heat flux using the variance-Bowen approach (H_{VB}), we derived the latent heat flux (λE_{VB}) via the residual of energy balance from net radiation (R_{NET}), ground heat flux (G), and H_{VB}:

$$\lambda E_{VB} = R_{NET} - G - H_{VB} \qquad \text{Eq.6}$$

Alternatively, one could also employ the Bowen ratio to solve for λE (Fritschen, 1966) without the need of fast frequency data. With the goal to develop an independent and user-friendly measurement, we also included λE computed using the modified Bowen ratio as shown in Eq. 3. To re-elaborate, aside from the need of R_{NET} and G, the modified Bowen ratio computed λE (λE_{β}) only required data from the temperature and relative humidity sensor, which was sampled at 0.1 Hz:

$$\lambda E_{\beta} = \frac{R_{NET} - G}{1 + \beta} \qquad \text{Eq.7}$$

This computed λE_{β} eliminates the need of having any profile measurements required by the traditional Bowen ratio setup. Hence, one can obtain this Bowen ratio by simply sampling the standard deviation of T and q (Eq.3) from the HMP155. Additionally, the Cp and λ (Eq. 3) can also be computed with the same sensor, making it possible to obtain the λE_{β} without a sonic anemometer. Therefore, this could be a simple, yet far more affordable setup for ranchers. A script can be found in Appendix A for applying the variance Bowen ratio approach.

It is important to note that although there are advantages to this approach, the Bowen ratio method is not commonly used nowadays to estimate H and LE due to its assumption that the source and sink of heat and water is identical.

1.3. Result

1.3.1. Quality assurance of eddy covariance data
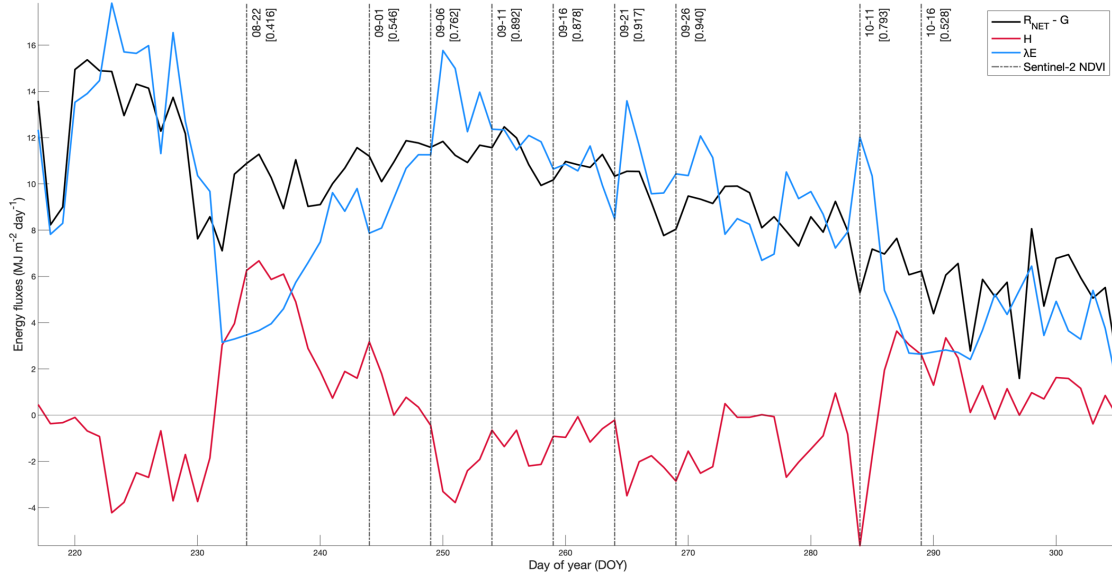
Figure 1. 2B. Daily integrated sensible and latent heat flux from eddy covariance along with the net available energy ($R_{NET} - G$) from DOY 217 to 305. The vertical lines indicate Sentinel-2 overpasses (~10:30 AM) and NDVI values shown in Figure 1. 2A.

Given the dynamics of the field characteristics, sensible (H) and latent heat flux (λE) from eddy covariance exhibited a wide range of values, cycling through growing season, cutting, and regrowth (Figure 1. 2B). On Aug 22nd, the recently mowed field (NDVI = 0.42) allowed more H to be transferred than λE. Through Sep 6th (NDVI = 0.76), as the vegetation started to develop, H began to decline while λE increased. At peak growing season on Sep 26th (NDVI = 0.94), H directed downward while λE exceeded the net available energy. This anomaly might indicate that the surface extracted sensible heat energy from the boundary layer to drive more latent heat, and this dynamic will be explored more in Section 4.2. Considering the observed dynamics with the vegetation height, measurement height, sensor path-length, and sampling rate, cospectral filtering of w'T' and w'q' may be possible (i.e. covariance or flux loss). To evaluate this and ensure the quality of the fluxes, we computed and examined the mean cospectra via spectral analysis (Alfieri et al., 2022; Baldocchi and Meyers, 1988). In Figure 1. 3, we normalized the cospectra of temperature and humidity by their total covariance (i.e. nSwT(f)/w'T', nSwQ(f)/w'q'). Then the normalized cospectra of each scalar was plotted against a non-dimensional frequency where the natural frequency (n) is multiplied by the height above the zero-displacement height (z-d) and then normalized by the wind speed (i.e. n(z-d)/U).

9

The cospectra of vertical wind component and temperature (i.e. sensible heat flux) nearly matched with the ideal spectra from the Kansas experiment (Kaimal et al., 1972), indicating that the measured sensible heat flux was accurate (Figure 1. 3 – top). For the cospectra of moisture
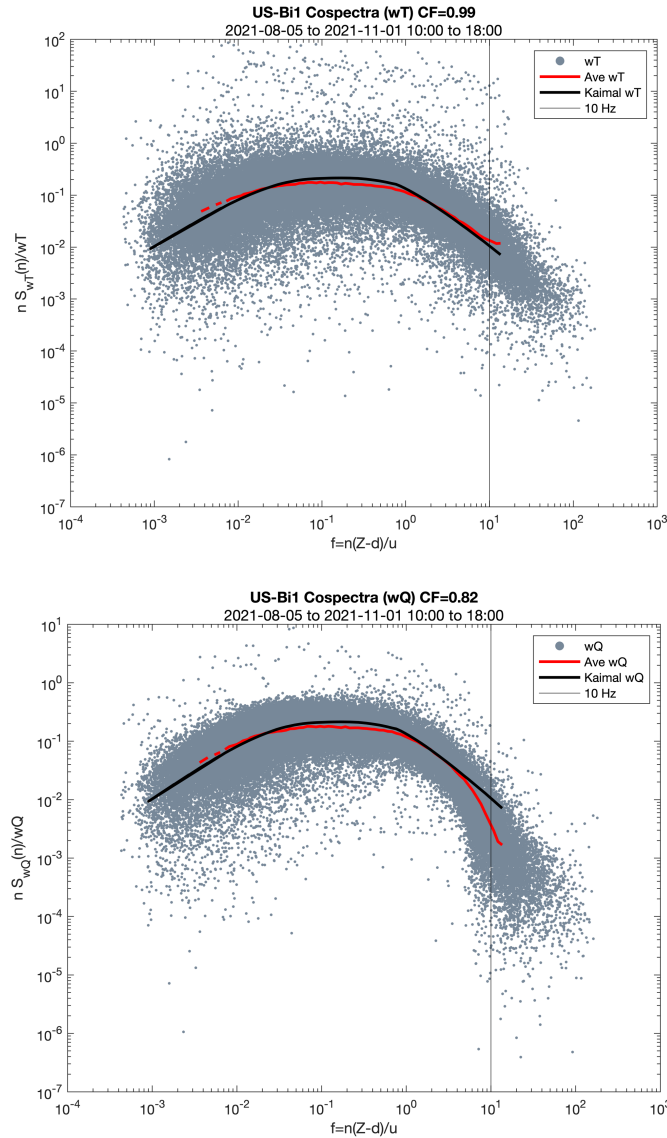
Figure 1. 3. The 10:00 to 18:00 cospectra plots for the vertical velocity component and scalar of temperature (top) and moisture (bottom) from the zero-plane displacement height (d) to the measurement height (z). CF indicates the correction factor. The data on Sep 3rd was omitted due to memory card issue.

flux (Figure 1. 3 – bottom), there was noticeable cospectral loss in the inertial subrange, indicating an underestimation of the λE was present. This underestimation was in fact attributed to the sensor's limitation due to factors including finite path-length and frequency response (Wolf and Laca, 2007). To address the attenuation of the fluxes, especially at the high frequency, a correction factor, taken as the ratio between the area under the curve of the measured and ideal cospectra, was applied. This procedure is also known as spectral correction with transfer function (Foken et al., 2012; Moore, 1986; Su et al., 2004). Because the ideal cospectra of moisture flux is

not well established, the ideal cospectra of sensible heat was used as the reference assuming a cospectral similarity between the heat and moisture fluxes (Massman, 2000). The transfer function was applied to both heat and moisture fluxes to spectrally correct them.

1.3.2. Sensible heat flux
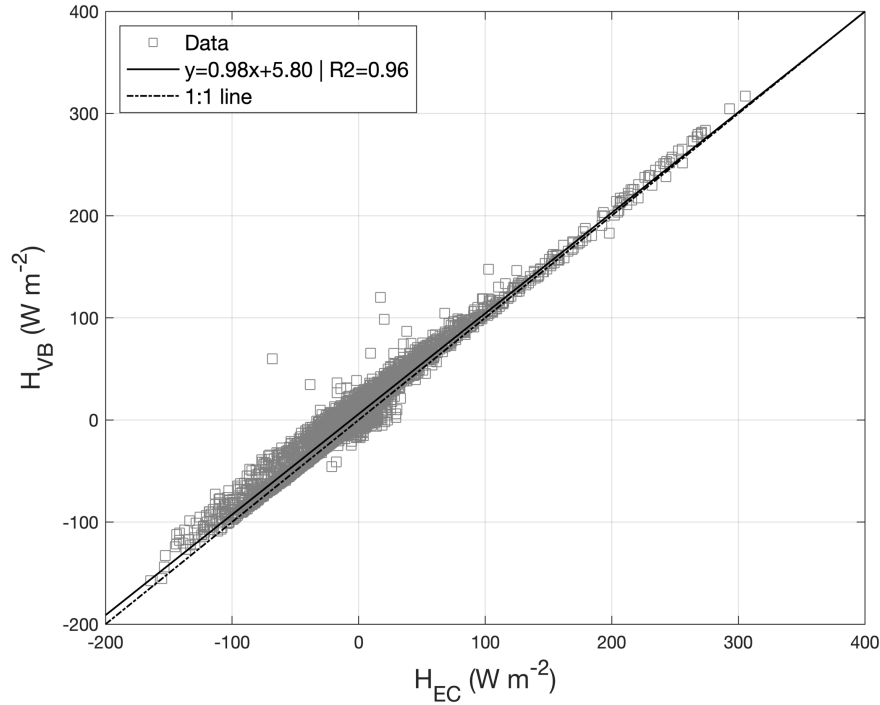
Figure 1. 4. Comparison between sensible heat flux computed by the variance-Bowen ratio method compared and measured by the eddy covariance (n = 3726, p<0.001). H_{EC} had spectral correction applied. The geometric mean regression (not shown) is: y=1.00x+5.89;

Figure 1. 4 shows the linear regression between the sensible heat flux computed with the variance-Bowen ratio approach (H_{VB}) and measured by eddy covariance (H_{EC}). The slope between the two variable (n=3726) was not significantly different from than 1 (R^2=0.96, p<0.001), indicating the very strong relationship. The root mean squared error (RMSE) was 11.5 W m^{-2}, further showing that the variance-Bowen ratio approach performed well in measuring sensible heat flux. Upon further inspection, one may notice few scattered outliers. For example, on Sep 23rd at 17:30, where the net available energy was already at -35.2 W m^{-2}, the H_{EC} was around -70 W m^{-2} while the H_{VB} was still positive at around 60 W m^{-2}. Although the exact cause was unknown, this highlighted that the sonic kinematic heat flux governed the sign of H_{VB} as shown in Eq. 4 and 5. Hence, further data filtering (i.e. step change detection) on $\overline{w'T_s'}$ should be considered to address the sudden sign flip. Nonetheless, the variance-Bowen ratio displayed potential to be used as an independent measurement of H.

1.3.3. Latent heat flux
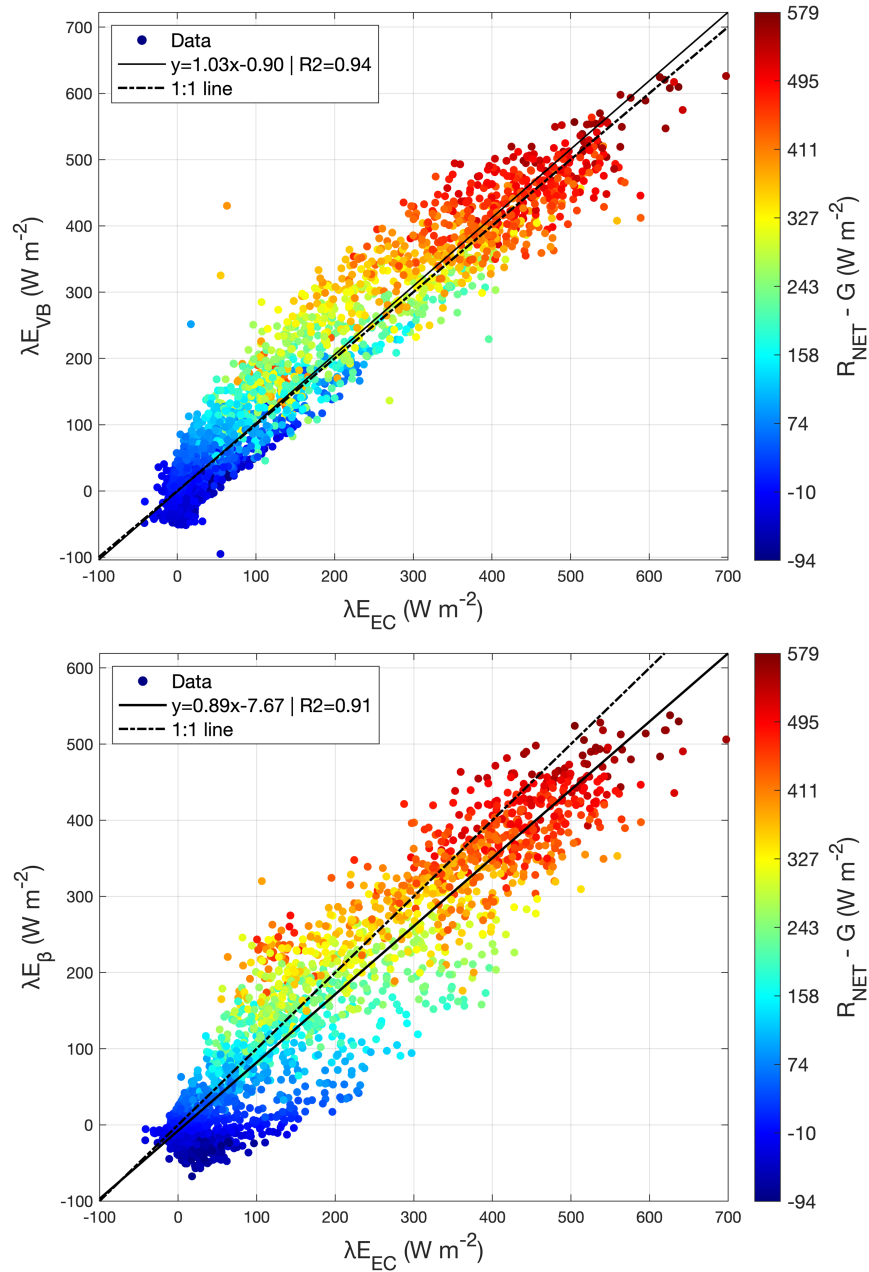
Figure 1. 5. (Top) Comparison between latent heat flux computed by the residual of energy balance vs. measured by the eddy covariance (n=3726, p<0.001). The geometric mean regression (not shown) is: y=1.07x-4.24; (Bottom) Comparison between latent heat flux computed by the modified-Bowen ratio vs. measured by the eddy covariance (n=3733, p<0.001). The geometric mean regression (not shown) is: y=0.94x-12.23.

Latent heat fluxes were computed following Eq. 6 and 7 using the energy balance residual (λE_{VB}) and modified-Bowen-ratio (λE_β). Linear regression of each derived half-hourly λE was plotted as a function of the net available energy to assess the performance (Figure 1. 5). On average, the λE_{VB} performed very well (R^2=0.94, p<0.001) compared to the spectrally corrected λE measured by eddy covariance (λE_{EC}) with a 3% overestimation and an RMSE of 39.9 W m^{-2}

12

(Figure 1. 5. Top). λE_β underestimated λE_{EC} (R^2=0.91, p<0.001), on average, by ~11% with an RMSE of 49.5 W m^{-2} (Figure 1. 5. Bottom). Based on Eq. 6 and 7, the net available energy fluxes (i.e. R_{NET} – G) govern the computed λE, which can be seen in Figure 1. 5 as the pattern of λE followed the low to high transition of the net available energy. For λE_{VB}, a visible hump was observed above the regression line, while a more tailored pattern was observed below the regression line. Interestingly, λE_β exhibited a symmetrical pattern with a mix of overestimations and underestimations, but noticeably with a larger magnitude of underestimations.

1.4. Discussion

1.4.1. Spectral correction and energy balance closure
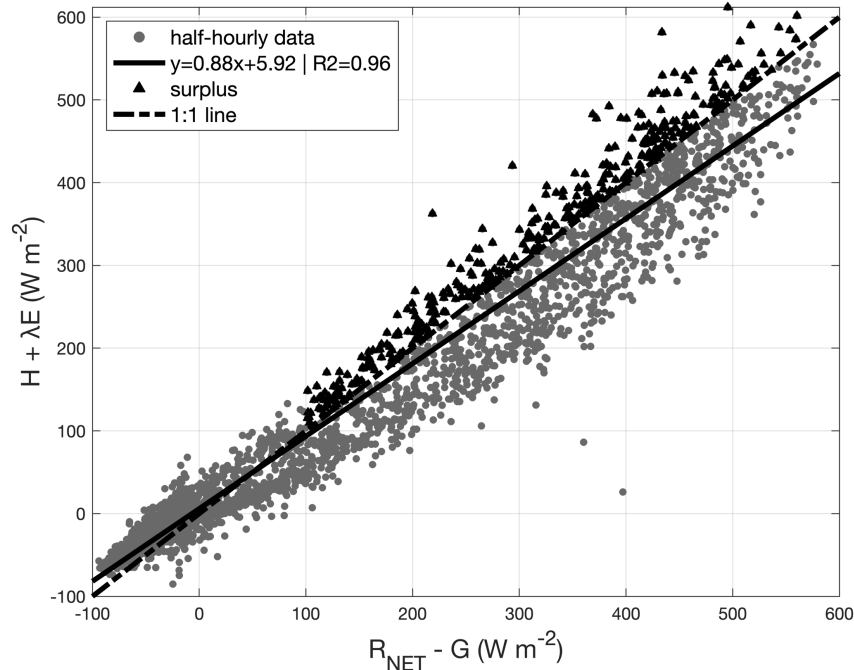
Figure 1. 6. Half hourly energy balance closure from the study period (n=4161, p<0.001). The black points indicate when the turbulent energy exceeded the net available energy (n=370, p<0.001), and the minimum threshold of the net available energy is 100 W m^{-2}. The geometric mean regression (not shown) for the entire half hourly data is: y=0.90x+3.83.

By employing a spectral correction, we improved the energy balance closure greatly with the slope increased from 0.73 to 0.88 (R^2=0.96, p<0.001), however, there was still a lack of closure (Figure 1. 6). One point to emphasize on is that based on the spectral analysis (Figure 1. 3), the forced closure method (Twine et al., 2000) should be considered inappropriate in our study as the sensible heat flux was measured accurately (see Figure 1. 3. Top). In our case, λE did need adjustment but specifically for mechanical reasons due to the known spectral loss instead of the ad hoc energy balance closure.

In Figure 1. 6, the highlighted surplus (n=370, p<0.001) indicated periods when the turbulent energy exceeded the net available energy. In general, a system cannot consume more energy than the amount it was given. Previous literature had also identified and attributed this problem from advection, the horizontal transport of heat or moisture (Philip, 1959), which can enhance

evaporation to a degree exceeding the net available energy (Wang et al., 2021; Baldocchi et al., 2016; Philip, 1987; Prueger et al., 1996; Tolk et al., 2006; Verma et al., 1978). Why is this normally assumed negligible quantity ubiquitous? And how does advection affect λE_β?

1.4.2. Advection and latent heat flux

Warm and dry air flowing over an actively evaporating surface can further enhance the evaporation (Philip, 1987), via an oasis effect. Under non-advective conditions with large fetch, eddy covariance provides higher data quality as the neglected horizontal component is often compensated by the field homogeneity (Gash, 1986; Foken and Wichura, 1996). However, agriculture sites in the Central Valley of California have a spatiotemporal mosaic pattern with alternating dry and wet fields, which can induce higher water loss through the advection of sensible heat (Blad and Rosenberg, 1974; Philip, 1959; Rosenberg and Verma, 1978; Tolk et al., 2006). In ways, the assumed homogeneous individual fields could construct a mosaic pattern with other fields, further encouraging the horizontal movement to be considered.
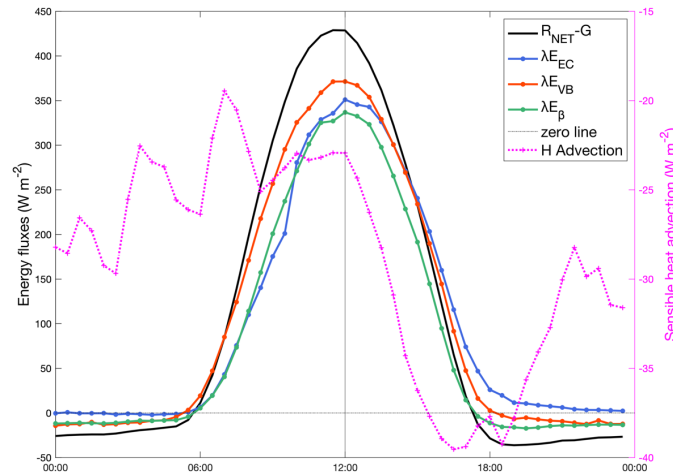
Figure 1. 7. Diel cycle of net available energy (solid black), spectrally corrected λE from eddy covariance (blue), λE computed through energy balance residual with the variance-Bowen ratio approach (red), and λE computed with modified Bowen ratio (green). Diel cycle of the sensible heat advection is on the secondary axis in pink.

Since sensible heat advection using the variance-Bowen ratio approach was also collected during the study period, we have included heat advection as a complementary data to illustrate its impact on λE. During the study period, heat advection was present, and the magnitude of advection started to increase after 12:00 local time. Simultaneously, all measured λE from different ways started to gain additional energy as they approached the net available energy, especially for λE_{VB} and λE_{EC}, indicating the enhanced evaporation (Figure 1. 7). The enhancement was further amplified after 15:00 when λE_{VB} and λE_{EC} exceeded the net available energy when the magnitude of advection was greater than -35 W m^{-2}. As hot and dry air began to be advected into the field, the crop surface started evaporating to prevent surface warming. This then creates an internal boundary layer, allowing more heat extraction from the layer above to enhance the local evaporation. Finally, this leads to a larger temperature gradient to induce more heat advection, creating a positive feedback. The process then came to an end as the sun started setting and the power of the evaporative cooling diminished. It is worth to also note that our case

may have had two different types of advection with one as the horizontal heat and the other as the vertical heat extraction (i.e. flux divergence) due to the internal boundary layer.

Although λE_{VB} demonstrated a very strong relationship (Figure 1. 4), in a diel cycle, it overestimated λE until 13:30. For λE_β, it aligned well with λE_{EC} prior to noon, then it started to lag without experiencing much of the enhanced evaporation compared to λE_{VB} and λE_{IRGA}. But how come the modified-Bowen ratio approach failed to reflect the magnitude of the enhancement? In the following, we explored the dynamics among λE_β, λE_{EC}, and heat advection. Additionally, given that thermal infrared signals can reflect latent heat (Anderson et al., 2012), we also paired the in-situ measurements with ECOSTRESS to inferentially diagnose and verify
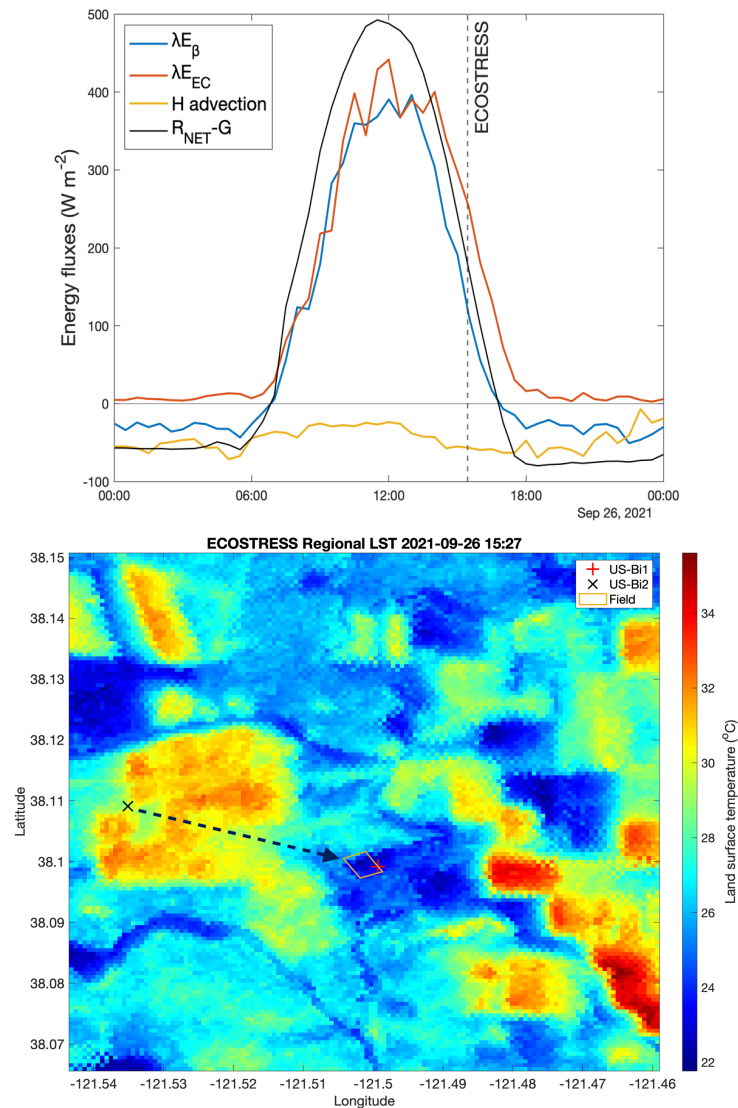
Figure 1. 8. (left) half-hourly energy fluxes of λE_β(blue), λE_{IRGA}(orange), sensible heat advection (golden), and net available energy (black). The vertical dashed line marks the ECOSTRESS overpass; (right) ECOSTRESS LST scene on 2021/09/26 at 15:27 local time. This scene includes the alfalfa site (red cross), the corn site (black x), and the predominant wind direction (dashed black line). PhenoCam: https://phenocam.sr.unh.edu/webcam/browse/bouldinalfalfa/2021/09/26/

15

the advection (i.e. heat and moisture). Specifically, we used the land surface temperature (LST) observations from ECOSTRESS at overpasses (Fisher et al., 2020).

1.4.2.1. Sensible heat advection

On Sep 26th, we observed a surplus of λE_{EC} exceeding the net available energy at 14:00. This also corresponded with the measured sensible heat advection, which reached around - 42.9 W m^{-2} at the same time and increased (magnitude) afterwards (Figure 1. 8 – left). To clarify the direction, the negative sign means the energy was directed downwards, adding additional heat into the surface to enhance evaporation. On this day, the field-averaged NDVI value of 0.94 (Sentinel-2) and the PhenoCam images (link in Figure 1. 8's caption) indicated that the field had a high canopy density, serving as an oasis absorbing the heat energy advected from upwind fields. Leveraging with ECOSTRESS LST, we were able to further visualize the oasis effect from space (Figure 1. 8 - right). At 15:27, from the corn site (black x) to the alfalfa site (red cross), we observed a large temperature gradient extending from ~32 °C to ~23 °C. The LST observation could indicate the potential sensible heat advection, but it alone cannot prove the advection. In fact, the enhancement in λE_{EC} may also be a product of the vertical flux divergence. However, without flux measurements at multiple levels, it is challenging to confirm the underlying advection. Nonetheless, the LST observation here offers a unique way to provide insights for our flux measurements that the measured heat advection was present at the time and could have caused the enhancement in evaporation.

Given that λE_{β} was calculated via a forced closure technique (Eq. 7), one unanswered question is why did λE_{β} fall behind of λE_{EC} on this day? Under advective conditions, especially for sensible heat advection, studies have shown that Bowen ratio technique performed poorly as a result that the assumed similarity between heat and water no longer stands (Blad and Rosenberg, 1974; Gavilán and Berengena, 2006). Lang et al. (1983) found that the ratio of eddy transfer coefficient for heat and water decreased as the atmospheric stability increased under advection. In Warhaft (2000, 1976), the disunity of the coefficients was found under advected heat and moisture. Studies also showed that latent heat flux evolved with the downwind distance under advection, in which the surface resistance and available energies differed from the field boundary to the uniformed regions (McNaughton, 1976a, 1976b; McNaughton and Black, 1973). In our approach, we calculated the Bowen ratio from σ_T and σ_q (see Eq. 3), but under advection the assumed equal similarity breaks (Lang et al., 1983). Derived from Eq. 7, under heat advection, σ_T would be greater than σ_q, resulting a larger Bowen ratio which lowered the λE_{β}. As a result, λE_{β} underestimated the enhanced evaporation as the sensible heat advection exacerbated.

1.4.2.2. Moisture advection
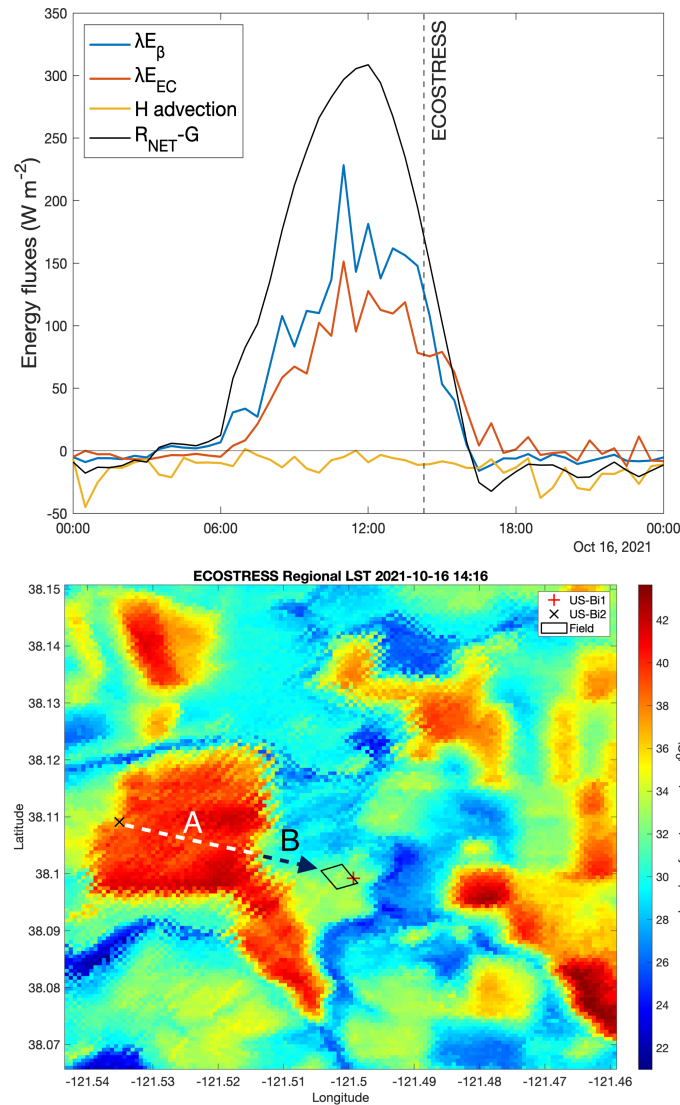
Figure 1. 9. Same as Figure 1. 8 but for Oct 16th, 2021. The ECOSTRESS overpass was at 14:16.

Since only heat advection was measured in our study, can we use the relationship of σ_T and σ_q to infer moisture (i.e. latent heat) advection as well? If moisture advection was present, σ_T would be less than σ_q, resulting a smaller Bowen ratio that would increase the λE_β. This hypothesis is valid on Oct 16th, where λE_β surpassed λE_{EC} (Figure 1. 9 - left).

Linking the in-situ measurement with ECOSTRESS LST (Figure 1. 9 - right), we saw a temperature gradient, where the entire region by the corn field (region A) had a high temperature beyond 38°C, region B had a cooler temperature (~29°C), and the alfalfa field was warm (~33°C). If we used the same concept as Figure 1. 8, we should have observed high sensible heat advection, however, our advection measurement suggested otherwise in Figure 1. 9. Looking at the upwind fields in region B, they had a relatively higher NDVI value of ~0.70 (Sentinel-2) and were cooler, inferring that these fields may have received heat advection to enhance

17

evaporation. Then, the evaporating fields from region B may have supplemented cool and moist air into our alfalfa field. As a co-located process, this moisture advection may have muted the effect of the heat advection. However, due to that moisture advection was not measured in this study, we cannot confirm this hypothesis. Nonetheless, the LST observation still could be used to serve as a secondary insight that may be helpful to indirectly diagnose the field condition. This also highlights the need to also include measurement of moisture advection to capture the co-located processes in future experiments.
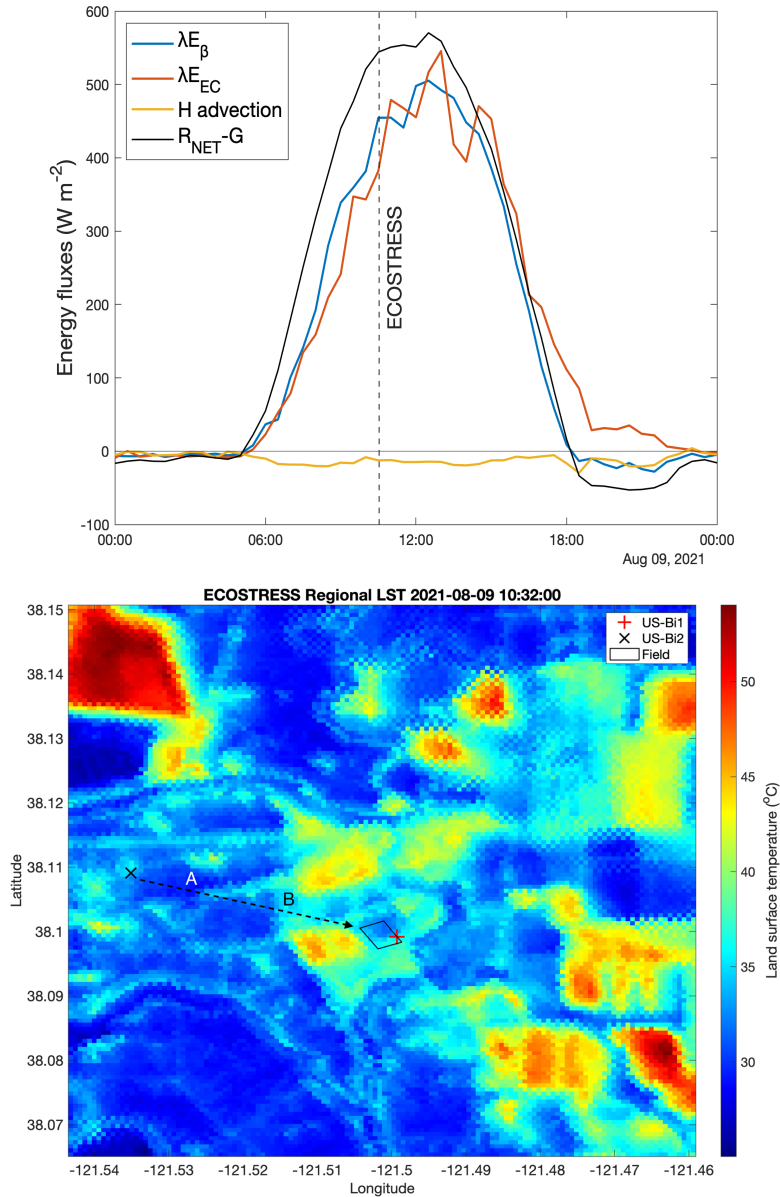
Figure 1. 10. Same as Fig. 8 but for Aug 9th, 2021. The ECOSTRESS overpass was at 10:32.

Another unanswered question is why did neither λE exceed the net available energy as similar to what we saw in Figure 1. 8? Unfortunately, the PhenoCam had logging issues since Oct 8th, and we were not able to visually inspect the field condition. However, compared to the full canopy case presented in Figure 1. 8, here, the low NDVI of 0.53 (Sentinel-2) suggested less water

would be evaporated in a developing field. Additionally, the available energy was already low in Fall with a max at ~300 W m^{-2}, further indicating the low potential evaporation at the site.

What happens in a more active growing season with sufficient energy supply? Noticeably on Aug 9th, even when heat advection was minimal throughout the day, λE_{EC} still exceeded the available energy while λE_{β} was almost identical to the available energy after 15:00 (Figure 1. 10 - left). At ECOSTRESS overpass (Figure 1. 10 - right), λE_{β} was already ~50 W m^{-2} greater than λE_{EC}. Thus, at least during this overpass, the relationship of σ_T and σ_q can be used to infer moisture advection. During this time, the upwind fields had some temperature differences where, along the transect from A to B, the temperature transitioned from cool (~31°C) to warm (~36°C) before reaching the alfalfa field (~33°C). Because moisture advection was not directly measured in this study, we are not sure of the exact cause. But, using the satellite LST observation as a start, the already cool and evaporating upwind fields might become even cooler as the available solar energy increased throughout the day. Then the additional moisture could be advected into the alfalfa site, resulting a surplus of λE. Furthermore, given the low measured heat advection during the day, we are inclined to suspect that moisture advection might have caused this surplus. One may ask why the heat from region B did not get advected into the field? It probably did, but the advected moisture from region A may have outweighed the heat, resulting more of a regional scale moisture advection.

1.4.3. Other considerations

1.4.3.1. Slow sampling rate of the modified-Bowen ratio technique
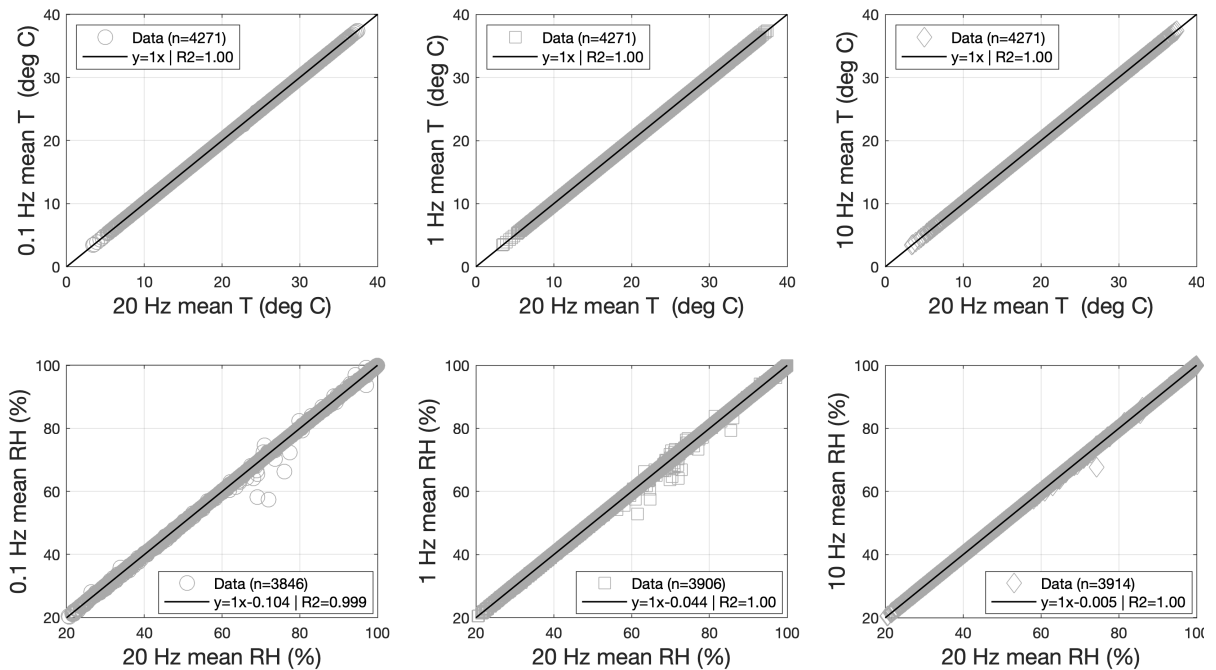
Figure 1. 11. Comparison of the standard deviation of air temperature (top) and relative humidity (bottom) between resampled frequency (0.1, 1, and 10 Hz) and the native measurement frequency (20 Hz).

As shown in Figure 1. 3, even with the fast frequency measurement at 20 Hz, there were underestimations of fluxes, especially for water. If we were sampling at 10 Hz, there may have been more unsensed fluxes. More importantly, should this concern the modified-Bowen ratio technique, which operated on a far slower frequency at 0.1 Hz? To test this, we resampled the 20 Hz air temperature and water vapor molar density data from the infrared gas analyzer into slower frequencies at 10, 1, and 0.1 Hz. The air temperature was used to compute the standard deviation (Figure 1. 11, top), and the water vapor molar density was converted into relative humidity (Figure 1. 11, bottom). Compared to the 20 Hz data, the standard deviation of the air temperature for all the resampled data agreed strongly (Figure 1. 11, top). Similarly, all resampled relative humidity agreed very strongly with the 20 Hz data (Figure 1. 11, bottom). The strong agreement of variables between the slower frequency (i.e. 0.1, 1, and 10 Hz) and the high frequency (i.e. 20 Hz) further proved that very low bias was presented with the 0.1 Hz modified-Bowen ratio technique in our study.

1.4.3.2. Affordability and applications

As writing this paper, heat and drought continued to scourge through California, and irrigate the right amount (i.e. precision agriculture) had never been so pressing. To tackle this, we could expand current sensor network and/or use satellite remote sensing models (i.e. OpenET Melton et al., 2021) to advise on-farm water management. Both approaches should be regarded as complementary because in-situ measurement provides validation, while satellite observation provides a broader view of the underlying issues. Currently, among the 574 registered AmeriFlux sites, there are only 66 continuously operating agricultural sites (10 in California). Based on our study, the variance-Bowen ratio system could be used to increase observation and validation.

Table 1. 2. An illustration of cost and list of sensors required in eddy covariance (*) and variance-Bowen ratio (†) system. The price was obtained from Campbell Scientific. Note that some sensors can be replaced with others (e.g. Gill Windmaster instead of CSAT3B). Additionally, this table does not include other configuration costs, including logger, sensor cable lengths, solar panel, power supply, enclosure, tripod, and crossarms. Note that a data logger is also needed for setup, and depending on the needs (e.g. sampling frequency and sensors), the logger could cost from $1,500 to 2,800.

Measurement	Sensor	Quantity	Price (per item)
Soil moisture * †	CS650	2	$247.70
Soil temperature * †	TCAV	2	$331.20
Soil heat flux * †	HFP01	2	$746.88
Net radiation * †	CNR4	1	$9,500.00
Temperature and relative humidity * †	HMP155	1	$766.08
Sonic anemometer * †	CSAT3B	1	$8,990.40
Sonic and gas analyzer *	IRGASON	1	$23,247.84

Compared to an eddy covariance setup, which can easily cost ~$36,165.48, the variance-Bowen ratio system is 60.5% cheaper at a cost of ~$21,908.04 (Table 1. 2). But this is still a steep price considering that other equipment is also needed. Plus, agricultural management involves many activities that could impact field sensors, ranging from sprinkler irrigation to tractor tilling,

discing, or spraying. Thus, all these activities require a minimalist system, and it is necessary to further simplify the variance-Bowen ratio approach. One option is to build the net radiometer and heat flux plates in house. The net radiometer could be constructed using polystyrene foam and type T thermocouple (Da Ros Carvalho et al., 2021) and the soil heat flux plates could be replaced with Peltier chips (Weaver and Campbell, 1985). Together, this would bring down the cost for these two sensors to less than $100. Alternatively, to eliminate the needs of net radiometer and ground heat flux measurements, a modeling scheme of the net available energy should be considered in the future to cut down the cost to ~$9,756.48 (Table 1. 2. CSAT3B and HMP155). For example, procedures from Mallick et al. (2015) could be implemented to replace the net available energy component, but the temporal resolution would need to be daily. Lastly, if a site experiences no advection, one could even remove the sonic anemometer and cut down the price to ~$766.08 with only a HMP155 to obtain the latent heat flux.

Aside from expanding the variance-Bowen ratio approach, its performance should also be tested across different crop types and ecosystems to assess its sensitivity and flexibility. Nevertheless, with the cost-effectiveness of this approach, we also presented opportunities for measuring advection, especially for heat. However, advection is a co-located process, where a site experiencing heat advection would also experience moisture advection as shown in Section 4.2. However, moisture advection remains to be a less researched area that requires attention in future studies.

Lastly, as nowadays, satellite-based irrigation is becoming more available through remote sensing models (Anderson et al., 2011; Fisher et al., 2008), for instance, the Disaggregated Atmosphere-Land Exchange Inverse flux (DisALEXI) and the Priestly-Taylor Jet Propulsion Laboratory (PT-JPL). Validation remains to be a demanding, yet necessary step for satellite-based models. To ensure the accuracy of these models under advective conditions, further research should be done in terms of how advection affect DisALEXI and PT-JPL as well as how to account for advection using remote sensing observations.

Together, we can better understand how spatial arrangement of land segments (i.e. spatiotemporal heterogeneity) may initiate a certain advection as well as how, consequentially, it would impact the local surface energy balance (i.e. sensible and latent heat flux).

1.4.4. Limitations

Although the following points are outside of the scope of this paper, they deserve to be noted as they challenge the robustness of the variance Bowen ratio approach:

1) Ideally, this approach should be employed over a broad range of crop surfaces to test how different canopy covers (i.e. canopy height/structure, crop types, and spatial heterogeneity) affect the performance of the variance Bowen ratio approach.

2) In parallel with the previous point, the variance Bowen ratio approach should also be scrutinized for its sensitivity under different atmospheric conditions, including varying atmospheric stabilities.

3) As shown in Section 4.2, the quality of the variance Bowen ratio approach degrades under advective conditions. But this degradation is often reported in eddy covariance measurements as well. Hence, caution needs to be taken under advective conditions, and

the effect of advection on our approach and eddy covariance measurement should be an area to be further researched.

4) Lastly, we compared the results of the variance Bowen ratio approach against eddy covariance measurement, which experienced spectral loss. Although the eddy covariance measurement had similar cospectra of heat flux compared to the Kaimal cospectra (Figure 1. 3 – Top), one should be mindful that the Kansas experiment was conducted over a very flat terrain with a limited amount of sample size, therefore adding more uncertainty for our truth measurement. Clearly, our study site experienced advection even with large fetch, further highlighting the need of revisiting the spectral variance theory.

1.5. Conclusion

In this chapter, we investigated the problem of measuring sensible and latent heat fluxes in-situ. Of particular interest, micrometeorological measurement such as eddy covariance is highly technical and expensive. In this study, we employed the variance-Bowen ratio approach to measure sensible and latent heat fluxes at an alfalfa site to address this problem.

The sensible heat flux from this approach demonstrated strong agreement compared to eddy covariance. We also computed latent heat flux with the modified-Bowen ratio (λE_β), which yielded good results overall. Excluding the net radiometer and ground heat flux measurements, λE_β only relies on an air temperature/relative humidity sensor, highlighting its potential simplicity and affordability. Alternatively, radiation modeling could also be considered to further reduce the cost of the whole system.

Overall, the variance-Bowen ratio approach has potential to be a simple and cost-effective alternative to obtain reliable sensible and latent heat flux. However, this approach still has limitations as mentioned in Section 4.4, and the robustness of this needs to be further investigated. Namely, this approach should be tested over a wide range of crop surfaces under different atmospheric conditions. Additionally, further research should investigate the effect of advection on the variance Bowen ratio approach given that the assumed equal diffusion of heat of water from Bowen ratio breaks under advective conditions.

Chapter 2 - How advection affects the surface energy balance and its closure at an irrigated alfalfa field[2]

Abstract

Orbiting around the non-closure problem in eddy covariance, a new generation of high-resolution thermal imagery has revealed that advection may be more common than previously expected. To investigate this, we conducted an extensive study over an irrigated alfalfa field that experienced both heat and moisture advection. Over the course of five analysis periods (37 days total), multiple tower arrays and profile measurements were deployed to measure the horizontal advection and vertical heat flux divergence. Latent heat flux (λE) measured at the anchor tower showed an enhancement due to both local and non-local processes. Locally, as a result of the upwind λE, advection humidified the atmosphere and increased stomatal opening, enhancing the downwind λE. Simultaneously, with lowered atmospheric demand, λE was suppressed downwind. Our results suggest that stomatal regulation played a dominant role in the enhancement, but not by itself. Spectral analysis revealed that low frequency (i.e., large) eddies contributed high heat and moisture via advection. In combination with thermal remote sensing observations from ECOSTRESS and Landsat 8/9, we found that these large eddies were generated over the upwind surface, and they were independent of the local boundary layer conditions. Consequently, spatiotemporal heterogeneity in land-surface conditions induced large eddies, which further enhanced λE through non-local transport of heat and moisture. Lastly, by conditionally including the advective fluxes, the energy balance closure improved from 89% to 97% ($r^2 = 0.97$, p<0.001) over the five analysis periods. Results from this improved energy balance closure offer additional validation dataset for remote sensing evapotranspiration (ET) models other than forcing closure with Bowen-ratio. Furthermore, our findings provide insights for algorithms aimed at enhancing remote sensing ET products. These algorithms often treat pixels as isolated columns, overlooking the lateral effects of heat and moisture.

---

[2] This chapter is reprinted, with permission, from the submitted article: Wang, T., Alfieri, J., Mallick, K., Arias-Ortiz, A., Anderson, M., Fisher, J., Girotto, M., Szutu, D., Verfaillie, J., Baldocchi, D., 2023a. How advection affects the surface energy balance and its closure at an irrigated alfalfa field.
(In review: Agricultural and Forest Meteorology)

2.1. Introduction
"If you do not have any shadows, you are not in the light" ---- Lady Gaga

The surface energy balance reigns supreme as the queen for meteorology and climate science as it governs the energy and trace gas exchanges between the biosphere and the atmosphere. However, in the land of AmeriFlux and FLUXNET, the energy balance closure problem persists for in-situ observations such as eddy covariance (Wilson et al., 2002; Fisher et al., 2021; Stoy et al., 2013; Leuning et al., 2012). In addition, the knowledge gap on how advection modifies the bio-atmospheric interaction remains. As a commonly overlooked quantity in eddy covariance, advection has cast a long-lasting shadow in the kingdom of surface energy balance ever since the 1960s (Philip, 1959), impeding accurate representations of energy and trace gas fluxes in Earth system. The eddy covariance method provides a direct measurement of the flux density of mass and energy at the measurement height (Baldocchi, 2020). With the constant flux layer theory (Kaimal and Finnigan, 1994), one can assume this flux density represents the underlying ecosystem, but only if there is no storage and no advection. If there is advection, a flux divergence will occur, invalidating the similarity theory. Under this situation, the flux density associated with the biosphere is a function of the integration of the flux density passing through horizontal and vertical directions.
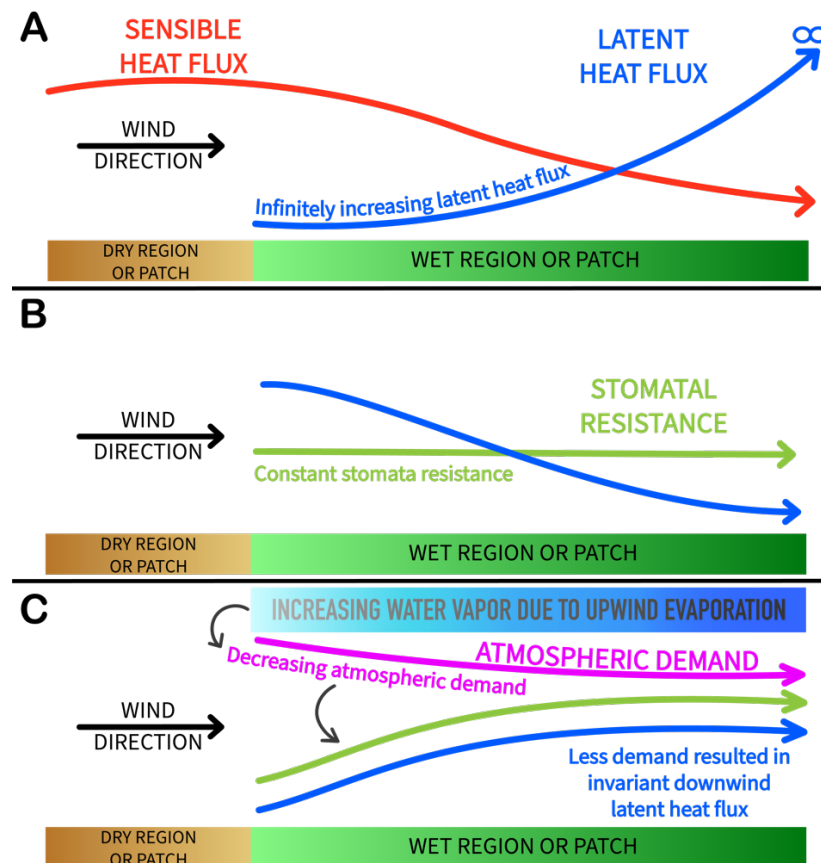
Figure 2. 1. An illustration of how fluxes vary downwind over dry-to-wet transition based on previous literature. Panel A represents Philip (1959); Panel B represents Rao et al. (1974) and Brakke et al. (1978); Panel C represents McAneney et al. (1994), Brunet et al. (1994), Baldocchi and Rao (1995), and Zermeño-Gonzalez and Hipps (1997). Evaporation is referred to as latent heat flux here.

On this quest of the advective enigma, many have laid the foundational work to prove the existence and importance of advection. Early work theorized advection in an analytical fashion, where the spatial heterogeneity can modify mass, energy, and momentum fluxes (Philip, 1959). As a result, the horizontal advection can effectively alter the local rate of evaporation and surface energy balance (Lang, 1973; Lang et al., 1974; Verma et al., 1978; Philip, 1987; Prueger et al., 1996; Baldocchi et al., 2016). By the early theory (Figure 2. 1, Panel A), the hot and dry air advected to an actively transpiring field would induce an "infinitely" increasing evaporation rate across the horizontal plane (Philip, 1959). Clearly, this assumes that the biosphere would unconditionally evaporate, which can only be achieved with a consistently downward sensible heat flux throughout the field. Albeit the incorrect assumption, this emphasized the knowledge gap, which led to the development of studies and analytical models. Unfortunately, the assumption of constant stomatal resistance from these follow-on studies incorrectly predicted that the evaporation would be high at the dry-to-wet transition (Figure 2. 1, Panel B), followed by a smooth decrease as the downwind distance increases (Rao et al., 1974; Brakke et al., 1978). One other limitation of the early generation advection studies is that they relied on K-theory to make measurements, which infer fluxes from the mean quantities of the vertical profiles (Raupach and Thom, 1981; Philip, 1987; McNaughton, 1976a). Specifically, this application is hindered by the assumed equality between the eddy transfer coefficients for sensible heat (K_H) and water (K_W). Under advective conditions, the counter-gradient of the vertical profile would result in a difference in K_H and K_W, hence invalidating the technique (McNaughton, 1976b; Warhaft, 1976). Additionally, non-local large eddies, which are independent of the local conditions, can cause errors in computed K_H and K_W, further biasing the resulting fluxes (Lang et al., 1983).

Nonetheless, it was these early field studies that allowed researchers to challenge the paradigm and consider the system function as an integrated continuum. When linking the biosphere with the atmosphere, a feedback mechanism occurs under advection, where the atmospheric demand (i.e., vapor pressure deficit) diminishes with increasing fetch. Consequently, with the lower atmospheric demand, the evaporation rate is suppressed despite the stomatal opening (Brunet et al., 1994; Itier et al., 1994; McAneney et al., 1994). This also coincides with the field experiment done by (Baldocchi and Rao, 1995), and their eddy covariance measurement showed that heat advection did not increase the evaporation rate substantially at the field edge as a negative feedback was linked to heat advection. Specifically, with heat advection, plants upwind started to conserve water with higher stomatal closure, hence, reducing the evaporation rate. Further downwind where the fetch-to-height ratio exceeded 75, evaporation rate did not increase due to the lower atmospheric demand. This was because as the downwind distance increased, the water vapor in the air also increased horizontally due to upwind evaporation. With a higher amount of water vapor, the atmosphere was more humidified (i.e., less atmospheric demand), hence resulting in an invariant evaporation rate further downwind (Figure 2. 1, Panel C). Zermeño-Gonzalez and Hipps (1997) also found similar results where spectral analysis showed that the spatial variation of scalars with downwind distance is governed not only by the local boundary layer conditions, but also by the upwind conditions. The large contribution of fluxes in the low frequency range showed that these upwind conditions produced larger eddies, effectively modifying the local surface energy balance.

In the early 2000s, eddy covariance started to become the gold standard for quantifying energy and trace gas fluxes (Baldocchi et al., 2001). The establishment of flux networks, such as FLUXNET and AmeriFlux have provided valuable datasets for validating remote sensing models (Volk et al., 2023). However, the chaotic nature of the atmospheric flow sourced from surface heterogeneity makes the underlying assumption of eddy covariance less appropriate for certain landscapes (Foken and Wichura, 1996). Despite the early momentum, research on advection and its effect on evaporation received less attention than anticipated. Instead, campaigns were initiated with an exclusive focus on carbon advection in forests and undulating or mountainous terrains (Aubinet et al., 2010; Feigenwinter et al., 2008). Of particular relevance, Moderow et al. (2021) found that horizontal advective fluxes of heat and water were present even under well-mixed conditions. In their study, advective fluxes were governed by the complex terrain (i.e., local slope) while the inclusion of these neglected fluxes only improved the energy balance closure at one of the three tower sites by 7%, which underlined that advection can be highly site specific. Oncley et al. (2007) initiated Energy Balance Experiment (EBEX-2000) with the goal to close the surface energy balance in a flood irrigated cotton field. However, their findings showed an imbalance that remained unsolved even by considering advective fluxes as these were too small to close the energy budget. Yet, it is important to note that the large-scale synoptic flow from the nearby foothills near their site may have induced non-local effects that contributed to the energy imbalance. Indeed, wavelet analysis from Gao et al. (2016) revealed that large eddies altered the turbulence structure and affected the scalar distribution. It is also worth noting that their cotton site was patch irrigated from north to south, hence introducing intra-field variability in soil moisture and temperature. This could also lead to the flux footprints seeing mixed dry and wet conditions, further affecting the surface energy balance.

Orbiting around the non-closure problem, these previous studies investigated whether advection could improve the energy balance closure. In reality, advection is highly site specific as are other variables that could result in an energy imbalance (Novick et al., 2014), and there is no definitive answer to the energy balance closure problem. Kochendorfer and Paw U (2011) carried out expansive eddy covariance measurements to investigate the effects of the advection on surface energy balance. They showed that horizontal advection can be ignored for a moderate distance downwind of transitions, while the vertical advection term close to the field edge was non-negligible. Close to the field edge, the inclusion of advective terms greatly improved the closure. However, further downwind, the inclusion of advective terms only had small effects on the closure. From a lake-to-land transition, Higgins et al. (2013) used Raman Lidar and showed that the horizontal moisture advection was too small to explain the lack of closure. However, they used an analytic approach and proposed a solution to identify the location where advection would be prevalent. With these short-term studies, an additional question arises as to whether advection happens continuously. From a sea-to-land transition, Rey-Sánchez et al. (2017) found a much larger magnitude of moisture advection. In addition to the apparently strong sea-land moisture gradient, advection was also related to seasonality, in which June-August was higher than April-May due to differences in meteorological conditions at their study site. Harder et al. (2017) examined the role of heat and moisture advection on snowmelt, and they found that both of the advective fluxes contributed to the net available energy, acting as an additional source for snowmelt. This highlights that for certain sites, advective fluxes should indeed be considered in field measurements and modeling, as they are essential for better representing fluxes in spatiotemporally dynamic surfaces.

Leveraging large eddy simulation with eddy covariance measurements, studies have shown that land surface heterogeneity can lead to secondary circulation (i.e., low-frequency large eddies), where large and persistent horizontal and vertical advection can bias eddy covariance measurements and result in a non-closure (Eder et al., 2015; Kenny et al., 2017). Morrison et al. (2021) investigated the heat transport in a dry-lake-bed desert site with surface temperature heterogeneity using experimental data from an array of flux towers within a 400 m by 400 m grid. They found that the magnitudes of horizontal heat advection and vertical heat flux divergence were large during the convective afternoon periods. By using a conceptual model, their results showed that over 80% of the horizontal advection was due to the intra-field variability in temperature. Combined with temperature variation and wind speed, advection provided an additional source of heat transport, which essentially biases the accuracy of the simplified surface energy balance equation we commonly use to assess closure (Morrison et al., 2021). Zhou et al. (2023) investigated the contribution of horizontal and vertical advective fluxes on energy imbalance by using a large eddy simulation over an idealized surface with alternating dry and wet heterogeneity. In their study, horizontal advection was large under heterogeneous transition (e.g. dry to wet to dry), and it was a key contributor to the lack of energy balance closure. Evidently, understanding the mechanism and occurrence behind advection remains challenging, but this knowledge gap could help us better understand bio-atmospheric interactions. Previous studies have largely focused on understanding advection with a sharp transition, commonly from a hot/dry to a cool/wet surface. However, agricultural lands, especially in the semi-arid California, embody different on-farm practices, creating a unique spatiotemporal mosaic of vegetated and bare surfaces (as shown in Figure 2. 2 for our study site). This makes us wonder: should the heat and moisture advection be considered as a co-located process that happens simultaneously?

In this study, we deployed experiments and collected advection data in an alfalfa field in 2021 (heat advection) and 2022 (heat and moisture advection). The alfalfa went through periodic cuttings, and the upwind fields were covered with seasonal crops (mainly corn) that underwent different on-farm regimes ranging from planting/harvest dates, irrigation to growing cycle. This unique spatiotemporal heterogeneity initiated by different on-farm practices allowed our field site to interact with various upwind conditions. By leveraging high-resolution multispectral and thermal satellite imagery, we detected different cases of advection aside from the classic dry-to-wet transition. With an array of meteorological and eddy covariance flux measurements, both horizontal and vertical components were used to measure the horizontal advection of heat and water as well as the vertical heat flux divergence. Through this deployment, we collected data over five study periods and captured diverse energy fluxes under unique sets of advective cases. The overarching goal of the study is to quantify the magnitude of horizontal advective fluxes to better understand the exchanges of water and heat fluxes in the bio-atmospheric continuum. By improving the understanding of how advection affects the surface energy balance (i.e., water and heat budgets), this study provides insights for upscaling algorithms that can improve remote sensing products, which tend to use siloed pixel to compute energy and scalar exchanges in a column, rather than considering the important role of lateral fluxes of heat and water.

2.2. Methods

2.2.1. Site description

The site (Lat: 38.0992, Lon: -121.4993) sits in the Sacramento-San Joaquin Delta of California with an operational AmeriFlux tower since 2016 (US-Bi1, Rey-Sanchez et al., 2022). A perennial alfalfa crop is grown at this site, and the crop is sub-surface irrigated by a nearby ditch. The soil type is a Ryde-Peltier complex with 50% Ryde, 35% Peltier, 5% Rindge, 4% Valdez, 3% Scribner, and 3% Venice (https://casoilresource.lawr.ucdavis.edu/gmap/). The topography is flat with the main tower (US-Bi1) measuring fluxes with a fetch-to-height ratio of ~115, making it ideal for eddy covariance measurements. Advection data were collected from Aug 5th to Nov 4th, 2021, and Apr 25th to Oct 31st, 2022. To clarify, we only collected heat advection data in 2021, while both heat and moisture advection data were collected in 2022. Throughout the data collection periods in both years, our site experienced periodic cutting, while the upwind fields also went through different on-farm management. Most upwind sites (left side of cyan line in Figure 2. 2) were fallow in the spring and planted with corn during the summer growing season. Together, the spatiotemporally heterogeneous upwind fields provided opportunity to inspect horizontal and vertical flux exchanges.

Using Sentinel-2, we visualized different conditions of our field site and nearby sites in 2022 via the Normalized Difference Vegetation Index (NDVI) as shown in Figure 2. 2. The red box in Figure 2. 2 indicates our field site while the cyan line separates the upwind regions. We refer to the right side of this cyan line as the direct upwind region and the left side as the further upwind region. In 2022, from the start of data collection to June 3rd, only direct upwind fields were cultivated, and the further upwind fields remained to be bare (Figure 2. 2c). After around June 8th, further upwind fields were planted and remained growing until September (Figure 2. 2d & e). In this study, we also included data from 2021, a visualization of the field condition in this year is in Figure 2. 2a and b, and more details can be found in Wang et al. (2023). Given the various site characteristics over the entire study interval, we have identified 5 specific growing periods investigated in this study in Table 2. 1. below. The classification of the site characteristics in Table 2. 1. was determined from optical (Sentinel-2) and thermal infrared observations (Landsat 8/9).
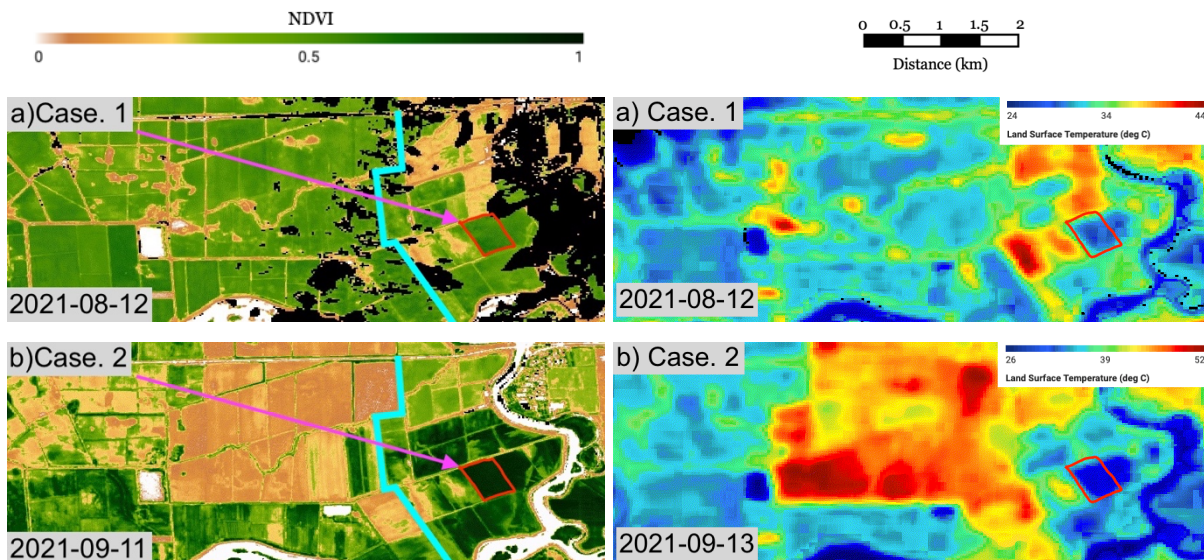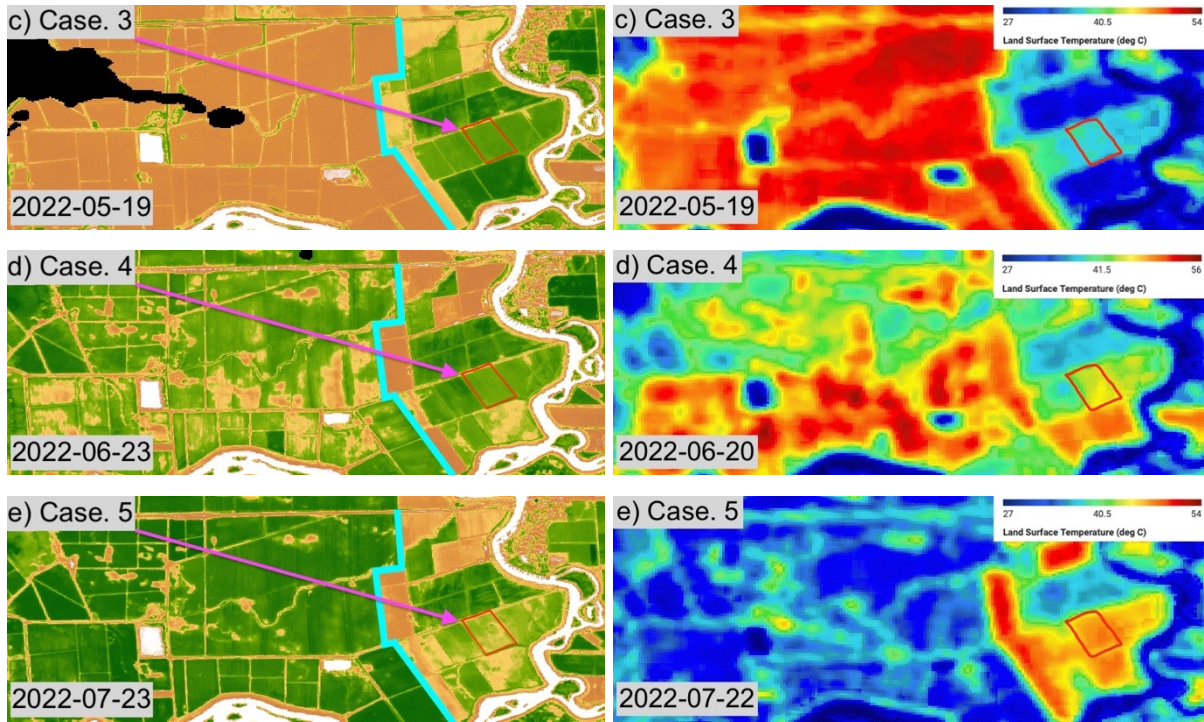
Figure 2. 2. Sentinel-2 NDVI (left) and Landsat 8/9 land surface temperature (right) showing the site characteristics of the alfalfa site (red box) and its upwind fields. Upwind regions are further divided by the cyan line. Right side of this line is the direct upwind fields and left side of this line is the further upwind (corn) fields. The pink arrow indicates the predominant wind direction.

Table 2. 1. Five different cases examined in this study with NDVI conditions for the study site, direct upwind, and further upwind.

Case	Site characteristics	Analysis period	NDVI		
			Alfalfa site	Direct upwind	Further upwind
1	Semi-homogeneous	2021-08-11 to 2021-08-16	0.66	0.59	0.62
2	Hot/dry to very cool/wet	2021-09-07 to 2021-09-13	0.90	0.73	0.20
3	Hot/dry to cool/wet	2022-05-18 to 2022-05-25	0.56	0.59	0.11
4	Mixed heterogeneity	2022-06-20 to 2022-06-28	0.40	0.34	0.37
5	Cool/wet to hot/dry	2022-07-16 to 2022-07-23	0.29	0.34	0.59

In the selected periods (Table 2. 1.), most of the wind came from within W to WNW region (Figure 2. 3). This is preferrable along with our experiment setup (Sect. 2.2), and we further filtered the wind direction to align with our advection measurements (Sect. 2.4).
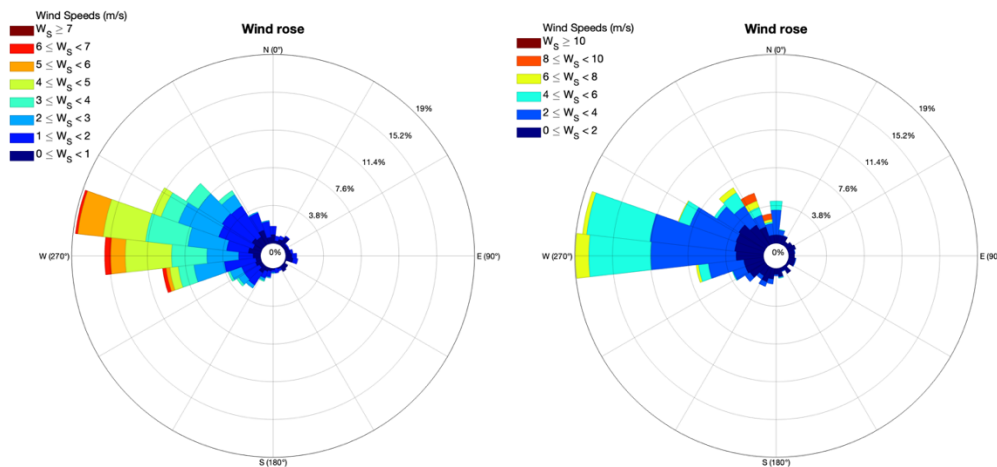
Figure 2. 3. Windroses showing the distributions of wind speed and direction during the analysis period for case 1 and 2 in 2021 (left) and case 3, 4, and 5 in 2022 (right).

2.2.2. Experiment setup
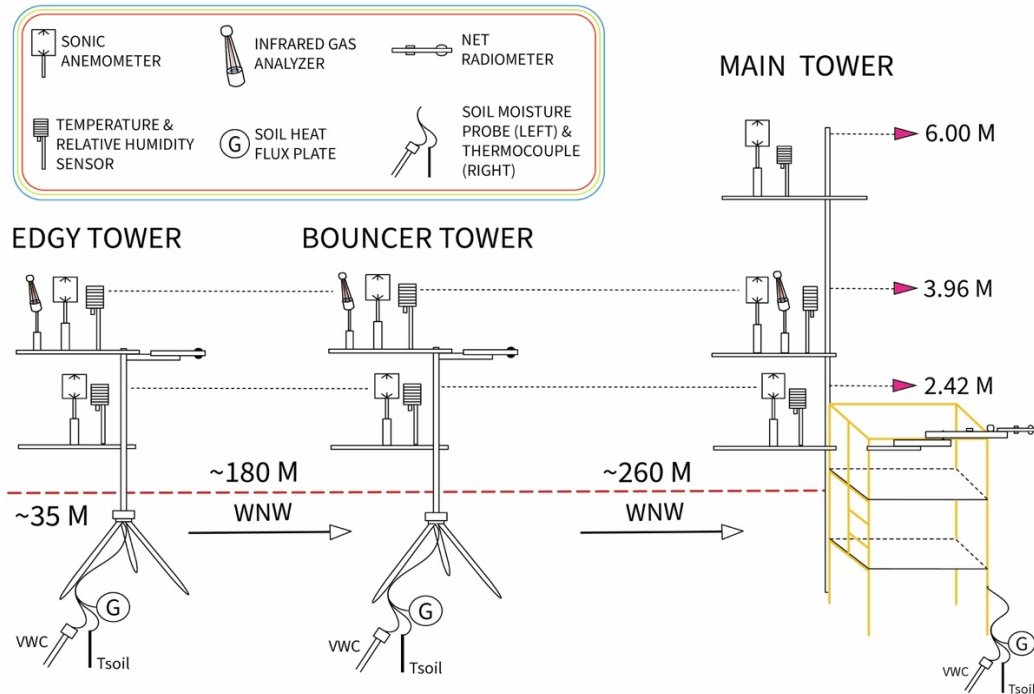
Figure 2. 4. An illustration of the sensor diagram for 2022 study. A detailed description is provided in Sect. 2.2.

For the study period in 2022, two additional towers were deployed upwind of the main tower to measure heat and moisture advection as well as vertical heat flux divergence (Figure 2. 4). The first tower was deployed ~35 m away from the field edge to measure the fluxes by the edge of the field, hereafter denoted as the edgy tower. The second tower was deployed ~180 m away from the edgy tower (or 215 m from the field edge), measuring the fluxes near the middle of the field. This second tower is denoted as the bouncer tower. The third tower was the anchor tower, measuring the fluxes across the field given its large fetch. The anchor tower, hereafter denoted as the main tower (US-Bi1, Rey-Sanchez et al., 2022), was ~260 m downwind of the bouncer tower (or 475 m from the field edge). Together, the triple tower transect was established along the mean wind direction at ~292 deg. This setup allowed us to collect not only the horizontal advective fluxes, but also the vertical heat flux divergence. In this setup, we directly measured sensible and latent heat fluxes at 3.96 m. To estimate the sensible heat flux (H) at other heights, we used the variance-Bowen ratio approach following Wang et al. (2023). A detailed description of the sensor arrays used in this study can be found in Table 2. 2.

Compared to the experiment in 2022, only one additional tower, the bouncer tower, was deployed in the upwind in 2021 to measure fluxes near the middle of the field. This tower was in the same location as the bouncer tower in 2022. In contrast to the 2022 study, there were several differences in the 2021 deployment:
1. At both levels of the bouncer tower (2.42 m and 3.96 m) and the lower level of the main tower (2.42 m) in 2021, we used the variance-Bowen ratio approach to solve for H.
2. There was no water flux measurement made at the bouncer tower in 2021. The latent heat flux was indirectly resolved through the energy balance residual as needed.

3. No measurements were made at 6 m height at the main tower in 2021.
4. The bouncer tower had no net radiometer and soil sensors in 2021.

The sensors used in the 2021 experiment have been marked with (†) in Table 2. 2.

Table 2. 2. Sensors used in the 2022 data collection as well as their location and corresponding data. The symbol (†) indicates sensors used in both 2021 and 2022.

Measurement	Instrument	Sampling regime, height (+), or depth (-)		
		Main tower	**Bouncer tower**	**Edgy tower**
Turbulence	WindMaster 1590	20Hz, +3.96 m †	20Hz, +3.96 m †	20Hz, +3.96 m
		20Hz, +2.42 m †	20Hz, +2.42 m †	20Hz, +2.42 m
		20Hz, +6.00 m		
H_2O/CO_2	LI-7500	20Hz, +3.96 m †	20Hz, +3.96 m	20Hz, +3.96 m
Temperature and humidity	HMP155A or HygroVue	20Hz, +3.96 m †	20Hz, +3.96 m †	20Hz, +3.96 m
		20Hz, +2.42 m †	20Hz, +2.42 m †	20Hz, +2.42 m
		20Hz, +6.00 m		
Net radiation	NR01 or NR-LITE	0.1Hz, +2.70 m	0.1Hz, +3.34 m	0.1Hz, +3.34 m
Soil heat flux	HFP01 or Peltiers	0.1Hz, -0.02 m	0.1Hz, -0.10 m	0.1Hz, -0.10 m
Soil moisture	CS 655 or ML3	0.1Hz, -0.02 m	0.1Hz, -0.10 m	0.1Hz, -0.10 m
Soil temperature	Type T Thermocouple	0.1Hz, -0.02 m	0.1Hz, -0.10 m	0.1Hz, -0.10 m

2.2.3. Data processing

Measuring advection presents theoretical difficulties as well as technical challenges. Additionally, measuring and sensing small differences vertically and horizontally across a distance can be challenging. As a result, we conducted a sensor intercomparison before or after each field campaign to inspect and minimize the potential errors that could occur during the data collection period (Appendix H). For both years, a linear regression model was used to assess the performance of sonic anemometers and temperature/relative humidity sensors compared to a reference sensor. For 2021, the mean statistics were computed for mean horizontal wind (slope=0.99; $r^2>0.99$), air temperature (slope=0.99; $r^2>0.99$), and relative humidity (slope=1.00; $r^2>0.99$). For 2022, mean horizontal wind (slope=0.99; $r^2\geq0.99$), air temperature (slope=0.99; $r^2\geq0.99$), and relative humidity (slope=1.00; $r^2>0.99$). Additional assessment on sonic kinematic heat flux and standard deviation of vertical wind speed was also conducted and more detail can

be found in Appendix H. Prior to calculating the vertical heat flux divergence and based on the intercomparison results, we used the sonic anemometer at the 3.96 m height as the reference sensor and assessed sonic kinematic heat flux measured at 2.42 m and/or 6.00 m. Since vertical heat flux divergence was used to assess the advective balance shown in Eq. 3a, we calibrated these kinematic heat fluxes accordingly to account for the deviations (Appendix H).

Routine data QA/QC was conducted on eddy covariance measurements used in this study, including: 1) despiking algorithm to filter spikes in sonic anemometer data; 2) 2D coordinate rotation to minimize tilt error and force mean vertical velocity to zero (Kaimal and Finnigan, 1994); 3) forced time-lag to account for physical separation between the sonic anemometer and gas analyzer; and 4) spectral analysis and correction to account for high-frequency loss. Additionally, storage-corrected soil heat flux and photosynthetic energy storage were computed (Meyers and Hollinger, 2004; Wang et al., 2023). For profile points below and above the main measurement height (3.96 m), we used the variance-Bowen ratio technique, which samples the Bowen ratio with the standard deviation of air temperature and specific humidity, to compute sensible heat fluxes at those levels (Suppl. 2). For detailed description of data processing, soil heat storage correction, and the application of the variance-Bowen ratio technique, please see Sect. 2 in Wang et al. (2023). Lastly, we followed Pennypacker and Baldocchi (2016) to compute the aerodynamic canopy height. Canopy heights used in this study can be found in Figure B1.

2.2.4. Horizontal advection terms

The two-dimensional conservation budget, with Reynolds decomposition and averaging, can be expressed with local storage (term I), horizontal scalar advection (term II), vertical scalar advection (term III), horizontal flux divergence (term IV), and vertical flux divergence (term V):

$$\bar{S}(x, y, z, t) = \frac{\partial \bar{c}}{\partial t} + \bar{u} \frac{\partial \bar{c}}{\partial x} + \bar{w} \frac{\partial \bar{c}}{\partial z} + \frac{\partial \overline{u'c'}}{\partial x} + \frac{\partial \overline{w'c'}}{\partial z} \qquad \text{Eq. 1}$$

$$\text{I} \qquad \text{II} \qquad \text{III} \qquad \text{IV} \qquad \text{V}$$

where $\bar{S}$ is the source/sink rate, $\bar{c}$ is the mean scalar concentration, $\bar{u}$ and $\bar{w}$ is the horizontal, vertical wind speed, respectively. Overbars denote the half-hourly averaging, and primes denote fluctuations from the average. Assuming the storage (term I), vertical advection (term III), as well as the horizontal flux divergence (term IV) to be negligible, the turbulence budgets for sensible heat flux (H) and latent heat flux (λE) can be expressed with term II and V:

$$H = \int_0^{Zm} \rho \cdot C_p \cdot \bar{u} \cdot \frac{\partial \bar{T}}{\partial x} \, dz + \int_0^{Zm} \rho \cdot C_p \cdot \frac{\partial \overline{w'T'}}{\partial z} \, dz \qquad \text{Eq. 2a}$$

$$\lambda E = \int_0^{Zm} \rho \cdot \lambda \cdot \bar{u} \cdot \frac{\partial \bar{q}}{\partial x} \, dz + \int_0^{Zm} \rho \cdot \lambda \cdot \frac{\partial \overline{w'q'}}{\partial z} \, dz \qquad \text{Eq. 2b}$$

where ρ (kg m^{-3}) is the density of air, Cp (J kg^{-1} K^{-1}) is the specific heat capacity of air, λ (J kg^{-1}) is the latent heat of vaporization, T is the air temperature (K), and q is the specific humidity (kg kg^{-1}). To represent the profile depth, a logarithmic wind profile was used for integration. Specifically, we determined the zero-plane displacement height (0.67 x canopy height) and roughness length (0.15 x canopy height) using the aerodynamic canopy height (Stull, 1988; Arya,

2001; Pennypacker and Baldocchi, 2016). To calculate the horizontal scalar gradient (i.e., in T and q), we followed the approach in Kochendorfer and Paw U (2011) and fitted half-hourly measurements on a pre-defined curve with all the towers. One distinction is that we used the same power function ($y=ax^b+c$) in their study for q gradient, however, for T gradient, the curve fitted better over a 2nd degree polynomial function ($y=ax^2+bx+c$). Nevertheless, these functions were then evaluated with the distance downwind from the field edge (e.g. 475 m for the main tower) to obtain $\partial \overline{T} / \partial x$ and $\partial \overline{q} / \partial x$. Lastly, data were excluded when the wind directions came from more than 20° (+/- 10°) of the predominant wind direction of 292°.

Under the same assumption for Eq. 1, if the horizontal and turbulent flows are steady (i.e. constant source/sink), Eq. 2a and 2b can be rearranged so that the advective flux of heat and moisture is balanced by the turbulent flux divergence as shown in Eq. 3a and 3b (Finnigan, 1999; Baldocchi et al., 2000):

$$\overline{u} \frac{\partial \overline{T}}{\partial x} = -\frac{\partial \overline{w'T'}}{\partial z} \qquad \text{Eq. 3a}$$

$$\overline{u} \frac{\partial \overline{q}}{\partial x} = -\frac{\partial \overline{w'q'}}{\partial z} \qquad \text{Eq. 3b}$$

This balance allows one to estimate the horizontal advection using vertical flux divergence, and we assessed this advective balance for heat flux. To obtain the vertical heat flux divergence from measurement height to the canopy, we first used the existing measurements at 2.42m to derive H using the variance-Bowen ratio technique. Then, we linearly extrapolate the H to the aerodynamic canopy height (Z_{veg}). Note that for this derivation, we calibrated the kinematic heat flux at 2.42m to the one at 3.96m based on the intercomparison (Appendix H). With the linear assumption of the flux divergence, similar to Higgins et al. (2013), we used Eq. 3a and estimated the total heat advection with vertical heat flux divergence in Eq. 4:

$$\Sigma \text{heat advection} \approx -\int_{Z_{veg}}^{Z_m} \rho \cdot C_p \cdot \frac{\partial \overline{w'T'}}{\partial z} \, dz \approx -\rho \cdot C_p \cdot (\overline{w'T'}|_{Z_m} - \overline{w'T'}|_{Z_{veg}}) \qquad \text{Eq. 4}$$

2.3. Results and discussion

2.3.1. Spectral analysis

At our site, the surface characteristics changed throughout the study period due to different on-farm practices (Figure 2. 2). The dynamic nature of vegetation height (Figure B1) and varying, local and non-local, field conditions (Figure 2. 2 and Table 2. 1.) necessitate an inspection of covariances of heat and moisture fluxes. Specifically, the measured variances or covariances is the integral of power spectral density or co-spectral density, respectively. By using Fourier transform, the power- and co-spectral densities can be decomposed and described as a function of the contributing frequencies. This entails that the flux contribution of the measured fluxes can be inspected with its corresponding eddy sizes. As a result, we computed the mean spectral and co-spectral densities via spectral analysis and assessed the measured energy fluxes (Wolf and Laca, 2007). In Figure 2. 5, we normalized the cospectra of scalars by their total covariance (i.e., nSwT(f)/w'T' and nSwQ(f)/w'q'). This is plotted against a dimensionless frequency (f), where

natural frequency (n) is multiplied by the height above the zero-displacement height (z-d) and normalized by the horizontal wind speed as, f=n(z-d)/u.
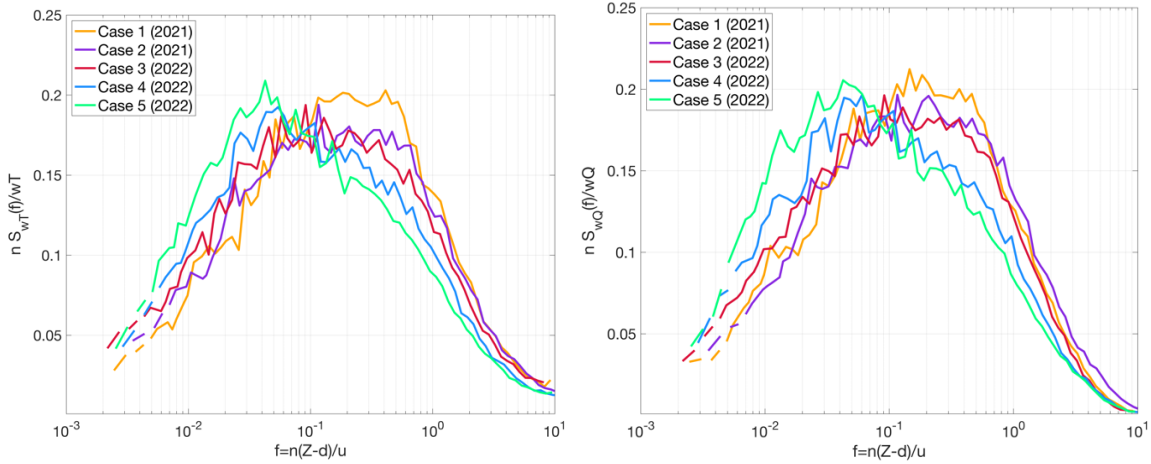
Figure 2. 5. Normalized co-spectra of vertical velocity with temperature, T (left) and moisture, Q (right) at the main tower for Case 1 (orange), Case 2 (purple), Case 3 (red), Case 4 (blue) and Case 5 (green) in semi-log scale prior to spectral correction. For each case, the half-hourly data are averaged over the case duration between 1000 to 1800 hours.

The cospectra of vertical velocity with temperature (Figure 2. 5 left) and with moisture (Figure 2. 5 right) exhibited different behaviors over the five cases. A summary of the spectral peak and the associated eddy size for each case can be found in Table 2. 3. For both cospectra, mid-sized eddies dominated the contributions of heat and water fluxes for Case 1 and 2, while large-sized eddies were responsible of the higher contributions of heat and water fluxes for Case 4 and 5. For Case 3, a mix of large to mid-sized eddies resulted in a higher contribution of heat and water fluxes at low to mid frequencies. A detailed discussion linking the cospectral behavior and energy fluxes for each case is provided in Sect. 3.2.

Both cospectra of heat and water fluxes were also assessed against the idealized Kaimal cospectra of heat (Figure C1). Compared to the cospectra of heat flux, there was large spectral loss for the spectra of water flux, especially in the inertial subrange. This high frequency attenuation was corrected by using a transfer function, and it was applied to both heat and water fluxes (Alfieri et al., 2012; Baldocchi et al., 2016, 1981; Prueger et al., 1996; Rao et al., 1974; Rosenberg, 1969; Rosenberg and Verma, 1978; Wang et al., 2021). To clarify, since the ideal spectra for water flux is not well established, we used the ideal cospectra of heat flux to apply the spectral correction.

Table 2. 3. Non-dimensional frequency of spectral peak and the associated eddy size for cospectra of heat and water fluxes shown in Figure 2. 5.

Case	Cospectra of heat flux		Cospectra of water flux	
	Peak frequency	Eddy size	Peak frequency	Eddy size
1	0.11 to 0.4	Mid	0.11 to 0.4	Mid
2	0.11 to 0.4	Mid	0.11 to 0.4	Mid
3	0.045 to 0.2	Large to mid	0.09 to 0.4	Large to mid

| 4 | 0.05 | Large | 0.06 | Large |
| 5 | 0.04 | Large | 0.04 | Large |

2.3.2. Energy and advective fluxes

2.3.2.1. Heat extraction from the atmosphere and enhanced λE

In Case 1 (semi-homogeneous condition, Table 2. 1.), there was a distinct transition from upwind corn fields (cool) to direct upwind fields (warm) to the alfalfa site (cool). Although the NDVI of 0.59 for the direct upwind fields was not too low, Landsat 8 land surface temperature (LST) showed that these fields were ~5-10 °C warmer, indicating the drier and warmer upwind conditions (Figure 2. 2a). Interestingly, these small dry/warm upwind patches still resulted in enhancement in latent heat flux (λE), which exceeded the net available energy after 13:00. This enhancement likely took place when the sensible heat flux (H) started to direct progressively downward (i.e., towards negative) at 11:00. Throughout the diel cycle, the heat advection ($U \cdot \nabla_T$) increased gradually, and it reached the maximum of ~60 W m^{-2} at 14:30 (Figure 2. 6A). But what caused the large enhancement in λE under this semi-homogeneous condition? The small dry/warm upwind patches may have produced larger convective eddies to be advected downwind to our field, where relatively large eddies in the mid-frequency resulted in high contribution of heat and water fluxes at this location (Figure 2. 5 orange line & Table 2. 3.). In addition, temperature profile (Figure D1) showed the presence of an internal boundary layer where air temperature was higher due to heat advection while the aerodynamic temperature was lower due to evaporative cooling, further explaining the persistently negative H and enhanced λE (Figure 2. 6A).

In Case 2 (hot/dry to very cool/wet transition, Table 2. 1.), we examined the classic oasis-like system. With a large patch of hot and dry fields in the further upwind region (Figure 2. 2b), H was consistently small and directed downward (i.e., negative) after 11:30 due to the development of the internal boundary layer (Figure D1) from $U \cdot \nabla_T$. Subsequently, λE was enhanced and exceeded the net available energy after 13:30 (Figure 2. 6B). By combining remote sensing observations (Figure 2. 2b) with spectral analysis (Table 2. 3.), the further upwind bare fields likely produced relatively larger eddies via convection, and these eddies were then advected downwind and warmed the downwind atmosphere. As a result, the evaporating surface extracted H from the warmer and drier atmosphere above, resulting in an enhanced λE.
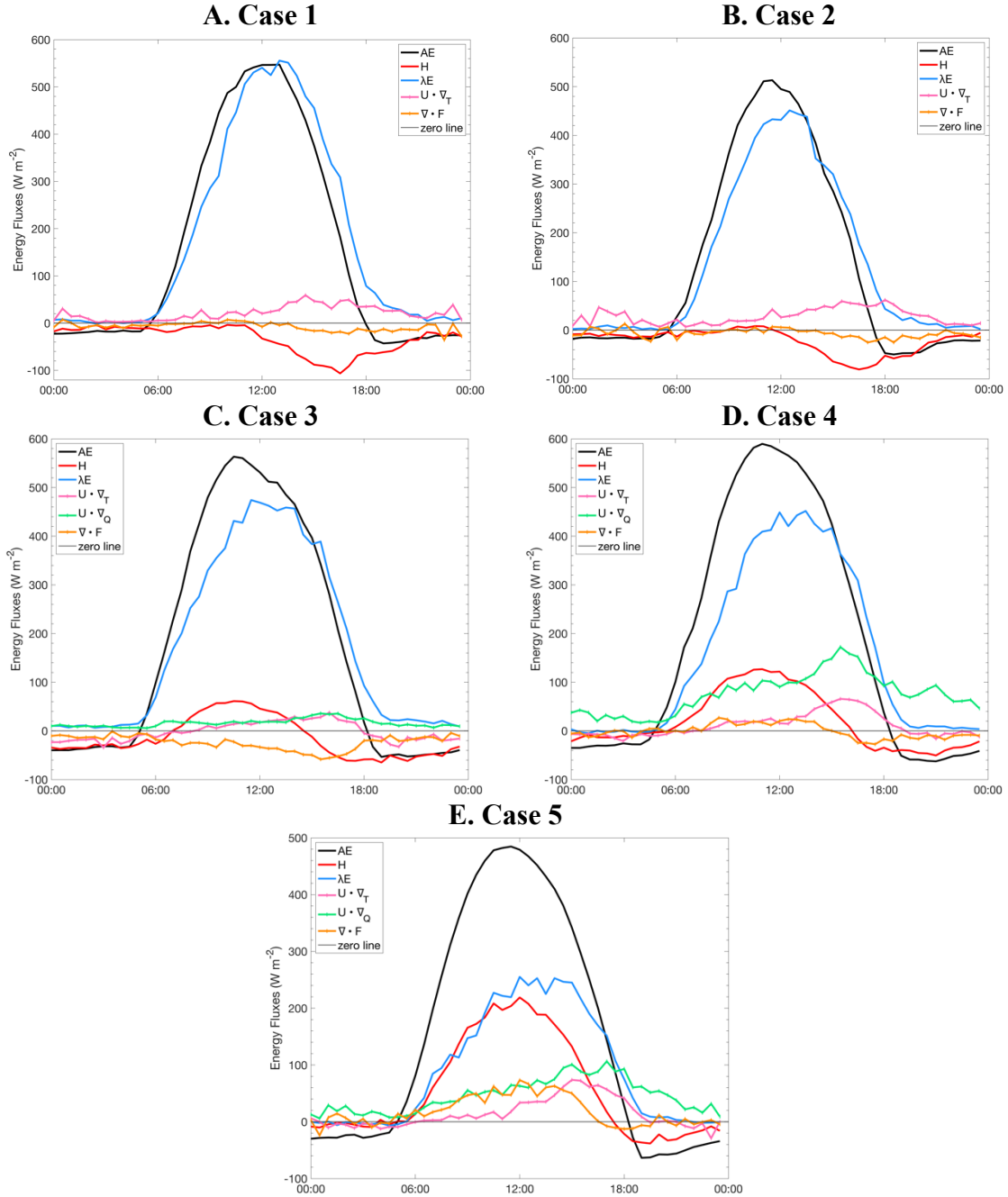
Figure 2. 6. Diel mean of the net available energy, AE (black); sensible heat flux, H (red); latent heat flux, λE (blue); horizontal heat advection, U·∇$_T$, (pink); horizontal moisture advection, U·∇$_Q$ (green); and vertical heat flux divergence ∇·F. (orange).

Compared to Case 2 in 2021, Case 3 (hot/dry to cool/wet transition, Table 2. 1.) had a similar condition, where the site NDVI in this case (0.56) was lower than the one in Case 2 (0.90). The magnitude of H was small (max ~60 W m^{-2} at 11:00), and it declined and became negative (i.e., downward) starting from 14:30. λE was already enhanced as H started to decline after 11:00, and the enhancement exceeded the net available energy when H became negative at 15:00 (Figure 2. 6C). As shown with the thermal remote sensing image (Figure 2. 2c) and spectral analysis (Table

2. 3.), processes from larger eddy structures were present, and we examined the effect of these large eddies in the following section (Sect. 3.2.2). Cases 4 and 5 are also discussed in Sec 3.2.2 below.

From semi-homogeneous to classic oasis (Case 1-3), our results are consistent with previous studies that horizontal heat advection can enhance λE via the heat extraction from the atmosphere above (Rosenberg, 1969; Rao et al., 1974; Rosenberg and Verma, 1978; Baldocchi et al., 1981; Prueger et al., 1996; Alfieri et al., 2012; Baldocchi et al., 2016; Wang et al., 2021). We found that large to mid-sized eddies, advected from the upwind region, allowed the heat extraction by creating the warmer atmosphere aloft the cool surface. In particular, there was a positive feedback at play. As the day progressed, λE became progressively higher (i.e., surface became progressively cooler). Eventually, the surface was cooler while the atmosphere was warmer due to the heat advection from the larger eddies (Table 2. 3. and Figure D1). At this point, the surface extracted H from the atmosphere above, providing additional energy to enhance λE in addition to the net radiation. This process did not stop until sunset, when the net available energy became null (Figure 2. 6A, B, & C).

2.3.2.2. Spatial heterogeneity and large eddies

In the Theory of Forms, Plato spoke of the world in physical and non-physical forms, but words of philosophy are difficult to grasp. Lady Gaga always encourages one to feel the depth of life, be proud, and shine in their own way. Similarly, surface energy balance is a complex system that suffers from the constraints of binary opposition should we consider a process to be one or the other. Compared to Cases 1 and 2 in 2021, Cases 3-5 in 2022 had more erratic see-saw pattern in λE despite the overall smooth net radiation (Figure 2. 6). Given the complexity of our site, we have to consider other processes that operate at a greater spatial scale. Following Li and Bou-Zeid (2011) and (Zermeño-Gonzalez and Hipps, 1997), the correlation coefficient of the momentum flux (R_{uw}) was computed across the three measured heights at the main tower. These R_{uw} at different levels suggested the presence of the large eddies, which correspond to the erratic pattern seen in λE (Figure E1).

As discussed in the previous section, in Case 3 the alfalfa field extracted H from the warmer atmosphere above and enhanced λE (Figure 2. 6C). The temperature profile (Figure D1) showed that the surface was cooler than the atmosphere, especially from 1430 to 1900 hours, allowing heat extraction due to the growing internal boundary layer. At the same time, larger eddies likely exacerbated the heat extraction by bringing more warm air downward. The higher contributions of heat and water fluxes at the low frequencies (Figure 2. 5 red line & Table 2. 3.) suggested the effect of these large eddies. Power spectra of temperature and specific humidity also peaked at low frequency, further supporting the non-local effect of remote sources from the upwind regions (Figure 2. 7). Specifically, the hot and dry fields in the further upwind (Figure 2. 2c) produced large convective eddies that were advected downwind to our alfalfa field. These eddies might have also carried some moisture from both direct upwind fields and within the alfalfa field, yielding the higher moisture contribution at the low frequency range (Figure 2. 7). The presence of the non-local large convective eddies was also supported by the higher R_{uw} (i.e., $R_{uw} < -0.25$), especially at the higher measurement height of 6.00 m (Figure E1). Subsequently, the transport of these convective eddies created the temperature inversion from 1430 to 1900 hours (Figure D1). As a result, the downdraft of these large warm eddies likely penetrated the IBL, allowing more heat to be extracted and to reach the surface. Together, the temperature inversion, created

by the ongoing evaporative cooling and the large eddies, further explained the downward H and enhanced λE.
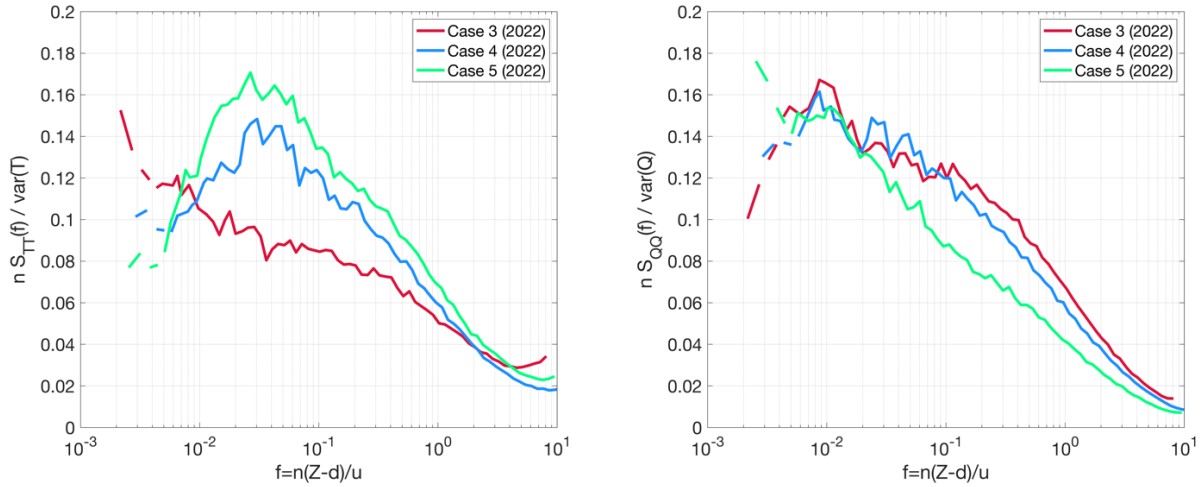
Figure 2. 7. Power spectra of air temperature, T, (left) and specific humidity, Q, (right) normalized by the variance of air temperature and specific humidity, respectively. For each case, the half-hourly data are averaged over the case duration between 1000 to 1800 hours. In power spectra of T, low frequency spectral peaks are at ~0.002 (case 3) and ~0.03 (case 4 & 5). In power spectra of Q, low frequency spectral peaks are at ~0.008 (case 3 & 4) and ~0.003 (case 5).

In a mixed heterogeneity (Table 2. 1., Case 4), despite the lower NDVI in this period, H still became negative after 16:00 (Figure 2. 6D). While the temperature profile only explained the negative H after 17:00, it is noticeable that the profile had already started shifting from 1500 to 1630 hours (Figure D1). This might be due to the ongoing surface cooling from advection as λE had already exceeded the net available energy ~15:00, which explained the delay of sign changing for H. The cospectra of heat and water fluxes (Figure 2. 5 blue line) showed higher contributions at the low frequencies, indicating that larger eddies were responsible for the scalar transport as a result of the alternating patches of the hot/dry and cool/wet upwind fields. This large-scale process is further supported by low frequency contributions in the power spectra of air temperature and specific humidity (Figure 2. 7). As a result, these larger eddies may have resulted in the modification in the surface energy balance (Figure 2. 6D).

For a cool/wet to hot/dry transition (Table 2. 1., Case 5), the further upwind corn fields have reached peak growing season, providing additional moisture to be advected to the dry alfalfa site with low canopy density (NDVI=0.29). During the day, the warmer surface from 0900 to 1630 hours explained the positive H (Figure D1). However, the averaged Bowen ratio throughout the day was low (~0.68). Why would a hot and dry site still have a moderate amount of λE shown in Figure 2. 6E? From spectral analysis, higher contributions of heat and water fluxes at low frequencies indicated the transport of heat and moisture via large eddies (Figure 2. 5 & 7 green line). Interestingly, the power spectra of moisture peaked at an extremely low frequency (f = ~0.003) before cascading. The large eddies, produced through convection from the bare rectangular field (Figure 2. 2e), likely advected not only heat into our field, but also moisture-packed air parcels from further upwind irrigating and evaporating surfaces. Since these larger eddies are independent of the local internal boundary layer, they caused updrafts that allowed the

cool and moist air to be transferred near the surface (Butterworth et al., 2021). These combinations resulted in the higher and non-local λE observed in this case.

Despite the site characteristics, our results showed that larger eddies modified the surface energy balance and enhanced λE in all examined cases. Driven by the horizontal advection due to spatial heterogeneity of land surface conditions, the larger eddies transported additional heat and/or moisture from upwind regions. In cases with actively growing alfalfa (Case 1-4), the cool evaporating surface developed an IBL. Meanwhile the warmer air aloft, due to larger and drier eddies advected from the upwind, resulted in an extraction of H and enhance λE. In the case of a drier field, the non-local large eddies carried a substantial amount of moisture and some heat into the system, resulting in the higher-than-expected λE as observed in Case 5. Given the existence of the larger eddies, one aspect that requires further investigation is whether there was some non-zero vertical velocity at these times too. This is important as the potential vertical advection could also play a role in modifying the turbulent budget and subsequently, the surface energy balance. Lastly, even with explicit measurements like ours, there may be unaccounted energy and scalar fluxes (e.g. mesoscale processes or shift in wind direction). To better understand the system and boundary conditions explicitly, large eddy simulations would be beneficial to assess the study domain and minimal measurement points (Chu et al., 2021).

2.3.3. Does advection balance the vertical variation of heat flux?
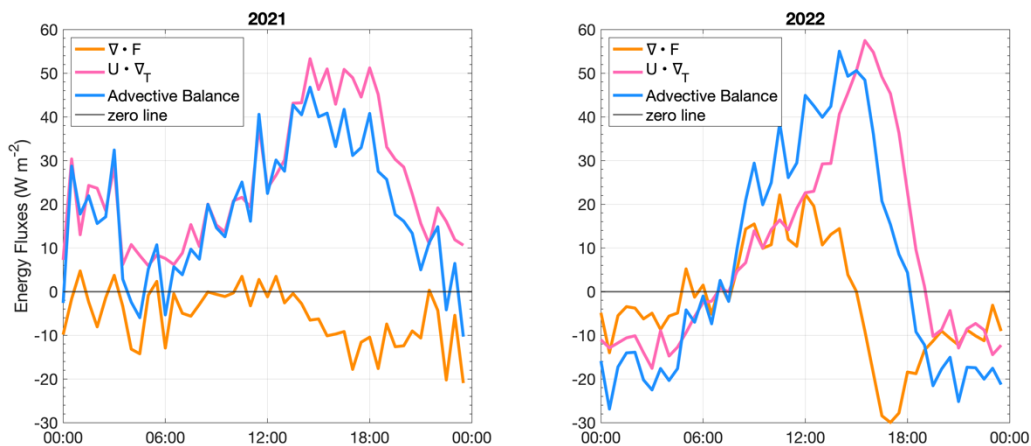
Figure 2. 8. Advective balance in 2021 and 2022. The advective balance (blue) is the sum of the horizontal heat advection (pink, $U \cdot \nabla_T$) and vertical heat flux divergence (orange, $\nabla \cdot F$) from canopy height to 3.96 m.

If we understand the surface energy balance better through the lens of advection, why not deploy more long-term horizontal measurements? This is certainly important, but as shown in Figure 2. 1 & 3, advection is as much of a scientific knowledge gap as a methodological challenge. Transect setup commonly requires the measurement of advective fluxes to be coming from a certain range of the wind direction, hence neglecting some advective fluxes that may be important. Following Eq. 3, we tested the idea of estimating advective fluxes with vertical flux divergence with a specific focus on the sensible heat budget (Eq. 3a) at the main tower. By comparing the balance between horizontal heat advection and vertical heat flux divergence, the diel advective balance was 18.8 W m⁻² averaged over Case 1-2 and -1.77 W m⁻² averaged over

Case 3-5 (Figure 2. 8). This seemingly perfect result is inconclusive. Specifically, despite the small differences in average, the half-hourly differences between the two components were large (Figure 2. 8 blue lines). Aside from the errors associated with how we computed the vertical flux divergence (e.g., linear extrapolation to canopy), it is also important to consider the assumptions we made during the analysis. For instance, our measurement height at 3.96 m could have been considerably smaller than the horizontal scale, potentially leading to a negligible horizontal flux divergence compared to its vertical counterpart (Finnigan, 1999). However, spectral analysis and thermal remote sensing observations indicated the presence of the large eddies, suggesting that vertical advection may not be negligible. Nonetheless, the findings from our study offer valuable insights for future implementations. To address the challenges associated with the vertical flux divergence computation, it might be beneficial to conduct an idealized assessment using different profiles above and below the canopy. Furthermore, large eddy simulation may be required to investigate the non-local effects.

2.3.4. Does λE evolve spatially under advection?

Up to this point, we have evaluated the fluxes at the main tower based on our transect measurements. In reality, energy and scalar fluxes are measured to represent the source/sink within a region of interest, usually less than several kilometers (Brunsell et al., 2011). However, what the flux towers "see" are not independent of the upwind area, and the upwind conditions can profoundly impact the local processes, especially for heterogeneous landscapes. On one hand, the processes sourced from heterogeneity can affect boundary layer dynamics and energy partitioning (McNaughton and Spriggs, 1986). Yet, it is challenging to quantify the effects with transect measurements. To address this, we used high-resolution satellite observations (e.g., thermal infrared) and combined them with latent heat fluxes measured at all three towers to gain a better understanding at a larger spatial scale, without sacrificing resolution at the temporal scale.

2.3.4.1. Wet to dry transition (Case 5)

In the cool/wet to hot/dry scenario (Table 2. 1., Case 5), ECOSTRESS LST showed a gradient alternating from cool/wet to hot/dry to cool/wet and then to the hot/dry alfalfa field (Figure 2. 9A). Previous advection field studies suggested that λE would undergo small or invariant changes with increasing downwind distance (McAneney et al., 1994; Baldocchi and Rao 1995; Zermeño-Gonzalez and Hipps, 1997). These findings validated the feedback interaction between atmospheric demand and stomatal regulations, which govern the invariant λE downwind. In Figure 2. 9A, our results showed that the λE was the highest near the field edge and decreased as the downwind distance increased. This finding contradicted findings in Baldocchi and Rao (1995) and Zermeño-Gonzalez and Hipps (1997), which reported an increasing λE near the field edge and an invariant λE with increasing downwind distance. There are two possible reasons for the different findings. First, at the surface discontinuity, the horizontal advective fluxes interacted with the surface, allowing the development of an internal boundary layer (Gash, 1986). As a result, fluxes at the edgy tower adjusted rapidly to the new equilibrium, hence, a higher λE. For the bouncer location, the advective processes were likely more blended with the underlying surface, resulting in a more uniform boundary layer condition. However, it is also possible that our "local" measurement near the field edge measured flux contributions from the upwind region (Baldocchi et al., 2022). This is confirmed by the averaged flux footprint at the edgy tower on this day, where the tower captured λE from the direct upwind field (Figure F1). Although the λE

was still decreasing from the bouncer to the main tower, the change was small (~6%), agreeing with findings from Baldocchi and Rao (1995) and Zermeño-Gonzalez and Hipps (1997). In this period, there were small and moderate, but consistent, $U \cdot \nabla_T$ and $U \cdot \nabla_Q$, respectively. Our results were consistent with the field studies that the stomatal regulation is not constant with increasing downwind distance (Zermeño-Gonzalez and Hipps, 1997). Specifically, in Figure 2. 9A, the surface conductance decreased with increasing downwind distance, and it remained nearly constant from bouncer to main tower. Note that although the higher LST may indicate the field as bare and dry (Figure 2. 9A left), there was sparse alfalfa growing at this time. Given the higher RNET at the main tower and an increasing H across towers, the alfalfa likely closed their stomates (i.e., lower surface conductance) and turned excess energy into H rather than into λE (Figure 2. 9A right). Omega factor in Figure G1 further confirmed this as both downwind towers showed stronger coupling strength, indicating the strong underlying stomatal regulation.

2.3.4.2. Mixed heterogeneity (Case 4)

Under a mixture of heterogeneity (Case 4) with different upwind conditions, ECOSTRESS LST showed a spatial gradient from upwind fields to the alfalfa field. Noticeably, the alfalfa field also exhibited noticeable intra-field variability in LST (Figure 2. 9B). Compared to the previous case, the overall λE trend in case 4 was still decreasing, except there was a small increase from bouncer to the main tower (~6%). Additionally, the magnitude of λE was higher due to the higher canopy density in this period. Similar to the previous case, the high λE near the field edge was due to the effect of flux footprint (Figure F1) as well as the adjustment to the boundary layer conditions. The RNET at the main tower was still the highest, ~5% higher than RNET at the bouncer tower. At the same time, there was an inverse pattern with H and λE across towers. As shown with the omega factor, the lower or suppressed λE at the bouncer tower was likely due to a more humidified atmosphere from $U \cdot \nabla_Q$, while the higher or enhanced λE at the main tower was more affected by the additional energy from the large eddies (Figure F1). Our finding of this downwind λE variation agrees with processes from McAneney et al. (1994) that there were two competing processes between stomatal regulations and atmospheric conditions. On one hand the stomatal opening would infer a higher λE, but on the other hand, the humid atmosphere with less demand would suppress λE. Overall, it seems that the stomatal regulation might have dominated the processes slightly more, which caused the slightly higher λE at the main tower.

A. Case 5

42
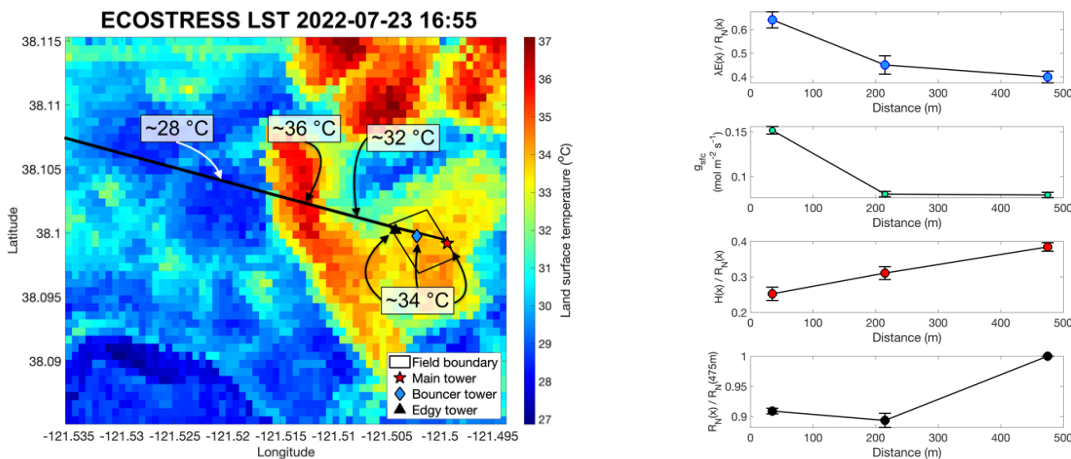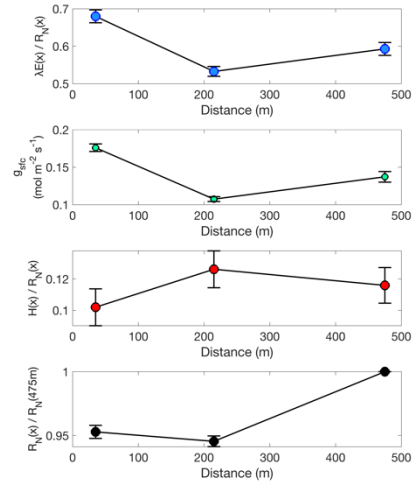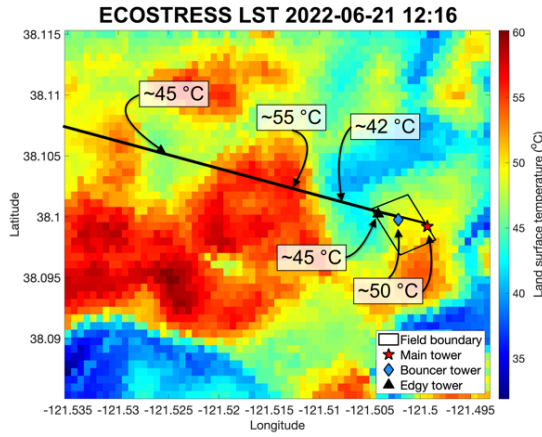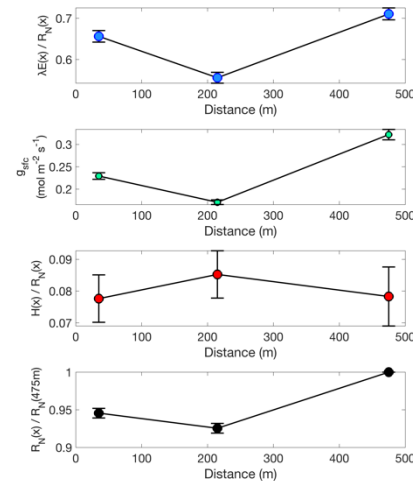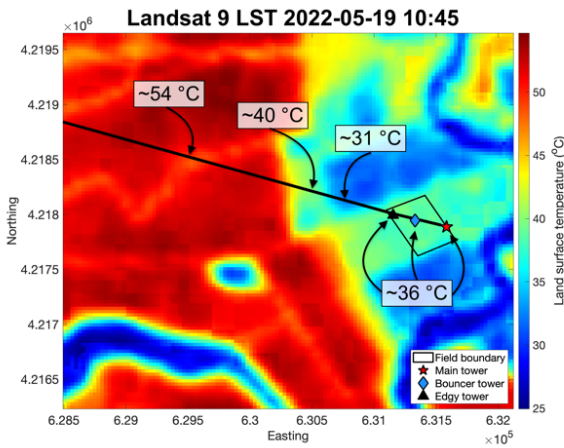
B. Case 4

C. Case 3

Figure 2. 9. Land surface temperature (LST) observations and the evolution of energy fluxes with respect to horizontal distance (x) for case 5 (A, top row), case 4 (B, middle row), and case 3 (C, bottom row). LST data are from ECOSTRESS 2022-07-23 16:55 (Panel A); ECOSTRESS 2022-06-21 12:16 (Panel B); and Landsat 9 2022-05-19 10:45 (Panel C). For LST observations, the black box is the field boundary, the black line is the primary wind direction, the red star is the main tower, the blue diamond is the bouncer tower, and the black triangle is the edgy tower. For the flux evolution, the blue circle represents the evolution of λE(x) normalized by RNET(x), the green circle represents the evolution of surface conductance (g_{sfc}), the red circle represents the evolution of H(x) normalized by RNET(x), and the black circle represents the variation of RNET(x) normalized by the RNET at the main tower. The error bars are plotted as one standard deviation. Surface conductance is derived by inverting the Penman-Monteith equation. Flux evolution is averaged between: (Panel A) 0900 to 1700 hours on 2022-07-23; (Panel B) 0800 to 1600 hours on 2022-06-21; and (Panel C) 0800 to 1600 hours on 2022-05-19.

2.3.4.3. Oasis effect (Case 3)

In an oasis-like system (Case 3), LST from Landsat 9 showed a generally decreasing LST gradient (Figure 2. 9C). Similar to the previous cases, λE at the edgy tower represented fluxes from the direct upwind field (Figure F1). However, λE at the main tower was ~17% higher than λE at the bouncer tower, even surpassing λE at the edgy tower. What caused the high λE at the further downwind location? During this time, the variation in H was too small to affect the varying λE. However, it seemed that λE was suppressed at the bouncer tower. Following McAneney et al. (1994), it is possible that the competing process was still at play since both $U \cdot \nabla_T$ and $U \cdot \nabla_Q$ were present at this time. Specifically, as shown in Figure G1, the bouncer tower is moderately decoupled with both stomatal regulation and available energy at play. Given that plants can humidify and affect the boundary layer growth (Cui and Chui, 2019), this location likely was adjusting to the new boundary layer conditions due to upwind evaporation. As a result, λE was suppressed with a humidified atmosphere due to advected moisture from upwind. For the main tower, a strong decoupling was observed, indicating that the non-local large eddies likely provided additional energy even to the further downwind location. As these large warm eddies advected along the mean wind direction into the cooler downwind fields, they penetrated the existing IBL, provided additional energy, and enhanced λE.

From these cases, with the help from thermal remote sensing, we confirmed the underlying processes, especially for the potential source of advection and large eddies. Through the interactions between advection and surface energy balance, there was a tipping scale between the two processes. On one hand, advection modified the atmosphere by adding additional moisture or heat to suppress or enhance the λE, respectively. On the other hand, the subsequent effect on humidity affected the surface (e.g. stomatal regulation), further affecting the λE. In parallel, spatiotemporal heterogeneity can affect the λE through non-local large eddies. However, when does one process become dominating or when do the two processes become compensated require distinctions in future studies. Specifically, the modification of boundary layer conditions sourced from heterogeneity should be further studied in the future. In our cases, we leveraged thermal remote sensing observation to visualize the potential source of the advection. However, being able to approximate or even pinpoint the effective source of the advective fluxes remains a challenge that needs to be tackled.

2.3.5. The infamous energy balance closure

From the five cases, we grouped the data by year and assessed the energy balance closure under advective conditions. The 2021 group included 13 days of half-hourly data and the 2022 group included 23 days of half-hourly data. By applying spectral correction, accounting for soil heat storage (Gs) and the photosynthetic energy storage (Sp) the energy balance closure improved by 15% (2021) and 11% (2022). However, there was still around 10-12% of underestimation in the turbulent fluxes (Table 2. 4.).

Table 2. 4. Changes in energy balance closure by accounting for various components in 2021 and 2022. The base case shows the raw data without any corrections. Gs is soil heat storage and Sp is photosynthetic energy storage. Each stage builds on the previous stage with a new component added. For example, stage 3 includes soil heat storage on top of the base case and spectral correction. Note that 2021 only has heat advection while 2022 has both heat and moisture advection.

Stage	2021		2022	
	Linear regression	Changes	Linear regression	Changes
1. Base case	y=0.73x+6.74 (r^2=0.98, n=624)	/	y=0.79x+13.9 (r^2=0.96, n=1104)	/
2. With spectral correction	y=0.83x+10.2 (r^2=0.96, n=624)	+ 10%	y=0.84x+17.8 (r^2=0.95, n=1104)	+ 5%
3. With Gs	y=0.85x+6.39 (r^2=0.97, n=624)	+ 2%	y=0.88x+11.2 (r^2=0.96, n=1104)	+ 4%
4. With Sp	y=0.88x+7.89 (r^2=0.97, n=624)	+ 3%	y=0.90x+12.7 (r^2=0.96, n=1104)	+ 2%
5. With advection	y=0.94x+10.4 (r^2=0.97, n=595)	+ 6%	y=1.00x+17.1 (r^2=0.96, n=1072)	+ 10%

By including all horizontal advective fluxes when the net radiation is greater than 75 W m^{-2}, the closure was further improved, but there were substantial amounts of hysteresis being introduced (data not shown). Note that only heat advection was included for 2021, while both heat and moisture advection were included for 2022. So, the question is should all measured advective fluxes be included? One economic wisdom that may be beneficial to apply to our unique bio-atmospheric interactions (i.e., transections) is the law of supply and demand. If someone missed buying a Lady Gaga concert ticket, they may be willing to pay more. However, this comes with conditionality as many have to consider incomes and other factors, triggering the law of diminishing returns. An ecosystem behaves similarly to a competitive market, where the energy supplied is also demanded commensurately. As the net available energy (net radiation minus ground heat flux) and additional energy (advection) increase, the demand from the atmosphere increases and the biosphere supplies in the form of turbulent fluxes. But the biosphere can only respond to a certain degree before it diminishes to prevent system failure. One response to the additional energy is to keep up by continuing the stomatal conductance (i.e., higher λE). The other response is to reduce stomatal conductance (i.e., lower λE) and turn the excess energy into sensible heat. The precise balance and timing of this trade-off remains unknown, and further research on how plants respond under different advective conditions has yet to gain momentum.

In our cases (Figure 2. 6), the system response might have already been reached when λE exceeded the net available energy. In other words, the biosphere stopped giving unwillingly despite the large amount of advective fluxes being supplemented simultaneously. With respect to the supply and demand relationship, instead of incorporating all the advective fluxes, we only

included them when: 1) the net radiation is greater than 75 W m^{-2} and 2) the sum of spectrally corrected H and λE were less than the net available energy. The inclusion of heat advection improved the energy balance closure by 6% (2021) while the inclusion of heat and moisture advection improved the energy balance closure by 10% (2022). Specifically, the inclusion of advective fluxes did not introduce much hysteresis or modify the general pattern of the regression while still improving the closure (Figure 2. 10). As shown here, advective fluxes played a key role in improving the energy balance closure. However, the improvement of closure was also achieved through other considerations, including spectral correction and accounting for Gs and Sp (Table 2. 4.).
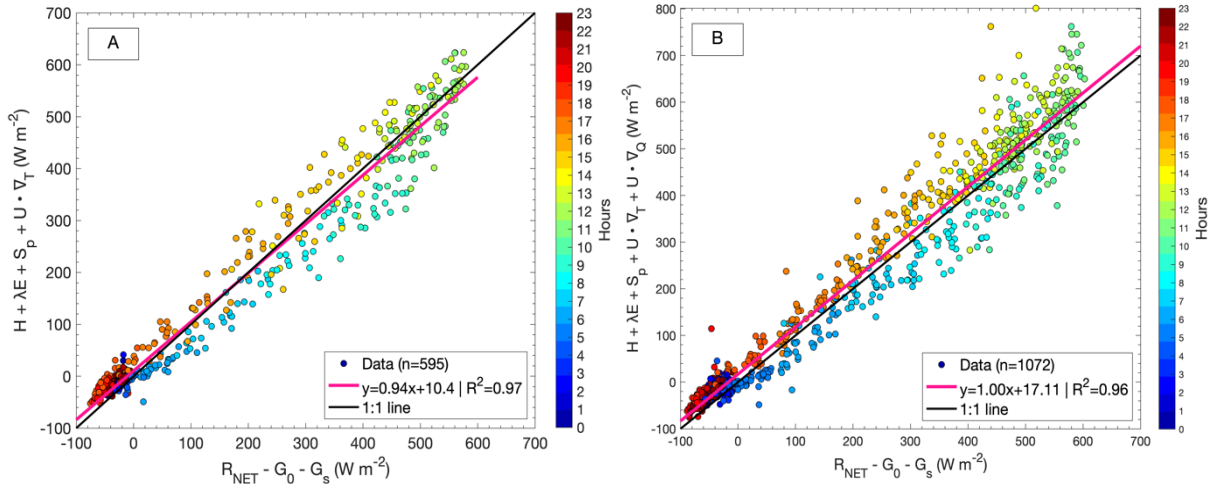
Figure 2. 10. Energy balance closure with spectral correction, soil heat (Gs), photosynthetic energy storage (Sp), and advective fluxes of heat and/or moisture (U·∇_T and U·∇_Q) for 2021 (A) and 2022 (B). The geometric mean regressions are y = 0.96x+8.35 (2021) and y = 1.03x+13.68 (2022).

2.3.5.1. A prelude for future energy balance problem solution

So, are we finally solving this energy balance problem after decades? Not quite, but we are getting closer. Complex and varying biometeorological controls across ecosystems can contribute to the lack of energy balance closure (Hulley et al., 2017). In reality, there is no silver bullet for achieving the energy balance closure. Each site is unique and requires a specific tailoring for addressing the energy imbalance (e.g. spectral filtering, non-local transport, complex terrain, etc). For our site, advection of heat and moisture certainly played an important role. But as late Dr. Leuning had emphasized the importance of 'know thy site', and slowly but surely, we started to understand that the seemingly small or negligible effects (e.g. Gs and Sp) are just as detrimental and can cumulatively lead to energy imbalance (Table 2. 4.). Researchers should also 'know thy instruments' as each may have different corrections and one must be mindful of certain corrections a sensor needs. For example, modern sonic anemometers, such as the ones in this study, commonly include crosswind correction while older generations do not.

It is important to note that although advection is shown to be a large source of energy flux at our site, it may not be as important for other sites. Given the increased access to high-resolution satellite remote sensing observations from multispectral (e.g. Sentinel-2 and Landsat) to thermal infrared (ECOSTRESS and Landsat), one should take advantage of what spatial coverage could

offer to disentangle the site-specific elements that may lead to the energy imbalance sourced from complex terrain and spatiotemporal heterogeneity (Hulley et al., 2017). Furthermore, measurements of net radiation and ground heat flux should be scrutinized, especially given the visible intra-field heterogeneity shown in Figure 2. 9. As eddy covariance "sees" fluxes within an extended region (i.e., flux footprint), consideration must be taken in terms of how representative are the measurements from the net radiometer and ground heat flux sensors placed by the tower. A gold standard measurement like eddy covariance still embodies flaws (e.g. spectral loss), however, we acknowledge that the spectral model (Kaimal et al., 1972) used here may not be perfect given the unique field configuration with varying atmospheric stability and field-to-field interactions. New spectral correction models such as (Gu et al., 2007) may provide valuable insights to account for signal attenuation in eddy covariance measurements. Lastly, biomass heat storage should also be considered, especially for tall and woody canopy (Gu et al., 2007).

2. 4. Conclusion

In this chapter, we investigated the role of spatiotemporal heterogeneity in surface energy balance using eddy covariance measurements. Specifically, differences in on-farm management have potential in modifying local boundary layer conditions due to horizontal scalar gradients (e.g., air temperature and water vapor concentration). To address this, we examined the effect of horizontal heat and moisture advection on surface energy balance at an alfalfa site over five study periods.

Despite the large fetch at this site, spatiotemporal heterogeneity induced advection and enhanced λE. By integrating spectral analysis with thermal remote sensing observations, we found the enhancement of λE was a product of both local and non-local effects. An internal boundary layer was developed locally due to a cooler surface from evaporative cooling and a warmer atmosphere aloft from advection. As a result of this the temperature inversion, heat extraction from aloft enhanced λE. Independently, upwind bare surfaces generated large eddies from convection that penetrated the internal boundary layer, intensified the heat extraction, and further enhanced λE. In our case, neither advection nor the small components should be assumed negligible. Energy balance closure was greatly improved by including the advective fluxes in addition to photosynthetic energy storage, soil heat storage, and spectral loss. Our results provide validations for remote sensing evapotranspiration models by incorporating assumed negligible components (i.e., storage terms) instead of preserving conservation with the traditional Bowen-ratio forced closure. Lastly, with a better understanding of advection and its complications, we provide insights for a new algorithm, which can help improve these remote sensing models that commonly treat pixels as an isolated columns rather than also considering the non-negligible effects of the lateral transport of heat and moisture.

Chapter 3 - Water scarcity in semi-arid California compromises perennial alfalfa's high yield and carbon sink potential[3]

Abstract

Alfalfa (*Medicago sativa L.)* a C3 and nitrogen fixing crop, offers high crop yield and carbon sink potential due to its perennial nature. As a prolific water user, its ability to thrive in warmer climates, such as semi-arid regions like California, is further enhanced with ample solar energy and irrigation. However, escalating challenges posed by water scarcity cast a shadow over alfalfa's ability to consistently provide high yields and serve as a robust carbon sink. In this study, long-term eddy covariance measurement, spanning from 2017 to 2023, was used to investigate the interannual energy, water, and carbon dynamics across various environmental conditions at an irrigated alfalfa site in California. Over 7 years, the average net ecosystem exchange was -544 g C m^{-2} y^{-1} accompanied by an average evaporation of 861 mm y^{-1}. In 2022, the net ecosystem exchange (-175 g C m^{-2} y^{-1}) and evaporation (722 mm y^{-1}) were markedly lower than other years. Notably, a significant reduction in photosynthesis occurred in 2022, while ecosystem respiration remained comparable across all years. In 2022, the significantly low evaporative fraction indicated that water stress during active summer growing seasons led to the overall low carbon and water budgets. Due to record low springtime precipitation, irrigation curtailment and limited water supply impeded crop growth, and likely also impacted crop yield. As the alfalfa continued to grow with a gradually declining biomass density, the insufficient soil water availability resulted in a higher crop stomatal closure. As a result, solar energy was used for sensible heat transfer rather than evaporation and carbon uptake processes. With depleting water resources, the dilemma of whether cultivation of water-demanding alfalfa should continue in these dry and drought prone regions (e.g., Imperial Valley, CA) remains largely unexplored.

3.1. Introduction

Alfalfa (*Medicago sativa L.*), a C3 nitrogen-fixing crop, is commonly grown in California (Lorenzo et al., 2020). This crop has advantages over other crops as it is perennial (i.e., long growing seasons), generating revenue from the multiple cuttings. These advantages are further amplified in a warmer climate, where plentiful solar energy and irrigation allow higher crop yield. Additionally, alfalfa can serve as a robust carbon sink through plant photosynthesis and provide climate change mitigation with its perennial system (Anthony et al., 2023; Ryu et al., 2019). However, at the heart of alfalfa's high yield and carbon sink potential lie the cost of water resources, which is a scarce commodity in warmer but often drier climates that depend on irrigation. So, is it still reasonable to harness alfalfa's high yield at the cost of greater water consumption? The significance of this question becomes particularly heightened in semi-arid regions such as California, where alfalfa agriculture has extensive acreage across the state (Putnam et al., 2000). The key issue of growing alfalfa is the heavy reliance on water resources, a commodity California frequently lacks, to achieve high crop yields under the perennial system.

To meet the growing demand of population and agricultural/dairy productions, more water is often used than is available (Famiglietti, 2014). In the past decade, California has experienced frequent and long-lasting droughts, leading to large fluctuations in water availability across years (Faunt et al., 2016). As a result, significantly lower surface water was available for irrigation (Liu et al., 2022). During periods of limited surface water, California farmers turned to groundwater to support ongoing irrigation (Scanlon et al., 2012). However, the increasing frequency and severity of droughts in California have also increased reliance on groundwater (Stewart et al., 2020). Thus, unstainable groundwater pumping has resulted in declining groundwater levels across California, leading to land subsidence in areas like the San Joaquin Valley (Carlson et al., 2020; Famiglietti, 2014). With less surface water, an increasing groundwater reliance, and subsiding land (Famiglietti, 2014), the cost of growing alfalfa in desert like environment perhaps ripples. However, the problem of alfalfa cultivations unfolds into a more complex matter…

Under future climate, frequent and severe droughts and less water supply are expected (Stewart et al., 2020). However, alfalfa is one of the top grown crops in California, supporting the state's ever-expanding dairy industry (Putnam et al., 2007). In 2023 alone, alfalfa (hay and hay/haylage) generated over \$1.6 billion in production value, and supported over 40 billions lbs. of dairy production (USDA/NASS, 2023). Alfalfa's capability to sequester atmospheric carbon raises the question of whether the climate mitigation potential outweighs the great water consumption. To answer this, in-situ micrometeorological measurement from eddy covariance can provide direct assessment of how alfalfa responds to various environment factors over the long term. In particular, this technique offers detailed and continuous measurements over a large sampling area, allowing insights on biosphere-atmosphere interactions through exchanges of energy, water (i.e., evaporation), and carbon fluxes (i.e., net ecosystem exchange) (Odum, 1969). Specifically,

net ecosystem exchange (NEE) comprises gross primary productivity (GPP) and ecosystem respiration (Reco), where GPP represents carbon assimilation via plant photosynthesis and the Reco represents the autotrophic and heterotrophic respiration from roots, soil, and litter (Baldocchi, 2020; Campioli et al., 2016). Such measurement is ideal to assess water use efficiency and photosynthetic activity of alfalfa agriculture as eddy covariance can link energy, water, and carbon fluxes with a broad range of environmental variables, including light source (Medlyn et al., 2011), temperature (Farquhar et al., 1980), precipitation (Weltzin et al., 2003), soil water availability (Novick et al., 2016), and plant physiology (Peñuelas and Filella, 2001), all of which have shown to affect carbon and water budgets (Baldocchi, 2020). Studies using direct eddy covariance measurements have showed the carbon budgets of alfalfa agriculture. Gilmanov et al. (2014) analyzed 5-site years of NEE and found that alfalfa was a strong carbon sink, sequestering on average around 980 g CO_2 m^{-2} per year. Menefee et al. (2022) showed that alfalfa, although a C3 legume crop, had similar net carbon uptake compared to productive C4 maize crop. The large carbon uptake is not surprising, as long growing seasons allow the perennial alfalfa to sequester a comparable amount of carbon with C4 corn, and more carbon than other C3 crops.

The carbon sinking potential of alfalfa is evident, but this depends on many conditions to sustain a healthy perennial system. Amiro et al. (2017) showed that short-term alfalfa-grass mixture resulted in a near neutral carbon uptake, where the decline of carbon uptake rate was attributed to the enhanced Reco after harvesting. As a result, large amounts of previously stored carbon in alfalfa/grass roots decomposed, yielding a near neutral carbon uptake due to respiration. In a rainfed alfalfa site, Wagle et al., (2019a) showed that the amount and timing of the rainfall regulated carbon uptake. During winter months, cold temperature and low solar radiation also were shown to inhibit carbon uptake rates, resulting in a carbon neutral or a small carbon source in the field. Although their results showed large carbon uptake of alfalfa at an annual scale, Wagle et al. (2019b) also showed the tight link between forage production and water use efficiency. In particular, at seasonal scale, higher forage production was associated with both higher carbon uptake and water loss (Wagle et al., 2019b). This underscores the complex and intricate relationship with alfalfa forage production, carbon fluxes, and water fluxes.

At the early stage of atmospheric research, Baldocchi et al. (1981a, 1981b) used the flux-gradient method to study carbon and water flux dynamics and found that carbon uptake rates were higher during active growth. The peak uptake occurred in spring and early summer due to optimal environmental conditions, including net radiation, turbulent mixing, and air temperature. On a daily scale, the crop's water use efficiency peaked in the morning and declined sharply by midday due to sensible heat advection, indicating the presence of stomatal regulation (Baldocchi et al., 1981a, 1981b). As sensible heat advection provided additional energy, evaporation rate for the well-watered alfalfa was greatly enhanced (Brakke et al., 1978; Rosenberg, 1969; Wang et al., 2023b). Under this advective condition, alfalfa seemed to have higher stomatal opening,

enabling evaporative cooling even during hot periods (Baldocchi et al., 1981a, 1981b). However, this can only be sustained with ample soil moisture, as one study has also shown that the presence of water stress under advective conditions led to higher stomatal closure and a suppressed evaporation (Wang et al., 2023a).

Behind alfalfa's high yield and carbon sink potential is at the apparent cost of water resources to sustain the perennial status. To our best knowledge, research regarding how long-term carbon and water fluxes vary in agricultural settings remain scarce. In this study, we leveraged long-term eddy covariance measurement, spanning from 2017 to 2023, at an irrigated alfalfa site in semi-arid California. At this natural laboratory, with fluctuating leaf area index due to periodic cuttings, extensive micrometeorological measurement enabled a comprehensive view of the energy, water, and carbon dynamics across various environmental conditions. This provides direct assessment of complications regarding growing water demanding alfalfa in semi-arid and drought prone regions. Furthermore, lessons learned here are also relevant for desert areas in the Imperial Valley of California, Arizona, and Idaho where much alfalfa is grown.

3.2. Method

3.2.1. Study Area

The study area is located in the Sacramento-San Joaquin River Delta (Lat: 38.0992, Lon: −121.4993), where a ~1400 km^2 historical wetland has been converted to agricultural land over the past 150 years (Atwater et al., 1979; Cloern and Jassby, 2012). At this site, a perennial alfalfa crop was grown, with periodic cuttings throughout the year and sheep grazing in the winter months (Figure 3. 1). The alfalfa (*Medicago sativa*, L) is a C3, perennial, nitrogen-fixing dicot, and water intensive legume crop with deep taproots. More details about the crop can be found in Alfalfa Agronomy Monographs (Fick et al., 1988; Sheaffer et al., 1988; Teuber and Brick, 1988). The study site has a Mediterranean climate (Köppen-Geiger climate classification: Csa) with a hot and dry summer and a cool and wet winter. In this climate, there are around 6 cuttings each year (Figure 3. 1). The air temperature in this region ranged from -3.9 ˚C to 42.8 ˚C from 2017 to 2023. In 2020 and 2022, ~3 days had high air temperature exceeding 40 ˚C. Precipitation usually happened towards the end of the year and last until the end of March in the following year. The annual total precipitation ranged from 175.9 to 446.9 mm. At our study site, the alfalfa crop was mainly sub-surface irrigated by an irrigation ditch adjacent to the field, and the applied irrigation water were not available to us. Sporadically, flash-flood was also used to irrigate the crop during the growing season. The site sits on degraded peatland soil with a Ryde-Peltier complex soil (50% Ryde, 35% Peltier, 5% Rindge, 4% Valdez, 3% Scribner, and 3% Venice based on the USDA-NCSS soil survey data at https://casoilresource.lawr.ucdavis.edu/gmap/).
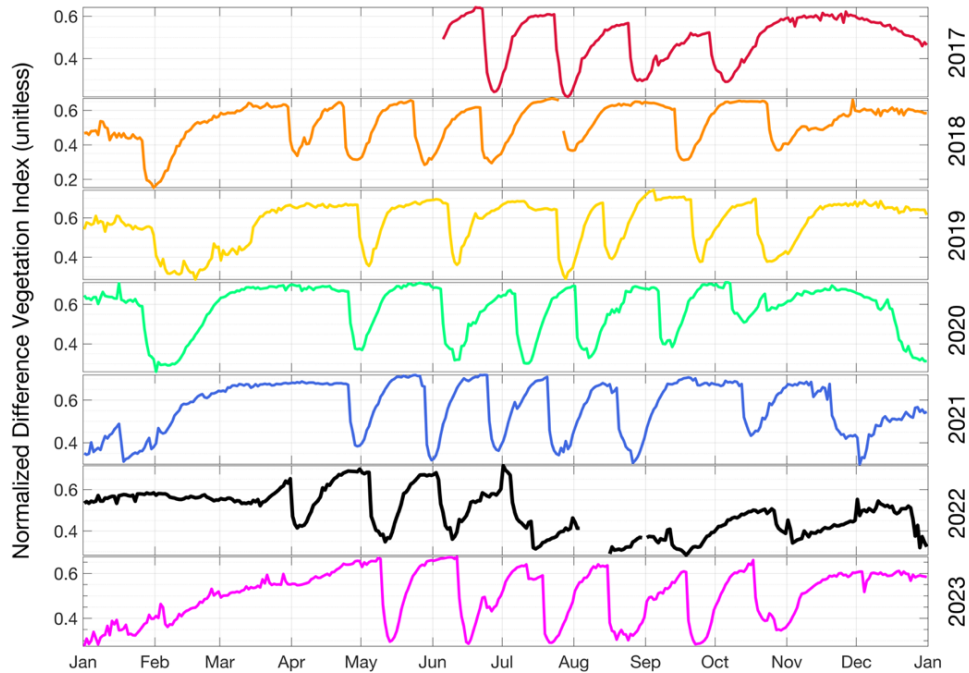
Figure 3. 1. Midday normalized difference vegetation index (NDVI) measured by Apogee SR-411 (red band: 650 nm and near infrared band: 810nm). The oscillating NDVI values from April to November each year indicate the periodic cuttings. Bad data prior to June 5th, 2017, were removed.

3.2.2. Eddy Covariance and Meteorological Measurements

Long-term eddy covariance and meteorological data were collected since 2016-08-13 with an eddy covariance flux tower, and we used data from 2017-01-01 to 2023-12-31 in this study. The flux tower is registered on AmeriFlux (Site ID: US-Bi1, Lat: 38.0992, Lon: −121.4993) and data can be accessed online (DOI: https://doi.org/10.17190/AMF/1480317). With the flat topography at the site and a predominant wind from the west to northwest, measurements were done on a scaffolding tower located ~475 m downwind of the field edge, allowing the idealization of eddy covariance measurements. A suite of the sensors used in this study can be found in Table I1. Eddy covariance data were collected to measure exchanges of energy, water, and carbon fluxes (Wang et al., 2023b). Specifically, a 3D ultrasonic anemometer (WindMaster 1590, Gill Instruments Ltd) was used to measure three orthogonal wind components (i.e., horizontal, lateral, and vertical) and the speed of sound. Alongside of the anemometer, an open path infrared gas analyzer (LI-7500, Li-COR) was used to measure water and CO_2 concentrations. All 20Hz data were filtered for spikes first. Then, a 2D coordinate rotation was performed to account for tilt errors and force the mean lateral and vertical components to zero (Kaimal and Businger, 1963). Additionally, time lag was computed to address the physical separation between the sonic anemometer and the gas analyzer. Afterwards, we computed half-hourly fluxes with the covariance of vertical wind speed and scalar (i.e., water and CO_2 concentration). Then, the

Webb-Pearman-Leuning correction was applied to water and CO_2 fluxes to account for fluctuations in air density (Webb et al., 1980). Lastly, a friction velocity (u*) filter was used to account for underestimation in NEE during low turbulence period. Here, we used a site-specific range to filter out fluxes with u* values less than 0.08 m s^{-1} and greater than 1.2 m s^{-1}. Alongside of eddy covariance data, half-hourly meteorological data were collected, including net radiation (NR-01, Hukseflux), aspirated and shielded temperature and relative humidity (HMP155, Vaisala), soil moisture (CS655, Campbell Scientific), and precipitation (TE525MM, Texas Electronics).

3.2.3. Gap-filling with artificial neural network

To assess the annual carbon and water budgets, missing data need to be gap-filled. Here, we used the artificial neural network (ANN) following Mofatt et al.(Moffat et al., 2007) to gap-fill heat (i.e., sensible heat flux, H), water (i.e., latent heat flux, λE), and carbon (i.e., net ecosystem exchange, NEE) fluxes. Explanatory variables for gap-filling were chosen for daytime and nighttime, including air temperature (TA), net radiation (RNET), photosynthetic active radiation (PAR), vapor pressure deficit (VPD), soil moisture (VWC), friction velocity (u*), seasonality (sine and cosine function of day of year), and days between cutting events (day_since_mow). Corresponding explanatory variables for each flux can be found in Table 3. 1. These explanatory variables were then divided into 15 clusters with k-means clustering, where data were sampled for 20 extractions of the training, testing, and validation. Lastly, each ANN structure was initialized for 10 times to avoid local minima. Compared to the measured fluxes, the ANN gap-filled fluxes yielded good results for H (y = 0.94x+0.55, R^2 = 0.93), λE (y = 0.97x+1.90, R^2 = 0.97), and NEE (y = 0.95x-0.07, R^2 = 0.93).

Table 3. 1. Explanatory variables for gap-filling sensible heat flux, latent heat flux, and carbon flux. The last column indicates the percentage of the gaps filled from 2017 to 2022.

	Explanatory variable		Percentage of filled data
	Daytime	Nighttime	
Sensible heat flux (n=105168)	TA, RNET, VPD, u*, day_since_mow, VWC at 2cm, seasonality	TA, day_since_mow, VWC at 2cm	28.8%
Latent heat flux (n=105168)	TA, RNET, VPD, u*, day_since_mow, VWC at 2cm, seasonality	TA, day_since_mow, VWC at 2cm	40.0%
Carbon flux (n=105168)	TA, PAR, VPD, u*, day_since_mow, VWC at 20cm, seasonality	TA, u*, day_since_mow, VWC at 20cm, seasonality	43.1%

3.2.4. NEE partitioning

NEE data were partitioned into GPP and Reco with ANN following Moffat et al.(Moffat et al., 2007). Nighttime measurements were used to estimate daytime Reco based on explanatory variables, including TA, PAR, VWC at 2cm, u*, day_since_mow, and seasonality. All data were divided into 8 clusters with 20 extractions for training, testing, and validation and 10 initializations. Similar to the popular partitioning method from (Reichstein et al., 2005), our ANN partitioning approach assumes similar behavior between nighttime and daytime Reco, which would lead to systematic biases. For example, due to radiative cooling at nighttime, a stable boundary layer can be formed, inducing entrainment jets, and creating nighttime Reco pulses that would not exist in daytime Reco. Nevertheless, by using multiple variables, this approach allows good representation of our alfalfa site that went through many growth, senescence, and harvest cycles. Partitioned NEE from the ANN approach were used in the analysis as its partitioned nighttime Reco compared well with measured nighttime Reco ($y=0.63x+2.02$, $R^2 = 0.63$).

3.2.5. Irrigation Curtailment and surface water allocation

In the study region, the water resource is critical for agricultural production. However, with limited water resources, the available water is distributed based on appropriative water rights (e.g., pre- and post-1914). Our study site, which is in the Reclamation District #756, has post-1914 appropriative water rights (Hanemann, 2014). This means that it is subject to water use regulations and priorities set by the State Water Resources Control Board (SWRCB), including irrigation curtailment under droughts. With anomalous data in 2022 that corresponded with ongoing drought, we accessed reclamation records on water delivery information from SWRCB regarding irrigation curtailment (https://www.waterboards.ca.gov/drought/delta/#tableau) and surface water allocation from the State Water Project (https://water.ca.gov/Programs/State-Water-Project/Management/SWP-Water-Contractors). Data regarding curtailment orders, available from August to October 2021 and May to October 2022, and water allocation from State Water Project can be found in Table 3. 2.

Table 3. 2. Irrigation curtailment statues and State Water Project water allocation from 2017 to 2023.

Year	Irrigation curtailment (Reclamation District #756)	Water allocation (across state)
2017	Not available	85%
2018	Not available	35%
2019	Not available	75%
2020	Not available	20%
2021	August 20th and 27th	5%
2022	July 6th, 12th, 19th and 26th August 2nd, 9th, 16th, and 23rd	5%
2023	Not available	100%

3.3. Results and Discussion

3.3.1. Annual ecosystem carbon budget and surface energy balance

Located in the Sacramento-San Joaquin Delta, the alfalfa field is perennial with growing seasons predominantly from April to October each year. With the Mediterranean climate, the sunny and rainless summer growing seasons allowed the irrigated alfalfa to thrive in this area, and there were around 6 cutting cycles each year (Figure 3. 1).

Table 3. 3. Annual sum of carbon, evaporation (converted from latent heat flux measured by eddy covariance), sensible heat flux, and net radiation from 2017 to 2022.

	2017	2018	2019	2020	2021	2022	2023
NEE ($g\ C\ m^{-2}\ y^{-1}$)	-541	-546	-775	-764	-522	-175	-486
Evaporation (mm)	864	862	928	881	933	722	839
Sensible heat ($MJ\ m^{-2}$)	399	484	240	377	366	964	688

Net radiation (MJ m^{-2})	3.25x10^3	3.27x10^3	3.37x10^3	3.27x10^3	3.35x10^3	3.32x10^3	3.41x10^3

The total annual carbon fluxes ranged from -175 to -775 g C m^{-2} y^{-1} with a mean of -544 g C m^{-2} y^{-1}. Although the alfalfa field remained a carbon sink across the 7 years, carbon sink strength (i.e., NEE) in 2022 was noticeably weaker than other years (Table 3. 3.). This decline of NEE in 2022 was attributed to the sharp decline of gross primary productivity (GPP) as the ecosystem respiration (Reco) was comparable across years (Figure J1). Following the decline of NEE, evaporation in 2022 was the lowest, around 140 mm lower than the mean total evaporation of 861 mm (Table 3. 3.). Figure 3. 2 shows the relationship between gross primary productivity (GPP) and evaporation from April 1st to October 31st. Throughout this period, high GPP coincided with high evaporation, especially when NDVI was high from May to September. From all years, as evaporation increased, so did GPP, indicating the influence of water availability on ecosystem productivity. The magnitude of this was particularly stronger at higher NDVI, demonstrating that biomass density and vegetation health affected GPP and evaporation (Figure 3. 2, top). Disregarding 2017, high GPP and evaporation were observed from May to September as a result of the higher net radiation, sufficient soil water availability, and higher NDVI (Figure 3. 2, bottom). However, data in 2022 were different. Specifically, more points were clustered at low GPP and low evaporation with NDVI generally less than 0.5. Compared to other years, in 2022, high GPP and evaporation were only observed in April and May, highlighting the coupling between carbon and water fluxes and potential water stress.
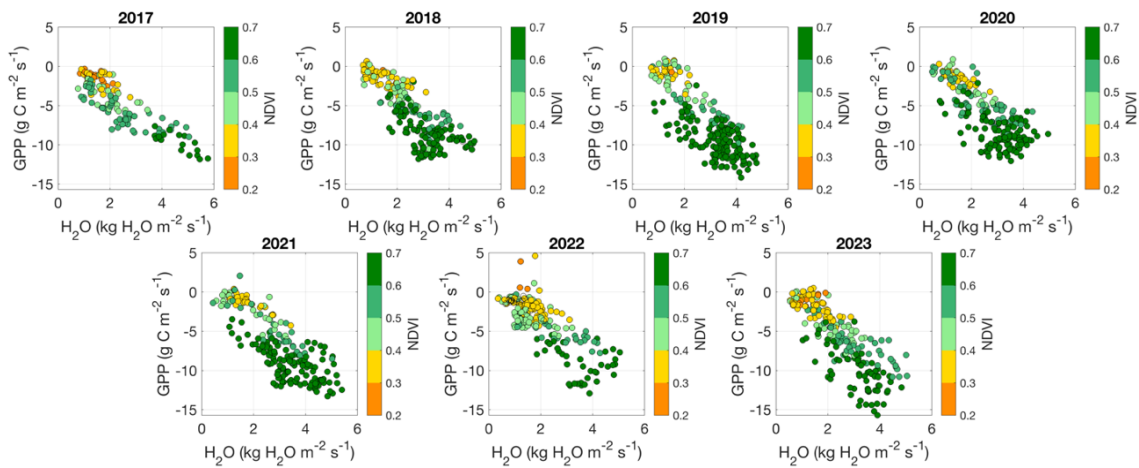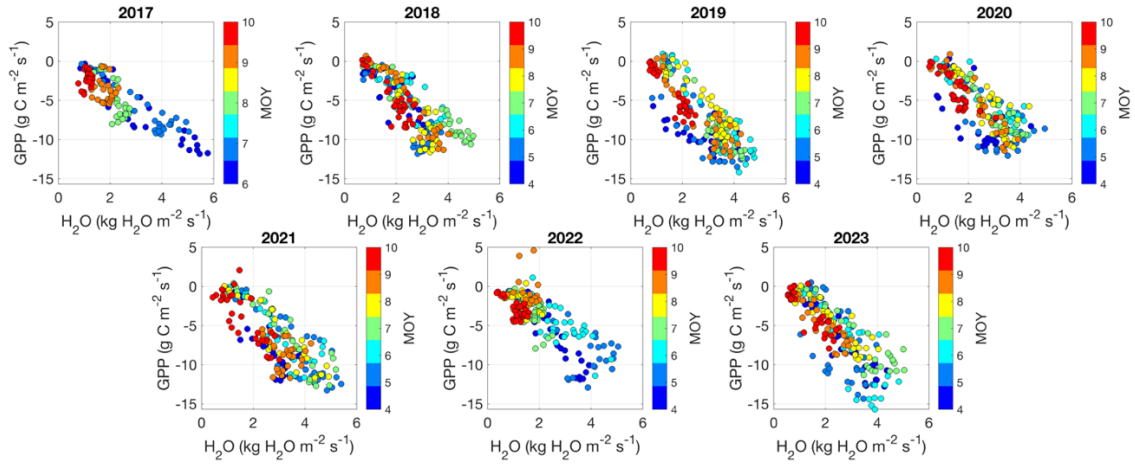
Figure 3. 2. (top) scatter plots of gross primary productivity (GPP) vs. water vapor fluxes as a function of NDVI. Data are shown as daily daytime (10:00 to 18:00) sum from April 1st to October 31st. (bottom) same as the top panel, except the z-axes are as month of year (MOY). Note that in 2017, bad NDVI data prior to June 5th were removed, hence the sample size was smaller for this year.

3.3.2. Interannual variability in environmental factors

57
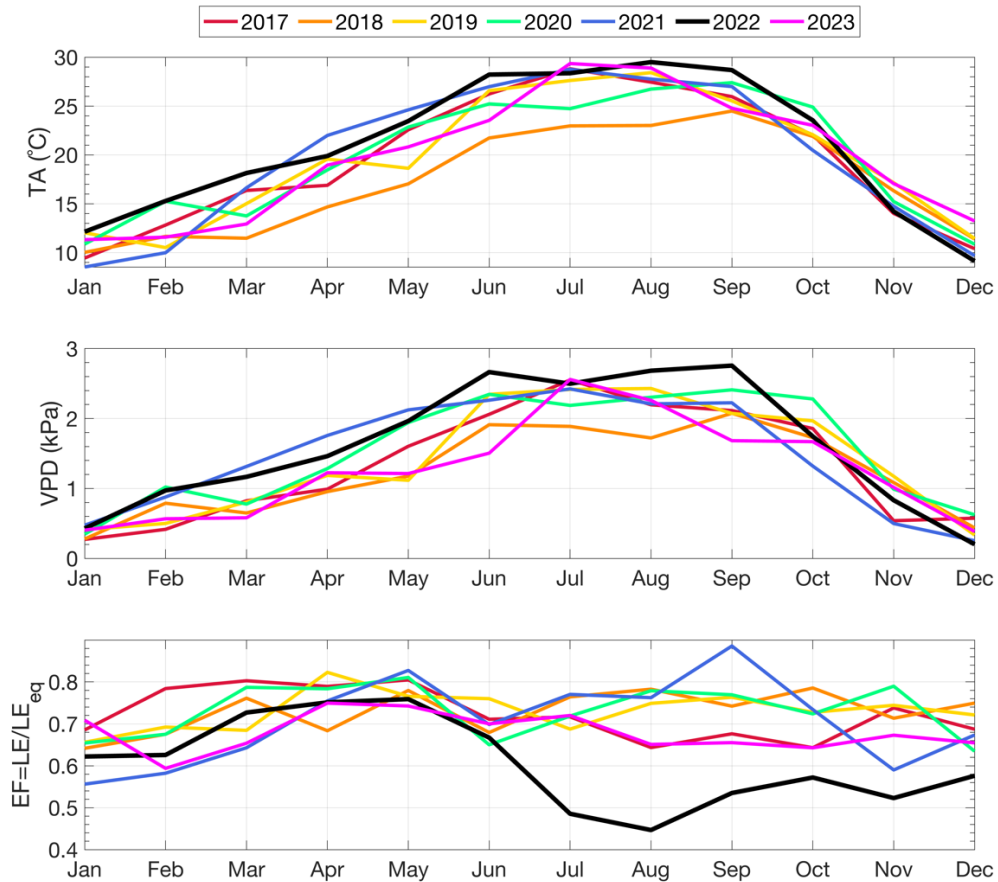
Figure 3. 3. Monthly hydrometeorological variables, including air temperature (top panel), vapor pressure deficit, VPD (middle panel), and evaporative fraction (bottom panel) over the course of 7 years. All data are shown as monthly mean averaged from daily daytime mean from 10:00 to 18:00 local time.

Across the 7 years, air temperature (TA), vapor pressure deficit (VPD), and evaporative fraction (EF, calculated with latent heat flux divided by its equilibrium part) were assessed (Figure 3. 3). It is worth re-elaborating that alfalfa has deep taproots, allowing the crop to access water deep down under the Delta Islands. While it is difficult to measure the root weighted soil moisture, EF via eddy covariance serves as an direct indicator to assess how soil moisture deficit or physiological stress may limit stomatal regulation, transpiration, and photosynthetic activity (Gentine et al., 2011). Monthly mean daytime TA and VPD were comparable across years. During the summer growing season of 2022, TA and VPD were slightly higher compared to other years in June, August, and September. While higher TA and VPD may suggest a higher evaporation rate at an irrigated alfalfa field, EF data suggested otherwise. Noticeably, after June, EF in 2022 declined rapidly with a monthly mean daytime EF ranging from 0.44-0.56 from July to November, compared to other years where EF were ~0.66 and above. The overall lower EF indicated either a decrease in soil moisture or an increase in net radiation (Lhomme and Elguero, 1999). With comparable net radiation values across years (Table 3. 3.), it was likely that the alfalfa was experiencing water stress, reflected through the overall lower EF (Figure 3. 3).

3.3.3. Interannual variability in ecosystem fluxes
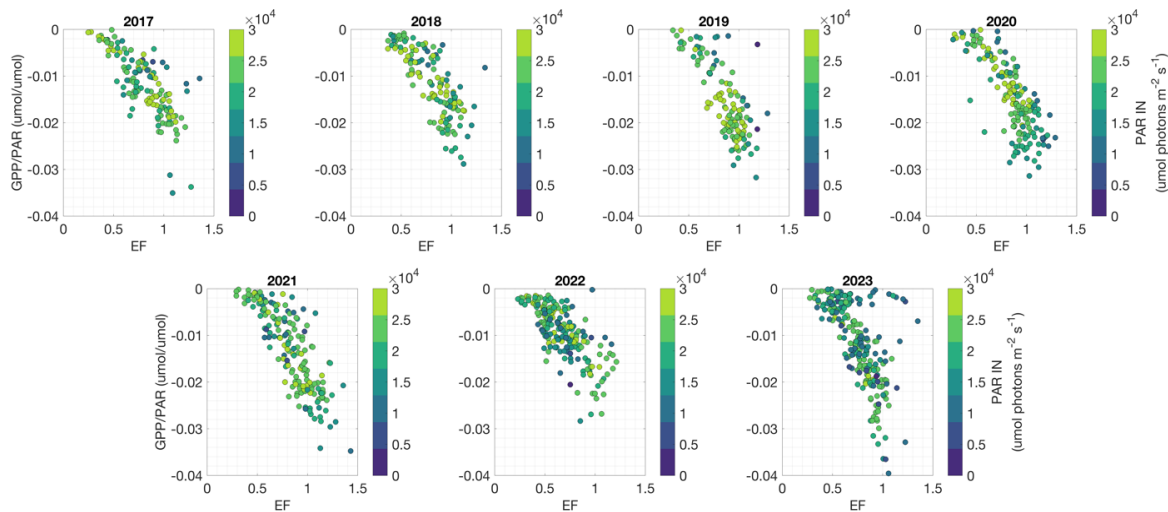
Figure 3. 4. Scatterplots of daily daytime (10:00 to 18:00) sum of gross primary productivity (GPP) normalized by photosynthetic active radiation (PAR) in micromole of CO2 per micromole of photon vs. evaporative fraction (EF). Z-axis shows the daily daytime sum of PAR (colorbar).

The significantly deviated EF in 2022 might be a result of the possible water stress, however, do other ecosystem fluxes indicate water stress as well? In terms of ecosystem respiration, we did not see any significant variations from year to year, and the reduction of NEE in 2022 was

mainly contributed to the lower photosynthesis (Figure J1). In Figure 3. 4, we normalized photosynthesis (i.e., GPP) by photosynthetic active radiation and compared it with evaporative fraction (EF) as a function of the incoming PAR. From 2017 to 2021 and in 2023, a strong positive relationship was exhibited between the two variables, indicating an efficient use of light for photosynthesis and evaporation. Similar to Figure 3. 2, this showed the strong coupling between carbon and water fluxes, likely due to well-watered condition. However, data in 2022 did not follow a similar pattern, as there was a higher density of points clustered in the region where photosynthesis and EF were low. This low EF is indicative of higher stomatal closure due to soil water deficit, and we inspected stomatal regulation with canopy omega coefficient (Ωc), computed via Eq. 1:

$$\lambda E = \Omega c \cdot \lambda E_{eq} + (1 - \Omega c) \cdot \lambda E_{imp} \qquad \qquad \text{Eq. 1}$$

where λE_{eq} is the equilibrium evaporation, and λE_{imp} is the imposed evaporation. λE_{eq} is dependent on radiation control while λE_{imp} is proportional to stomatal conductance. As a result, a high Ωc value indicates a strong energy control, and a lower value indicates a strong stomatal control. A detailed description on Ωc can be found in (Jarvis and McNaughton, 1986). In 2022, despite the lower biomass density (Figure 3. 1), the low Ωc indicated the stronger stomatal regulation compared to other years (Figure 3. 5). In a well-irrigated alfalfa, we would expect a higher potential evaporation rate due to ample water availability (Eichelmann et al., 2018), consequently leading to a higher Ωc attributed to energy control. However, with a broad spectrum of Ωc values spanning 7 years, Ωc for 2022 stood out with a consistently low value at ~0.37 (Figure 3. 5), indicating the higher stomatal closure due to water stress. Additionally, this lower Ωc and canopy density also affected sensible heat transfer, in which reduced evaporation led to large differences in sensible heat flux (Table 3. 3.). In particular, the alfalfa experienced higher stomatal closure, which in turn reduced EF, decreased evaporative cooling, and resulted in a larger temperature gradient (Appendix K). Consequently, this larger temperature gradients, induced by higher stomatal closure, created favorable conditions for sensible heat transfer, where more available energy was partitioned into sensible heat flux. This further reduced evaporation and carbon uptake rates (Table 3. 3.). With detailed information between GPP and EF, results presented here can also be used to assess GPP with satellite remote sensing, especially for models that already incorporate EF (e.g., Fisher et al., 2020).

3.3.4. Springtime precipitation and irrigation curtailment influenced carbon sink strength
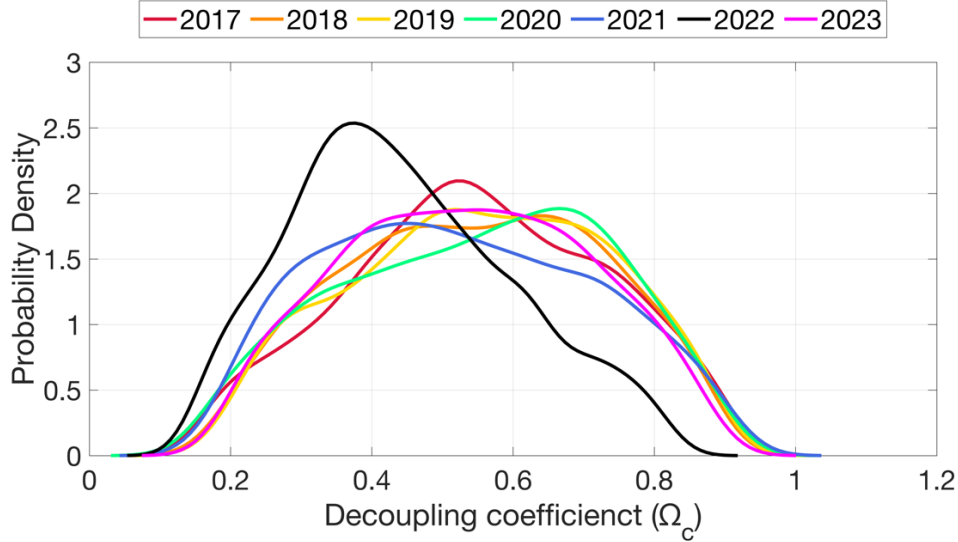
Figure 3. 5. Probability density function of omega coefficient (symbol) from 2017 to 2023. All data were filtered in between the 5th quantile to the 95th quantile.

As shown, changes of NEE, EF, and sensible heat transfer in 2022 were attributed to stronger stomatal regulation (Figure 3. 5). However, behind the complex mechanisms of biosphere-atmosphere interactions linger the question: what led to the stronger stomatal regulation? Needless to say that to sequester a lot of carbon bears the simultaneous consequences of losing water through evaporation, and neither can be achieved without enough soil water availability (Cowan and Farquhar, 1977; Tanner and Sinclair, 1983). The perennial alfalfa requires large amount of irrigation water, to inspect the potential water stress, we used a pedotransfer function (Appendix D) and estimated the soil water potential ($-\Psi_S$) at 20 cm (Figure L1). Generally, $-\Psi_S$ increased from April, indicating the increasingly drying soil. Compared to other years, $-\Psi_S$ in 2020 and 2022 stood out with values exceeding 0.1 MPa starting from mid-May. After April 2022, $-\Psi_S$ continuously increased at a faster rate before reaching its maximum in October, suggesting the relatively dry soil was caused by ongoing water stress. It is important to note that with alfalfa's deep taproot, $-\Psi_S$ at 20 cm may not be representative of the entire water flow. However, when combining with EF data, $-\Psi_S$ at this depth further supported expectation of the crop water stress. In 2022, the low EF, from higher stomatal closure, indicated crop water stress, which might have been induced by reduction in precipitation and irrigation, reflected in the higher $-\Psi_S$ (Figure L1).

For most years, ample precipitation happened towards the end of the year and in early spring, except from 2020 to 2022, where statewide (Figure M1) and site level (Figure M2) precipitation showed less frequent springtime precipitation due to ongoing drought (DeFlorio et al., 2024). In the tug-of-war between water scarcity and agricultural production, the low precipitation in drought periods led to a reduced surface water allocation to the farmers by the State Water

Project (Table 3. 2.). Compared to other years, 2021 and 2022 had significantly lower surface water allocation delivery (Table 3. 2.), limiting water available for irrigation. Additionally, curtailment orders were imposed in late August 2021, and from July 6th to August 23rd, 2022 (Table 3), further restricting irrigation. Due to curtailment, less surface water was available for irrigation, leading farmers to pump more groundwater, which in turn resulted a sharp decline in groundwater storage in San Joaquin basins in 2021 (Liu et al., 2022). Although their study did not report groundwater storage in 2022, it is likely that the declining trend was present given the low water allocation (Table 3. 2.) and precipitation (Figure M1 & 2) in this year. The withdrawal of groundwater at the beginning of the drought years in 2020 and 2021 might have supported ongoing irrigation, explaining the normal amount of NEE and evaporation in these years (Table 3. 3.). In 2022, irrigation curtailment and declining groundwater storage since 2020 likely limited groundwater supplies, hence leading to a reduction in irrigation water supply. However, it is unknown whether the Sustainable Groundwater Management Act (SGMA) imposed regulations to prevent overdrafts. Nonetheless, albeit the lack of irrigation information at the field, water use data from state agency along with EF data clearly showed the pronounced crop water stress in 2022 (Figure 3. 3), explaining the overall reduced carbon sink strength (Table 3. 3.).

Compared to the monthly sum of NEE from 2017 to 2021, NEE in 2022 and 2023 were noticeably different (Figure 3. 6 – left). In 2022, the field was mostly a carbon sink, except for July, August, September, November, and December. The field switched back to a carbon sink again in October with the incoming precipitation (Figure M1 & 2). Additionally, from April to September in 2022, the monthly sum of NEE ranged from ~20-186% higher than the same months from 2017 to 2021 (Figure 3. 6 – right). In 2022, the declining carbon sink strength also coincided with the simultaneously declining EF (Figure 3. 3), attributed to summertime irrigation curtailment, which in turn forced the stomata (Figure 3. 5) to close and inhibited photosynthesis (Table 3. 3.). Prior to July, lower springtime precipitation inhibited photosynthesis while the proceeding curtailment orders further inhibited photosynthesis via limited irrigation, resulting in an increasingly larger differences in NEE. Crop age may have contributed to low NEE in 2022 as alfalfa growth typically declines after the 5th year (Hu et al., 2020). Yet, NEE in 2023 did not exhibit a further declining trend likely due to the ample water supplies (Table 3. 2. and Figure M1). In this year, the carbon sinking strength was comparable to that from 2017 to 2021, especially during the peak growing season from May, and July to September. Unlike 2022, the field in 2023 was a moderate carbon source from January to March due to the lower canopy density succeeded from the previous year (Figure 3. 1).
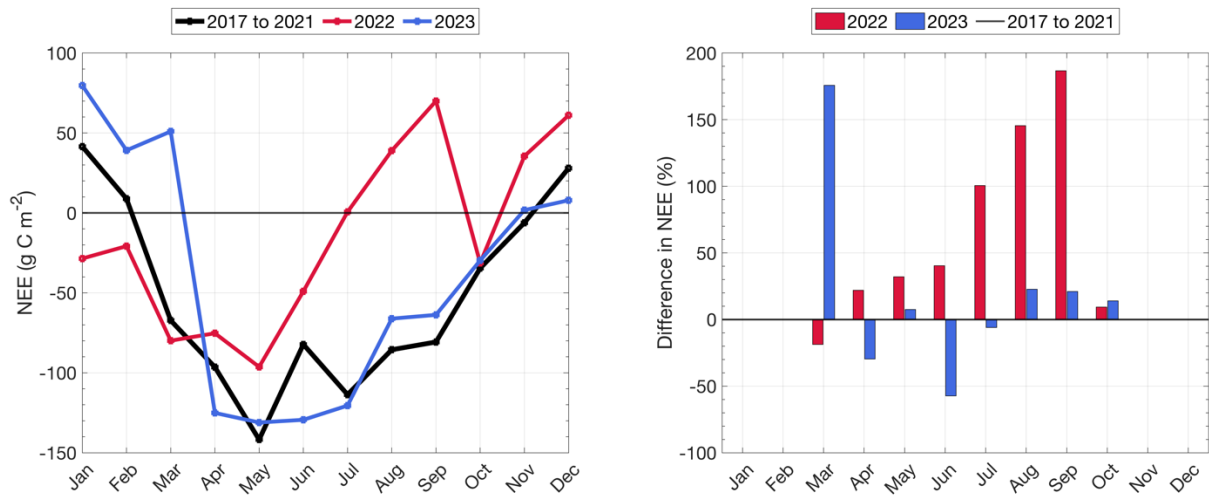
Figure 3. 6. **Left** – monthly sum of Net Ecosystem Exchange (NEE) from 2017 to 2021 (black), in 2022 (red), and in 2023 (blue); **right** – percentage differences of NEE in 2022 (red) and 2023 (blue) compared to NEE from 2017 to 2021 (black line at zero). Data in Jan, Feb, Nov, and Dec were removed for percentage calculation.

Although our study site was not rainfed, reduced springtime precipitation led to less water available for irrigation, which in turn greatly affected the carbon sink strength and evaporation throughout 2022. The irrigation curtailment and limited water supply in the active growing season notably affected the crop growth (Figure 3. 1), and likely impacting the crop yield as well. In this year, the significantly reduced EF (as shown in Figure 3. 3) and higher stomatal closure (as shown in Figure 3. 5) indicated crop water stress, which contributed to the noticeable decrease in carbon sink strength and evaporation (Table 3. 3.).

3.3.5. Future directions

The challenge of water management amid climate change is pressing. Our results showed that growing alfalfa might be less effective for sequestering carbon under limited water resources. While cultivating alfalfa in California is driven by its high yield potential, largely due to the Mediterranean climate, which allows many cuttings each year, this high yield comes at the cost of substantial water use. Our findings demonstrated that the carbon sink potential did not hold up as a result of water scarcity, which likely also affected the anticipated high yield. So, even though alfalfa is deep rooted and can have access to water deep under the land surface, these data show that the crop was not able to compensate by accessing this water source in a sufficient manner to maintain high productivity.

Although our analysis is limited at site-level, we expect long term climate variability also affects other regions. Similar analysis can also be done whether using eddy covariance or remote sensing data to better understand how the carbon and water budgets are changing regionally and

62

globally. As the 5th largest economy in the world, the fate California's agriculture is intricately tied to the uncertain future climate.

Questions arise as how to share and allocate water efficiently, especially in times of prolonged drought when less surface water is available, and groundwater becomes the primary source for irrigation. The reality is that water may not be available each year, and the groundwater certainly cannot be pumped infinitely. Despite efforts of groundwater regulation from SGMA, the ongoing depletion of groundwater storage and uncertainty in future climate pose important questions regarding the continued allocation of water for alfalfa cultivation in California. For example, one lingering question is the crop water use of alfalfa agriculture in arid regions like Imperial Valley, as highlighted previously (Baldocchi et al., 2019). In such arid climates, conditions may be even worse compared to our study region. In oasis-like environments, where green irrigated fields are surrounded by desert, sensible heat advection can often induce even higher evaporation rates, prompting further questions regarding the justification for cultivating the already water-demanding alfalfa in these desert-like regions.

While alfalfa agriculture can sequester carbon at the field level, it is important to recognize that the harvested dry matter is also consumed and then respired back to the atmosphere elsewhere. Specifically, as alfalfa is commonly used for dairy and other livestock productions (Wang et al., 2016), methane emission stemming from animal consumption may potentially outweigh the carbon sequestered in agricultural fields, resulting in a net increase in carbon emissions at a broader scale (Johnson and Johnson, 1995). While our study did not include life cycle analyses, since it is beyond the scope of our research, it highlights a knowledge gap that warrants further investigation. In particular, the interconnection between crop growth and animal consumption should be considered in future study to better understand the net carbon balance.

3.4. Conclusion

Long term carbon and water budgets remain largely unknown for alfalfa agriculture in California. In this chapter, we investigated this problem using long term eddy covariance measurements at an irrigated alfalfa site in the Sacramento-San Joaquin River Delta region.

Due to its perennial nature, alfalfa's yield and carbon sink potentials are promising, especially in warmer climates such as semi-arid California with ample solar energy and irrigation. However, increasing water scarcity casts a shadow over alfalfa's ability to consistently provide high yields and serve as a robust carbon sink. In this study, we analyzed 7 years of eddy covariance data, from 2017 to 2023, and examined interannual variability in energy, water, and carbon fluxes at an irrigated alfalfa site in California. In 2022, net ecosystem exchange (-175 g C m^{-2} y^{-1}) and evaporation (722 mm y^{-1}) were significantly lower compared to other years. By linking ecosystem functions with hydrological changes, our results revealed that, due to low springtime precipitation, irrigation curtailment and limited water supply strongly affected the carbon and water budgets during the active summer growing season in 2022. Specifically, water stress in this

year, supported by the significantly low evaporative fraction, impeded crop growth and resulted in a reduced carbon sink strength and evaporation. With declining canopy density and higher stomatal closure, a large amount of energy was used for sensible heat transfer (964 MJ m^{-2}) as opposed to for carbon uptakes and evaporation in 2022. In a fast-changing climate with limiting water resources, how to share and allocate water efficiently in California's agriculture remain to be an important question. This is heightened especially in times of prolonged drought when less surface water is available, and groundwater becomes the primary source for irrigation. Furthermore, whether cultivating water intensive alfalfa should continue in these dry and drought prone regions remains to be largely unexplored.

Reference

Alfieri, J., Kustas, W., Prueger, J., Hipps, L., Evett, S., Basara, J., Neale, C., French, A., Colaizzi, P., Agam, N., Cosh, M., Chavez, J., Howell, T., 2012. On the discrepancy between eddy covariance and lysimetry-based surface flux measurements under strongly advective conditions. Publications from USDA-ARS / UNL Faculty.

Alfieri, J., Kustas, W.P., Anderson, M., Sivakumar, M., 2018. A Brief Overview of Approaches for Measuring Evapotranspiration. https://doi.org/10.2134/agronmonogr60.2016.0034

Alfieri, J.G., Kustas, W.P., Prueger, J.H., McKee, L.G., Hipps, L.E., Bambach, N., 2022. The vertical turbulent structure within the surface boundary layer above a Vineyard in California's Central Valley during GRAPEX. Irrig Sci. https://doi.org/10.1007/s00271-022-00779-x

Amiro, B.D., Tenuta, M., Gervais, M., Glenn, A.J., Gao, X., 2017. A decade of carbon flux measurements with annual and perennial crop rotations on the Canadian Prairies. Agricultural and Forest Meteorology 247, 491–502. https://doi.org/10.1016/j.agrformet.2017.08.039

Anderson, M.C., Allen, R.G., Morse, A., Kustas, W.P., 2012. Use of Landsat thermal imagery in monitoring evapotranspiration and managing water resources. Remote Sensing of Environment, Landsat Legacy Special Issue 122, 50–65. https://doi.org/10.1016/j.rse.2011.08.025

Anderson, M.C., Kustas, W.P., Norman, J.M., Hain, C.R., Mecikalski, J.R., Schultz, L., González-Dugo, M.P., Cammalleri, C., d'Urso, G., Pimstein, A., Gao, F., 2011. Mapping daily evapotranspiration at field to continental scales using geostationary and polar orbiting satellite imagery. Hydrol. Earth Syst. Sci. 15, 223–239. https://doi.org/10.5194/hess-15-223-2011

Anthony, T.L., Szutu, D.J., Verfaillie, J.G., Baldocchi, D.D., Silver, W.L., 2023. Carbon-sink potential of continuous alfalfa agriculture lowered by short-term nitrous oxide emission events. Nat Commun 14, 1926. https://doi.org/10.1038/s41467-023-37391-2

Arya, P.S., 2001. Introduction to Micrometeorology. Elsevier.

Atwater, B.F., Conrad, S.G., Dowden, J.N., Hedel, C.W., MacDonald, R.L., Savage, W., 1979. History, landforms, and vegetation of the estuary's tidal marshes 347–386.

Aubinet, M., Feigenwinter, C., Heinesch, B., Bernhofer, C., Canepa, E., Lindroth, A., Montagnani, L., Rebmann, C., Sedlak, P., Van Gorsel, E., 2010. Direct advection measurements do not help to solve the night-time CO2 closure problem: Evidence from three different forests. Agricultural and Forest Meteorology, Special Issue on Advection: ADVEX and Other Direct Advection Measurement Campaigns 150, 655–664. https://doi.org/10.1016/j.agrformet.2010.01.016

Auble, D.L., Meyers, T.P., 1992. An open path, fast response infrared absorption gas analyzer for H2O and CO2. Boundary-Layer Meteorol 59, 243–256. https://doi.org/10.1007/BF00119815

Baldocchi, D., 2014. Measuring fluxes of trace gases and energy between ecosystems and the atmosphere – the state and future of the eddy covariance method. Global Change Biology 20, 3600–3609. https://doi.org/10.1111/gcb.12649

Baldocchi, D., Dralle, D., Jiang, C., Ryu, Y., 2019. How Much Water Is Evaporated Across California? A Multiyear Assessment Using a Biophysical Model Forced With Satellite Remote Sensing Data. Water Resources Research 55, 2722–2741. https://doi.org/10.1029/2018WR023884

Baldocchi, D., Falge, E., Gu, L., Olson, R., Hollinger, D., Running, S., Anthoni, P., Bernhofer, C., Davis, K., Evans, R., Fuentes, J., Goldstein, A., Katul, G., Law, B., Lee, X., Malhi, Y., Meyers, T., Munger, W., Oechel, W., U, K.T.P., Pilegaard, K., Schmid, H.P., Valentini, R., Verma, S., Vesala, T., Wilson, K., Wofsy, S., 2001. FLUXNET: A New Tool to Study the Temporal and Spatial Variability of Ecosystem-Scale Carbon Dioxide, Water Vapor, and Energy Flux Densities. Bulletin of the American Meteorological Society 82, 2415–2434. https://doi.org/10.1175/1520-0477(2001)082<2415:FANTTS>2.3.CO;2

Baldocchi, D., Finnigan, J., Wilson, K., Paw U, K.T., Falge, E., 2000. On Measuring Net Ecosystem Carbon Exchange Over Tall Vegetation on Complex Terrain. Boundary-Layer Meteorology 96, 257–291. https://doi.org/10.1023/A:1002497616547

Baldocchi, D., Knox, S., Dronova, I., Verfaillie, J., Oikawa, P., Sturtevant, C., Matthes, J.H., Detto, M., 2016. The impact of expanding flooded land area on the annual evaporation of rice. Agricultural and Forest Meteorology 223, 181–193.

Baldocchi, D.D., 2020. How eddy covariance flux measurements have contributed to our understanding of Global Change Biology. Global Change Biology 26, 242–260. https://doi.org/10.1111/gcb.14807

Baldocchi, D.D., Hincks, B.B., Meyers, T.P., 1988. Measuring Biosphere-Atmosphere Exchanges of Biologically Related Gases with Micrometeorological Methods. Ecology 69, 1331–1340. https://doi.org/10.2307/1941631

Baldocchi, D.D., Keeney, N., Rey-Sanchez, C., Fisher, J.B., 2022. Atmospheric humidity deficits tell us how soil moisture deficits down-regulate ecosystem evaporation. Advances in Water Resources 159, 104100. https://doi.org/10.1016/j.advwatres.2021.104100

Baldocchi, D.D., Meyers, T.P., 1988. A spectral and lag-correlation analysis of turbulence in a deciduous forest canopy. Boundary-Layer Meteorol 45, 31–58. https://doi.org/10.1007/BF00120814

Baldocchi, D.D., Rao, K.S., 1995. Intra-field variability of scalar flux densities across a transition between a desert and an irrigated potato field. Boundary-Layer Meteorol 76, 109–136. https://doi.org/10.1007/BF00710893

Baldocchi, D.D., Verma, S.B., Rosenberg, N.J., 1981a. Environmental effects on the CO2 flux and CO2—Water flux ratio of Alfalfa. Agricultural Meteorology 24, 175–184. https://doi.org/10.1016/0002-1571(81)90042-X

Baldocchi, D.D., Verma, S.B., Rosenberg, N.J., 1981b. Environmental effects on the CO2 flux and CO2—Water flux ratio of Alfalfa. Agricultural Meteorology 24, 175–184. https://doi.org/10.1016/0002-1571(81)90042-X

Baldocchi, D.D., Verma, S.B., Rosenberg, N.J., 1981c. Seasonal and diurnal variation in the co2 flux and co2—water flux ratio of alfalfa. Agricultural Meteorology 23, 231–244. https://doi.org/10.1016/0002-1571(81)90107-2

Blad, B., Rosenberg, N., 1974. Lysimetric Calibration of the Bowen Ratio-Energy Balance Method for Evapotranspiration Estimation in the Central Great Plains. Agronomy & Horticulture -- Faculty Publications.

Brakke, T.W., Verma, S.B., Rosenberg, N.J., 1978. Local and Regional Components of Sensible Heat Advection. Journal of Applied Meteorology and Climatology 17, 955–963. https://doi.org/10.1175/1520-0450(1978)017<0955:LARCOS>2.0.CO;2

Brunet, Y., Itier, B., McAneney, J., Lagouarde, J.P., 1994. Downwind evolution of scalar fluxes and surface resistance under conditions of local advection. Part II: measurements over

barley. Agricultural and Forest Meteorology 71, 227–245. https://doi.org/10.1016/0168-1923(94)90013-2

Brunsell, N.A., Mechem, D.B., Anderson, M.C., 2011. Surface heterogeneity impacts on boundary layer dynamics via energy balance partitioning. Atmospheric Chemistry and Physics 11, 3403–3416. https://doi.org/10.5194/acp-11-3403-2011

Buchan, G.D., 2000. Soil Temperature Regime, in: Soil and Environmental Analysis. CRC Press.

Burba, G., Anderson, D., 2010. A Brief Practical Guide to Eddy Covariance Flux Measurements: Principles and Workflow Examples for Scientific and Industrial Applications. LI-COR Biosciences.

Butterworth, B.J., Desai, A.R., Townsend, P.A., Petty, G.W., Andresen, C.G., Bertram, T.H., Kruger, E.L., Mineau, J.K., Olson, E.R., Paleri, S., Pertzborn, R.A., Pettersen, C., Stoy, P.C., Thom, J.E., Vermeuel, M.P., Wagner, T.J., Wright, D.B., Zheng, T., Metzger, S., Schwartz, M.D., Iglinski, T.J., Mauder, M., Speidel, J., Vogelmann, H., Wanner, L., Augustine, T.J., Brown, W.O.J., Oncley, S.P., Buban, M., Lee, T.R., Cleary, P., Durden, D.J., Florian, C.R., Lantz, K., Riihimaki, L.D., Sedlar, J., Meyers, T.P., Plummer, D.M., Guzman, E.R., Smith, E.N., Sühring, M., Turner, D.D., Wang, Z., White, L.D., Wilczak, J.M., 2021. Connecting Land–Atmosphere Interactions to Surface Heterogeneity in CHEESEHEAD19. Bulletin of the American Meteorological Society 102, E421–E445. https://doi.org/10.1175/BAMS-D-19-0346.1

Campioli, M., Malhi, Y., Vicca, S., Luyssaert, S., Papale, D., Peñuelas, J., Reichstein, M., Migliavacca, M., Arain, M.A., Janssens, I.A., 2016. Evaluating the convergence between eddy-covariance and biometric methods for assessing carbon budgets of forests. Nat Commun 7, 13717. https://doi.org/10.1038/ncomms13717

Carlson, G., Shirzaei, M., Ojha, C., Werth, S., 2020. Subsidence-Derived Volumetric Strain Models for Mapping Extensional Fissures and Constraining Rock Mechanical Properties in the San Joaquin Valley, California. Journal of Geophysical Research: Solid Earth 125, e2020JB019980. https://doi.org/10.1029/2020JB019980

Castellví, F., 2004. Combining surface renewal analysis and similarity theory: A new approach for estimating sensible heat flux. Water Resources Research 40. https://doi.org/10.1029/2003WR002677

Castellví, F., Snyder, R.L., Baldocchi, D.D., Martínez-Cob, A., 2006. A comparison of new and existing equations for estimating sensible heat flux using surface renewal and similarity concepts. Water Resources Research 42. https://doi.org/10.1029/2005WR004642

CDFA, (California Department of Food and Agriculture), 2019. California Agricultural Statistics Review 2018-2019.

Chu, H., Luo, X., Ouyang, Z., Chan, W.S., Dengel, S., Biraud, S.C., Torn, M.S., Metzger, S., Kumar, J., Arain, M.A., Arkebauer, T.J., Baldocchi, D., Bernacchi, C., Billesbach, D., Black, T.A., Blanken, P.D., Bohrer, G., Bracho, R., Brown, S., Brunsell, N.A., Chen, J., Chen, X., Clark, K., Desai, A.R., Duman, T., Durden, D., Fares, S., Forbrich, I., Gamon, J.A., Gough, C.M., Griffis, T., Helbig, M., Hollinger, D., Humphreys, E., Ikawa, H., Iwata, H., Ju, Y., Knowles, J.F., Knox, S.H., Kobayashi, H., Kolb, T., Law, B., Lee, X., Litvak, M., Liu, H., Munger, J.W., Noormets, A., Novick, K., Oberbauer, S.F., Oechel, W., Oikawa, P., Papuga, S.A., Pendall, E., Prajapati, P., Prueger, J., Quinton, W.L., Richardson, A.D., Russell, E.S., Scott, R.L., Starr, G., Staebler, R., Stoy, P.C., Stuart-Haëntjens, E., Sonnentag, O., Sullivan, R.C., Suyker, A., Ueyama, M., Vargas, R., Wood, J.D., Zona, D., 2021. Representativeness of Eddy-Covariance flux footprints for areas

surrounding AmeriFlux sites. Agricultural and Forest Meteorology 301–302, 108350. https://doi.org/10.1016/j.agrformet.2021.108350

Cloern, J.E., Jassby, A.D., 2012. Drivers of change in estuarine-coastal ecosystems: Discoveries from four decades of study in San Francisco Bay. Reviews of Geophysics 50. https://doi.org/10.1029/2012RG000397

Cowan, I.R., Farquhar, G.D., 1977. Stomatal function in relation to leaf metabolism and environment. Symp Soc Exp Biol 31, 471–505.

Cui, W., Chui, T.F.M., 2019. Temporal and spatial variations of energy balance closure across FLUXNET research sites. Agricultural and Forest Meteorology 271, 12–21. https://doi.org/10.1016/j.agrformet.2019.02.026

Da Ros Carvalho, H., McInnes, K.J., Heilman, J.L., 2021. Construction of a Simple Domeless Net Radiometer for Demonstrating Energy Balance Concepts in a Laboratory Activity. Atmosphere 12, 1620. https://doi.org/10.3390/atmos12121620

DeFlorio, M.J., Sengupta, A., Castellano, C.M., Wang, J., Zhang, Z., Gershunov, A., Guirguis, K., Niño, R.L., Clemesha, R.E.S., Pan, M., Xiao, M., Kawzenuk, B., Gibson, P.B., Scheftic, W., Broxton, P.D., Switanek, M.B., Yuan, J., Dettinger, M.D., Hecht, C.W., Cayan, D.R., Cornuelle, B.D., Miller, A.J., Kalansky, J., Monache, L.D., Ralph, F.M., Waliser, D.E., Robertson, A.W., Zeng, X., DeWitt, D.G., Jones, J., Anderson, M.L., 2024. From California's Extreme Drought to Major Flooding: Evaluating and Synthesizing Experimental Seasonal and Subseasonal Forecasts of Landfalling Atmospheric Rivers and Extreme Precipitation during Winter 2022/23. Bulletin of the American Meteorological Society 105, E84–E104. https://doi.org/10.1175/BAMS-D-22-0208.1

Detto, M., Baldocchi, D., Katul, G.G., 2010. Scaling Properties of Biologically Active Scalar Concentration Fluctuations in the Atmospheric Surface Layer over a Managed Peatland. Boundary-Layer Meteorol 136, 407–430. https://doi.org/10.1007/s10546-010-9514-z

Eder, F., De Roo, F., Rotenberg, E., Yakir, D., Schmid, H.P., Mauder, M., 2015. Secondary circulations at a solitary forest surrounded by semi-arid shrubland and their impact on eddy-covariance measurements. Agricultural and Forest Meteorology 211–212, 115–127. https://doi.org/10.1016/j.agrformet.2015.06.001

Eichelmann, E., Hemes, K.S., Knox, S.H., Oikawa, P.Y., Chamberlain, S.D., Sturtevant, C., Verfaillie, J., Baldocchi, D.D., 2018. The effect of land cover type and structure on evapotranspiration from agricultural and wetland sites in the Sacramento–San Joaquin River Delta, California. Agricultural and Forest Meteorology 256–257, 179–195. https://doi.org/10.1016/j.agrformet.2018.03.007

Emad, A., 2023. Optimal Frequency-Response Corrections for Eddy Covariance Flux Measurements Using the Wiener Deconvolution Method. Boundary-Layer Meteorol 188, 29–53. https://doi.org/10.1007/s10546-023-00799-w

Famiglietti, J.S., 2014. The global groundwater crisis. Nature Clim Change 4, 945–948. https://doi.org/10.1038/nclimate2425

Farquhar, G.D., von Caemmerer, S., Berry, J.A., 1980. A biochemical model of photosynthetic CO_2 assimilation in leaves of C3 species. Planta 149, 78–90. https://doi.org/10.1007/BF00386231

Faunt, C.C., Sneed, M., Traum, J., Brandt, J.T., 2016. Water availability and land subsidence in the Central Valley, California, USA. Hydrogeol J 24, 675–684. https://doi.org/10.1007/s10040-015-1339-x

Feigenwinter, C., Bernhofer, C., Eichelmann, U., Heinesch, B., Hertel, M., Janous, D., Kolle, O., Lagergren, F., Lindroth, A., Minerbi, S., Moderow, U., Mölder, M., Montagnani, L., Queck, R., Rebmann, C., Vestin, P., Yernaux, M., Zeri, M., Ziegler, W., Aubinet, M., 2008. Comparison of horizontal and vertical advective CO_2 fluxes at three forest sites. Agricultural and Forest Meteorology 148, 12–24. https://doi.org/10.1016/j.agrformet.2007.08.013

Finnigan, J., 1999. A comment on the paper by Lee (1998): "On micrometeorological observations of surface-air exchange over tall vegetation." Agricultural and Forest Meteorology 97, 55–64. https://doi.org/10.1016/S0168-1923(99)00049-0

Fisher, J.B., Keenan, T.F., Buechner, C., Shirkey, G., Perez-Quezada, J.F., Knox, S.H., Frank, J.M., Runkle, B.R.K., Bohrer, G., 2021. Once Upon a Time, in AmeriFlux. Journal of Geophysical Research: Biogeosciences 126, e2020JG006148. https://doi.org/10.1029/2020JG006148

Fisher, J.B., Lee, B., Purdy, A.J., Halverson, G.H., Dohlen, M.B., Cawse-Nicholson, K., Wang, A., Anderson, R.G., Aragon, B., Arain, M.A., Baldocchi, D.D., Baker, J.M., Barral, H., Bernacchi, C.J., Bernhofer, C., Biraud, S.C., Bohrer, G., Brunsell, N., Cappelaere, B., Castro-Contreras, S., Chun, J., Conrad, B.J., Cremonese, E., Demarty, J., Desai, A.R., De Ligne, A., Foltýnová, L., Goulden, M.L., Griffis, T.J., Grünwald, T., Johnson, M.S., Kang, M., Kelbe, D., Kowalska, N., Lim, J.-H., Maïnassara, I., McCabe, M.F., Missik, J.E.C., Mohanty, B.P., Moore, C.E., Morillas, L., Morrison, R., Munger, J.W., Posse, G., Richardson, A.D., Russell, E.S., Ryu, Y., Sanchez-Azofeifa, A., Schmidt, M., Schwartz, E., Sharp, I., Šigut, L., Tang, Y., Hulley, G., Anderson, M., Hain, C., French, A., Wood, E., Hook, S., 2020. ECOSTRESS: NASA's Next Generation Mission to Measure Evapotranspiration From the International Space Station. Water Resources Research 56, e2019WR026058. https://doi.org/10.1029/2019WR026058

Fisher, J.B., Melton, F., Middleton, E., Hain, C., Anderson, M., Allen, R., McCabe, M.F., Hook, S., Baldocchi, D., Townsend, P.A., Kilic, A., Tu, K., Miralles, D.D., Perret, J., Lagouarde, J.-P., Waliser, D., Purdy, A.J., French, A., Schimel, D., Famiglietti, J.S., Stephens, G., Wood, E.F., 2017. The future of evapotranspiration: Global requirements for ecosystem functioning, carbon and climate feedbacks, agricultural management, and water resources. Water Resources Research 53, 2618–2626. https://doi.org/10.1002/2016WR020175

Fisher, J.B., Tu, K.P., Baldocchi, D.D., 2008. Global estimates of the land–atmosphere water flux based on monthly AVHRR and ISLSCP-II data, validated at 16 FLUXNET sites. Remote Sensing of Environment 112, 901–919. https://doi.org/10.1016/j.rse.2007.06.025

Foken, T., Bange, J., 2021. Temperature Sensors, in: Foken, T. (Ed.), Springer Handbook of Atmospheric Measurements, Springer Handbooks. Springer International Publishing, Cham, pp. 183–208. https://doi.org/10.1007/978-3-030-52171-4_7

Foken, T., Leuning, R., Oncley, S.R., Mauder, M., Aubinet, M., 2012. Corrections and Data Quality Control, in: Aubinet, M., Vesala, T., Papale, D. (Eds.), Eddy Covariance: A Practical Guide to Measurement and Data Analysis, Springer Atmospheric Sciences. Springer Netherlands, Dordrecht, pp. 85–131. https://doi.org/10.1007/978-94-007-2351-1_4

Foken, Th., Wichura, B., 1996. Tools for quality assessment of surface-based flux measurements. Agricultural and Forest Meteorology 78, 83–105. https://doi.org/10.1016/0168-1923(95)02248-1

Fritschen, L.J., 1966. Evapotranspiration Rates of Field Crops Determined by the Bowen Ratio Method1. Agronomy Journal 58, 339–342. https://doi.org/10.2134/agronj1966.00021962005800030028x

Gao, Z., Liu, H., Russell, E.S., Huang, J., Foken, T., Oncley, S.P., 2016. Large eddies modulating flux convergence and divergence in a disturbed unstable atmospheric surface layer. Journal of Geophysical Research: Atmospheres 121, 1475–1492. https://doi.org/10.1002/2015JD024529

Gash, J.H.C., 1986. A note on estimating the effect of a limited fetch on micrometeorological evaporation measurements. Boundary-Layer Meteorol 35, 409–413. https://doi.org/10.1007/BF00118567

Gavilán, P., Berengena, J., 2006. Accuracy of the Bowen ratio-energy balance method for measuring latent heat flux in a semiarid advective environment. Irrigation Science. https://doi.org/10.1007/s00271-006-0040-1

Gentine, P., Entekhabi, D., Polcher, J., 2011. The Diurnal Behavior of Evaporative Fraction in the Soil–Vegetation–Atmospheric Boundary Layer Continuum. Journal of Hydrometeorology 12, 1530–1546. https://doi.org/10.1175/2011JHM1261.1

Gilmanov, T.G., Baker, J.M., Bernacchi, C.J., Billesbach, D.P., Burba, G.G., Castro, S., Chen, J., Eugster, W., Fischer, M.L., Gamon, J.A., Gebremedhin, M.T., Glenn, A.J., Griffis, T.J., Hatfield, J.L., Heuer, M.W., Howard, D.M., Leclerc, M.Y., Loescher, H.W., Marloie, O., Meyers, T.P., Olioso, A., Phillips, R.L., Prueger, J.H., Skinner, R.H., Suyker, A.E., Tenuta, M., Wylie, B.K., 2014. Productivity and Carbon Dioxide Exchange of Leguminous Crops: Estimates from Flux Tower Measurements. Agronomy Journal 106, 545–559. https://doi.org/10.2134/agronj2013.0270

Gu, L., Meyers, T., Pallardy, S.G., Hanson, P.J., Yang, B., Heuer, M., Hosman, K.P., Liu, Q., Riggs, J.S., Sluss, D., Wullschleger, S.D., 2007. Correction to "Influences of biomass heat and biochemical energy storages on the land surface fluxes and radiative temperature." Journal of Geophysical Research: Atmospheres 112. https://doi.org/10.1029/2007JD008509

Hanemann, M., 2014. Property rights and sustainable irrigation—A developed world perspective. Agricultural Water Management, Exploring some of the socio-economic realities of sustainable water management in irrigation 145, 5–22. https://doi.org/10.1016/j.agwat.2014.07.001

Harder, P., Pomeroy, J.W., Helgason, W., 2017. Local-Scale Advection of Sensible and Latent Heat During Snowmelt. Geophysical Research Letters 44, 9769–9777. https://doi.org/10.1002/2017GL074394

Higgins, C.W., Pardyjak, E., Froidevaux, M., Simeonov, V., Parlange, M.B., 2013. Measured and Estimated Water Vapor Advection in the Atmospheric Surface Layer. Journal of Hydrometeorology 14, 1966–1972. https://doi.org/10.1175/JHM-D-12-0166.1

Hill, T., Chocholek, M., Clement, R., 2017. The case for increasing the statistical power of eddy covariance ecosystem studies: why, where and how? Global Change Biology 23, 2154–2165. https://doi.org/10.1111/gcb.13547

Hu, Y., Kang, S., Ding, R., Du, T., Tong, L., Li, S., 2020. The Dynamic Yield Response Factor of Alfalfa Improves the Accuracy of Dual Crop Coefficient Approach under Water and Salt Stress. Water 12, 1224. https://doi.org/10.3390/w12051224

Hulley, G., Hook, S., Fisher, J., Lee, C., 2017. ECOSTRESS, A NASA Earth-Ventures Instrument for studying links between the water cycle and plant health over the diurnal

cycle, in: 2017 IEEE International Geoscience and Remote Sensing Symposium (IGARSS). Presented at the 2017 IEEE International Geoscience and Remote Sensing Symposium (IGARSS), pp. 5494–5496. https://doi.org/10.1109/IGARSS.2017.8128248

Itier, B., Brunet, Y., McAneney, K.J., Lagouarde, J.P., 1994. Downwind evolution of scalar fluxes and surface resistance under conditions of local advection. Part I: a reappraisal of boundary conditions. Agricultural and Forest Meteorology 71, 211–225. https://doi.org/10.1016/0168-1923(94)90012-4

Jarvis, P.G., McNaughton, K.G., 1986. Stomatal Control of Transpiration: Scaling Up from Leaf to Region, in: MacFadyen, A., Ford, E.D. (Eds.), Advances in Ecological Research. Academic Press, pp. 1–49. https://doi.org/10.1016/S0065-2504(08)60119-1

Johnson, K.A., Johnson, D.E., 1995. Methane emissions from cattle. Journal of Animal Science 73, 2483–2492. https://doi.org/10.2527/1995.7382483x

Kaimal, J.C., Businger, J.A., 1963. A Continuous Wave Sonic Anemometer-Thermometer. Journal of Applied Meteorology and Climatology 2, 156–164. https://doi.org/10.1175/1520-0450(1963)002<0156:ACWSAT>2.0.CO;2

Kaimal, J.C., Finnigan, J.J., 1994. Atmospheric Boundary Layer Flows: Their Structure and Measurement. Oxford University Press.

Kaimal, J.C., Wyngaard, J.C., Izumi, Y., Coté, O.R., 1972. Spectral characteristics of surface-layer turbulence. Quarterly Journal of the Royal Meteorological Society 98, 563–589. https://doi.org/10.1002/qj.49709841707

Katul, G., Goltz, S.M., Hsieh, C.-I., Cheng, Y., Mowry, F., Sigmon, J., 1995. Estimation of surface heat and momentum fluxes using the flux-variance method above uniform and non-uniform terrain. Boundary-Layer Meteorol 74, 237–260. https://doi.org/10.1007/BF00712120

Kenny, W.T., Bohrer, G., Morin, T.H., Vogel, C.S., Matheny, A.M., Desai, A.R., 2017. A Numerical Case Study of the Implications of Secondary Circulations to the Interpretation of Eddy-Covariance Measurements Over Small Lakes. Boundary-Layer Meteorol 165, 311–332. https://doi.org/10.1007/s10546-017-0268-8

Kochendorfer, J., Paw U, K.T., 2011. Field estimates of scalar advection across a canopy edge. Agricultural and Forest Meteorology 151, 585–594. https://doi.org/10.1016/j.agrformet.2011.01.003

Kustas, W.P., Blanford, J.H., Stannard, D.I., Daughtry, C.S.T., Nichols, W.D., Weltz, M.A., 1994. Local energy flux estimates for unstable conditions using variance data in semiarid rangelands. Water Resources Research. https://doi.org/10.1029/93WR03084

Lang, A.R.G., 1973. Measurement of evapotranspiration in the presence of advection, by means of a modified energy balance procedure. Agricultural Meteorology 12, 75–81. https://doi.org/10.1016/0002-1571(73)90008-3

Lang, A.R.G., Evans, G.N., Ho, P.Y., 1974. The influence of local advection on evapotranspiration from irrigated rice in a semi-arid region. Agricultural Meteorology 13, 5–13. https://doi.org/10.1016/0002-1571(74)90060-0

Lang, A.R.G., McNaughton, K.G., Fazu, C., Bradley, E.F., Ohtaki, E., 1983. Inequality of eddy transfer coefficients for vertical transport of sensible and latent heats during advective inversions. Boundary-Layer Meteorol 25, 25–41. https://doi.org/10.1007/BF00122095

Leuning, R., van Gorsel, E., Massman, W.J., Isaac, P.R., 2012. Reflections on the surface energy imbalance problem. Agricultural and Forest Meteorology 156, 65–74. https://doi.org/10.1016/j.agrformet.2011.12.002

Lhomme, J.-P., Elguero, E., 1999. Examination of evaporative fraction diurnal behaviour using a soil-vegetation model coupled with a mixed-layer model. Hydrology and Earth System Sciences 3, 259–270. https://doi.org/10.5194/hess-3-259-1999

Li, D., Bou-Zeid, E., 2011. Coherent Structures and the Dissimilarity of Turbulent Transport of Momentum and Scalars in the Unstable Atmospheric Surface Layer. Boundary-Layer Meteorol 140, 243–262. https://doi.org/10.1007/s10546-011-9613-5

Lindberg, S.E., Dong, W., Meyers, T., 2002. Transpiration of gaseous elemental mercury through vegetation in a subtropical wetland in Florida. Atmospheric Environment 36, 5207–5219. https://doi.org/10.1016/S1352-2310(02)00586-1

Liu, P.-W., Famiglietti, J.S., Purdy, A.J., Adams, K.H., McEvoy, A.L., Reager, J.T., Bindlish, R., Wiese, D.N., David, C.H., Rodell, M., 2022. Groundwater depletion in California's Central Valley accelerates during megadrought. Nat Commun 13, 7825. https://doi.org/10.1038/s41467-022-35582-x

Lorenzo, C.D., García-Gagliardi, P., Antonietti, M.S., Sánchez-Lamas, M., Mancini, E., Dezar, C.A., Vazquez, M., Watson, G., Yanovsky, M.J., Cerdán, P.D., 2020. Improvement of alfalfa forage quality and management through the down-regulation of MsFTa1. Plant Biotechnology Journal 18, 944–954. https://doi.org/10.1111/pbi.13258

Lund, J., Medellin-Azuara, J., Durand, J., Stone, K., 2018. Lessons from California's 2012–2016 Drought. Journal of Water Resources Planning and Management 144, 04018067. https://doi.org/10.1061/(ASCE)WR.1943-5452.0000984

Mallick, K., Jarvis, A., Wohlfahrt, G., Kiely, G., Hirano, T., Miyata, A., Yamamoto, S., Hoffmann, L., 2015. Components of near-surface energy balance derived from satellite soundings – Part 1: Noontime net available energy. Biogeosciences 12, 433–451. https://doi.org/10.5194/bg-12-433-2015

Massman, W.J., 2000. A simple method for estimating frequency response corrections for eddy covariance systems. Agricultural and Forest Meteorology. 104: 185-198. 104, 185–198.

Mauder, M., Foken, T., 2011. Documentation and Instruction Manual of the Eddy Covariance Software Package TK2. Arbeitsergebnisse, Universität Bayreuth, Abteilung Mikrometeorologie, ISSN 1614-8916 46. https://doi.org/10.5194/bg-5-451-2008

McAneney, K.J., Brunet, Y., Itier, B., 1994. Downwind evolution of transpiration by two irrigated crops under conditions of local advection. Journal of Hydrology 161, 375–388. https://doi.org/10.1016/0022-1694(94)90136-8

McElrone, A.J., Shapland, T.M., Calderon, A., Fitzmaurice, L., Paw U, K.T., Snyder, R.L., 2013. Surface Renewal: An Advanced Micrometeorological Method for Measuring and Processing Field-Scale Energy Flux Density Data. J Vis Exp. https://doi.org/10.3791/50666

McNaughton, K.G., 1976a. Evaporation and advection I: evaporation from extensive homogeneous surfaces. Quarterly Journal of the Royal Meteorological Society 102, 181–191. https://doi.org/10.1002/qj.49710243115

McNaughton, K.G., 1976b. Evaporation and advection II: evaporation downwind of a boundary separating regions having different surface resistances and available energies. Quarterly Journal of the Royal Meteorological Society 102, 193–202. https://doi.org/10.1002/qj.49710243116

McNaughton, K.G., Black, T.A., 1973. A study of evapotranspiration from a Douglas fir forest using the energy balance approach. Water Resources Research 9, 1579–1590. https://doi.org/10.1029/WR009i006p01579

McNaughton, K.G., Jarvis, P.G., 1991. Effects of spatial scale on stomatal control of transpiration. Agricultural and Forest Meteorology 54, 279–302. https://doi.org/10.1016/0168-1923(91)90010-N

McNaughton, K.G., Spriggs, T.W., 1986. A mixed-layer model for regional evaporation. Boundary-Layer Meteorol 34, 243–262. https://doi.org/10.1007/BF00122381

Medlyn, B.E., Duursma, R.A., Eamus, D., Ellsworth, D.S., Prentice, I.C., Barton, C.V.M., Crous, K.Y., De Angelis, P., Freeman, M., Wingate, L., 2011. Reconciling the optimal and empirical approaches to modelling stomatal conductance. Global Change Biology 17, 2134–2144. https://doi.org/10.1111/j.1365-2486.2010.02375.x

Melton, F.S., Huntington, J., Grimm, R., Herring, J., Hall, M., Rollison, D., Erickson, T., Allen, R., Anderson, M., Fisher, J.B., Kilic, A., Senay, G.B., Volk, J., Hain, C., Johnson, L., Ruhoff, A., Blankenau, P., Bromley, M., Carrara, W., Daudert, B., Doherty, C., Dunkerly, C., Friedrichs, M., Guzman, A., Halverson, G., Hansen, J., Harding, J., Kang, Y., Ketchum, D., Minor, B., Morton, C., Ortega-Salazar, S., Ott, T., Ozdogan, M., ReVelle, P.M., Schull, M., Wang, C., Yang, Y., Anderson, R.G., 2021. OpenET: Filling a Critical Data Gap in Water Management for the Western United States. JAWRA Journal of the American Water Resources Association n/a, 1–24. https://doi.org/10.1111/1752-1688.12956

Menefee, D., Scott, R.L., Abraha, M., Alfieri, J.G., Baker, J., Browning, D.M., Chen, J., Gonet, J., Johnson, J.M.F., Miller, G.R., Nifong, R., Robertson, P., Russell, E.S., Saliendra, N., Schreiner-Mcgraw, A.P., Suyker, A., Wagle, P., Wente, C., White, P.M., Smith, D., 2022. Unraveling the effects of management and climate on carbon fluxes of U.S. croplands using the USDA Long-Term Agroecosystem (LTAR) network. Agricultural and Forest Meteorology 326, 109154. https://doi.org/10.1016/j.agrformet.2022.109154

Meyers, T.P., Hall, M.E., Lindberg, S.E., Kim, K., 1996. Use of the modified bowen-ratio technique to measure fluxes of trace gases. Atmospheric Environment 30, 3321–3329. https://doi.org/10.1016/1352-2310(96)00082-9

Meyers, T.P., Hollinger, S.E., 2004. An assessment of storage terms in the surface energy balance of maize and soybean. Agricultural and Forest Meteorology 125, 105–115. https://doi.org/10.1016/j.agrformet.2004.03.001

Moderow, U., Grünwald, T., Queck, R., Spank, U., Bernhofer, C., 2021. Energy balance closure and advective fluxes at ADVEX sites. Theor Appl Climatol 143, 761–779. https://doi.org/10.1007/s00704-020-03412-z

Moffat, A.M., Papale, D., Reichstein, M., Hollinger, D.Y., Richardson, A.D., Barr, A.G., Beckstein, C., Braswell, B.H., Churkina, G., Desai, A.R., Falge, E., Gove, J.H., Heimann, M., Hui, D., Jarvis, A.J., Kattge, J., Noormets, A., Stauch, V.J., 2007. Comprehensive comparison of gap-filling techniques for eddy covariance net carbon fluxes. Agricultural and Forest Meteorology 147, 209–232. https://doi.org/10.1016/j.agrformet.2007.08.011

Moore, C.J., 1986. Frequency response corrections for eddy correlation systems. Boundary-Layer Meteorol 37, 17–35. https://doi.org/10.1007/BF00122754

Morrison, T., Calaf, M., Higgins, C.W., Drake, S.A., Perelet, A., Pardyjak, E., 2021. The Impact of Surface Temperature Heterogeneity on Near-Surface Heat Transport. Boundary-Layer Meteorol 180, 247–272. https://doi.org/10.1007/s10546-021-00624-2

Novick, K., Brantley, S., Miniat, C.F., Walker, J., Vose, J.M., 2014. Inferring the contribution of advection to total ecosystem scalar fluxes over a tall forest in complex terrain.

Agricultural and Forest Meteorology 185, 1–13.
https://doi.org/10.1016/j.agrformet.2013.10.010

Novick, K.A., Ficklin, D.L., Stoy, P.C., Williams, C.A., Bohrer, G., Oishi, A.C., Papuga, S.A., Blanken, P.D., Noormets, A., Sulman, B.N., Scott, R.L., Wang, L., Phillips, R.P., 2016. The increasing importance of atmospheric demand for ecosystem water and carbon fluxes. Nature Clim Change 6, 1023–1027. https://doi.org/10.1038/nclimate3114

Odum, E.P., 1969. The Strategy of Ecosystem Development. Science 164, 262–270. https://doi.org/10.1126/science.164.3877.262

Oncley, S.P., Foken, T., Vogt, R., Kohsiek, W., DeBruin, H.A.R., Bernhofer, C., Christen, A., Gorsel, E. van, Grantz, D., Feigenwinter, C., Lehner, I., Liebethal, C., Liu, H., Mauder, M., Pitacco, A., Ribeiro, L., Weidinger, T., 2007. The Energy Balance Experiment EBEX-2000. Part I: overview and energy balance. Boundary-Layer Meteorol 123, 1–28. https://doi.org/10.1007/s10546-007-9161-1

Parry, C.K., Shapland, T.M., Williams, L.E., Calderon-Orellana, A., Snyder, R.L., Paw U, K.T., McElrone, A.J., 2019. Comparison of a stand-alone surface renewal method to weighing lysimetry and eddy covariance for determining vineyard evapotranspiration and vine water stress. Irrig Sci 37, 737–749. https://doi.org/10.1007/s00271-019-00626-6

Pathak, T.B., Maskey, M.L., Dahlberg, J.A., Kearns, F., Bali, K.M., Zaccaria, D., 2018. Climate Change Trends and Impacts on California Agriculture: A Detailed Review. Agronomy 8, 25. https://doi.org/10.3390/agronomy8030025

Paw U, K.T., Baldocchi, D.D., Meyers, T.P., Wilson, K.B., 2000. Correction Of Eddy-Covariance Measurements Incorporating Both Advective Effects And Density Fluxes. Boundary-Layer Meteorology 97, 487–511. https://doi.org/10.1023/A:1002786702909

Pennypacker, S., Baldocchi, D., 2016. Seeing the Fields and Forests: Application of Surface-Layer Theory and Flux-Tower Data to Calculating Vegetation Canopy Height. Boundary-Layer Meteorol 158, 165–182. https://doi.org/10.1007/s10546-015-0090-0

Peñuelas, J., Filella, I., 2001. Responses to a Warming World. Science 294, 793–795. https://doi.org/10.1126/science.1066860

Philip, J., 1987. Advection, evaporation, and surface resistance. Irrigation Science 8, 101–114.

Philip, J.R., 1959. THE THEORY OF LOCAL ADVECTION: I. Journal of the Atmospheric Sciences 16, 535–547. https://doi.org/10.1175/1520-0469(1959)016<0535:TTOLAI>2.0.CO;2

Prueger, J.H., Hipps, L.E., Cooper, D.I., 1996. Evaporation and the development of the local boundary layer over an irrigated surface in an arid region. Agricultural and Forest Meteorology 78, 223–237. https://doi.org/10.1016/0168-1923(95)02234-1

Putnam, D., Brummer, J., Cash, D., Gray, A., Griggs, T., Ottman, M., Ray, I., Riggs, W., Smith, M., Shewmaker, G., Todd, R., 2000. The importance of western alfalfa production., in: The Importance of Western Alfalfa Production. Presented at the Proceedings of 29th National Alfalfa Symposium and 30th CA Alfalfa Symposium., Las Vegas, NV, USA, pp. 11–12.

Putnam, D.H., Summers, C.G., Orloff, S.B., 2007. Alfalfa Production Systems in California, in: IN (C. G. Summers and D. H. Putnam, Eds.), Irrigated Alfalfa Management for Mediterranean and Desert Zones. Chapter 1. Oakland: University of California Agriculture and Natural Resources Publication 8287.

Rao, K.S., Wyngaard, J.C., Coté, O.R., 1974. Local advection of momentum, heat, and moisture in micrometeorology. Boundary-Layer Meteorol 7, 331–348. https://doi.org/10.1007/BF00240836

Raupach, M.R., Thom, A.S., 1981. Turbulence in and above Plant Canopies. Annual Review of Fluid Mechanics 13, 97–129. https://doi.org/10.1146/annurev.fl.13.010181.000525

Reichstein, M., Falge, E., Baldocchi, D., Papale, D., Aubinet, M., Berbigier, P., Bernhofer, C., Buchmann, N., Gilmanov, T., Granier, A., Grünwald, T., Havránková, K., Ilvesniemi, H., Janous, D., Knohl, A., Laurila, T., Lohila, A., Loustau, D., Matteucci, G., Meyers, T., Miglietta, F., Ourcival, J.-M., Pumpanen, J., Rambal, S., Rotenberg, E., Sanz, M., Tenhunen, J., Seufert, G., Vaccari, F., Vesala, T., Yakir, D., Valentini, R., 2005. On the separation of net ecosystem exchange into assimilation and ecosystem respiration: review and improved algorithm. Global Change Biology 11, 1424–1439. https://doi.org/10.1111/j.1365-2486.2005.001002.x

Rey-Sánchez, A.C., Bohrer, G., Morin, T.H., Shlomo, D., Mirfenderesgi, G., Gildor, H., Genin, A., 2017. Evaporation and CO2 fluxes in a coastal reef: an eddy covariance approach. Ecosystem Health and Sustainability 3, 1392830. https://doi.org/10.1080/20964129.2017.1392830

Rey-Sanchez, C., Tianxin Wang, Szutu, D., Shortt, R., Chamberlaain, S., Verfaillie, J., Baldocchi, D., 2022. AmeriFlux BASE US-Bi1 Bouldin Island Alfalfa, Ver. 8-5.

Rosenberg, N.J., 1969a. Advective contribution of energy utilized in evapotranspiration by alfalfa in the east central great plains (U.S.A.). Agricultural Meteorology 6, 179–184. https://doi.org/10.1016/0002-1571(69)90003-X

Rosenberg, N.J., 1969b. Advective contribution of energy utilized in evapotranspiration by alfalfa in the east central great plains (U.S.A.). Agricultural Meteorology 6, 179–184. https://doi.org/10.1016/0002-1571(69)90003-X

Rosenberg, N.J., Verma, S.B., 1978. Extreme Evapotranspiration by Irrigated Alfalfa: A Consequence of the 1976 Midwestern Drought. Journal of Applied Meteorology and Climatology 17, 934–941. https://doi.org/10.1175/1520-0450(1978)017<0934:EEBIAA>2.0.CO;2

Ryu, Y., Berry, J.A., Baldocchi, D.D., 2019. What is global photosynthesis? History, uncertainties and opportunities. Remote Sensing of Environment 223, 95–114. https://doi.org/10.1016/j.rse.2019.01.016

Sauer, T.J., 2002. 5.5 Heat Flux Density, in: Methods of Soil Analysis. John Wiley & Sons, Ltd, pp. 1233–1248. https://doi.org/10.2136/sssabookser5.4.c52

Scanlon, B.R., Faunt, C.C., Longuevergne, L., Reedy, R.C., Alley, W.M., McGuire, V.L., McMahon, P.B., 2012. Groundwater depletion and sustainability of irrigation in the US High Plains and Central Valley. Proceedings of the National Academy of Sciences 109, 9320–9325. https://doi.org/10.1073/pnas.1200311109

Schotanus, P., Nieuwstadt, F.T.M., De Bruin, H.A.R., 1983. Temperature measurement with a sonic anemometer and its application to heat and moisture fluxes. Boundary-Layer Meteorol 26, 81–93. https://doi.org/10.1007/BF00164332

Shapland, T.M., McElrone, A.J., Snyder, R.L., Paw U, K.T., 2012a. Structure Function Analysis of Two-Scale Scalar Ramps. Part I: Theory and Modelling. Boundary-Layer Meteorol 145, 5–25. https://doi.org/10.1007/s10546-012-9742-5

Shapland, T.M., McElrone, A.J., Snyder, R.L., Paw U, K.T., 2012b. Structure Function Analysis of Two-Scale Scalar Ramps. Part II: Ramp Characteristics and Surface Renewal Flux

Estimation. Boundary-Layer Meteorol 145, 27–44. https://doi.org/10.1007/s10546-012-9740-7

Shapland, T.M., McElrone, A.J., U, K.T.P., Snyder, R.L., 2013. A Turnkey data logger program for field-scale energy flux density measurements using eddy covariance and surface renewal. Italian Journal of Agrometeorology 5–16.

Shapland, T.M., Snyder, R.L., Paw U, K.T., McElrone, A.J., 2014. Thermocouple frequency response compensation leads to convergence of the surface renewal alpha calibration. Agricultural and Forest Meteorology 189–190, 36–47. https://doi.org/10.1016/j.agrformet.2014.01.008

Snyder, R.L., Spano, D., Pawu, K.T., 1996. Surface renewal analysis for sensible and latent heat flux density. Boundary-Layer Meteorol 77, 249–266. https://doi.org/10.1007/BF00123527

Stewart, I.T., Rogers, J., Graham, A., 2020. Water security under severe drought and climate change: Disparate impacts of the recent severe drought on environmental flows and water supplies in Central California. Journal of Hydrology X 7, 100054. https://doi.org/10.1016/j.hydroa.2020.100054

Stewart, J.B., Kustas, W.P., Humes, K.S., Nichols, W.D., Moran, M.S., Bruin, H.A.R. de, 1994. Sensible Heat Flux-Radiometric Surface Temperature Relationship for Eight Semiarid Areas. Journal of Applied Meteorology and Climatology 33, 1110–1117. https://doi.org/10.1175/1520-0450(1994)033<1110:SHFRST>2.0.CO;2

Stoy, P.C., Mauder, M., Foken, T., Marcolla, B., Boegh, E., Ibrom, A., Arain, M.A., Arneth, A., Aurela, M., Bernhofer, C., Cescatti, A., Dellwik, E., Duce, P., Gianelle, D., van Gorsel, E., Kiely, G., Knohl, A., Margolis, H., McCaughey, H., Merbold, L., Montagnani, L., Papale, D., Reichstein, M., Saunders, M., Serrano-Ortiz, P., Sottocornola, M., Spano, D., Vaccari, F., Varlagin, A., 2013. A data-driven analysis of energy balance closure across FLUXNET research sites: The role of landscape scale heterogeneity. Agricultural and Forest Meteorology 171–172, 137–152. https://doi.org/10.1016/j.agrformet.2012.11.004

Stull, R.B., 1988. Measurement and Simulation Techniques, in: Stull, R.B. (Ed.), An Introduction to Boundary Layer Meteorology, Atmospheric Sciences Library. Springer Netherlands, Dordrecht, pp. 405–440. https://doi.org/10.1007/978-94-009-3027-8_10

Su, H.-B., Schmid, H.P., Grimmond, C.S.B., Vogel, C.S., Oliphant, A.J., 2004. Spectral Characteristics and Correction of Long-Term Eddy-Covariance Measurements Over Two Mixed Hardwood Forests in Non-Flat Terrain. Boundary-Layer Meteorology 110, 213–253. https://doi.org/10.1023/A:1026099523505

Suvočarev, K., Shapland, T.M., Snyder, R.L., Martínez-Cob, A., 2014. Surface renewal performance to independently estimate sensible and latent heat fluxes in heterogeneous crop surfaces. https://doi.org/10.1016/j.jhydrol.2013.11.025

Tanner, C.B., Sinclair, T.R., 1983. Efficient Water Use in Crop Production: Research or Re-Search?, in: Limitations to Efficient Water Use in Crop Production. John Wiley & Sons, Ltd, pp. 1–27. https://doi.org/10.2134/1983.limitationstoefficientwateruse.c1

Tillman, J.E., 1972. The Indirect Determination of Stability, Heat and Momentum Fluxes in the Atmospheric Boundary Layer from Simple Scalar Variables During Dry Unstable Conditions. Journal of Applied Meteorology and Climatology 11, 783–792. https://doi.org/10.1175/1520-0450(1972)011<0783:TIDOSH>2.0.CO;2

Tolk, J.A., Evett, S.R., Howell, T.A., 2006. Advection Influences on Evapotranspiration of Alfalfa in a Semiarid Climate. Agronomy Journal 98, 1646–1654. https://doi.org/10.2134/agronj2006.0031

Twine, T.E., Kustas, W.P., Norman, J.M., Cook, D.R., Houser, P.R., Meyers, T.P., Prueger, J.H., Starks, P.J., Wesely, M.L., 2000. Correcting eddy-covariance flux underestimates over a grassland. Agricultural and Forest Meteorology 103, 279–300. https://doi.org/10.1016/S0168-1923(00)00123-4

USDA/NASS, 2023. USDA/NASS 2023 State Agriculture Overview for California [WWW Document]. URL https://www.nass.usda.gov/Quick_Stats/Ag_Overview/stateOverview.php?state=california%20 (accessed 3.27.24).

Van Atta, C., 1977. Effect of coherent structures on structure functions of temperature in the atmospheric boundary layer. Aech Mech 29, 161–171.

Verma, S.B., Rosenberg, N.J., Blad, B.L., 1978. Turbulent Exchange Coefficients for Sensible Heat and Water Vapor under Advective Conditions. Journal of Applied Meteorology (1962-1982) 17, 330–338.

Vickers, D., Mahrt, L., 1997. Quality Control and Flux Sampling Problems for Tower and Aircraft Data. Journal of Atmospheric and Oceanic Technology 14, 512–526. https://doi.org/10.1175/1520-0426(1997)014<0512:QCAFSP>2.0.CO;2

Volk, J.M., Huntington, J., Melton, F.S., Allen, R., Anderson, M.C., Fisher, J.B., Kilic, A., Senay, G., Halverson, G., Knipper, K., Minor, B., Pearson, C., Wang, T., Yang, Y., Evett, S., French, A.N., Jasoni, R., Kustas, W., 2023. Development of a Benchmark Eddy Flux Evapotranspiration Dataset for Evaluation of Satellite-Driven Evapotranspiration Models Over the CONUS. Agricultural and Forest Meteorology 331, 109307. https://doi.org/10.1016/j.agrformet.2023.109307

Wagle, P., Gowda, P.H., Northup, B.K., 2019a. Annual dynamics of carbon dioxide fluxes over a rainfed alfalfa field in the U.S. Southern Great Plains. Agricultural and Forest Meteorology 265, 208–217. https://doi.org/10.1016/j.agrformet.2018.11.022

Wagle, P., Gowda, P.H., Northup, B.K., 2019b. Dynamics of evapotranspiration over a non-irrigated alfalfa field in the Southern Great Plains of the United States. Agricultural Water Management 223, 105727. https://doi.org/10.1016/j.agwat.2019.105727

Wang, Q., Hansen, J., Xu, F. (Eds.), 2016. China's emerging dairy markets and potential impacts on U.S. alfalfa and dairy product exports. https://doi.org/10.22004/ag.econ.235833

Wang, T., Alfieri, J., Mallick, K., Arias Ortiz, A., Anderson, M.C., Fisher, J.B., Girotto, M., Szutu, D., Verfaillie, J., Baldocchi, D., 2023a. How Advection Affects the Surface Energy Balance and Plays a Role in its Closure at an Irrigated Alfalfa Field. https://doi.org/10.2139/ssrn.4587556

Wang, T., Melton, F.S., Pôças, I., Johnson, L.F., Thao, T., Post, K., Cassel-Sharma, F., 2021. Evaluation of crop coefficient and evapotranspiration data for sugar beets from landsat surface reflectances using micrometeorological measurements and weighing lysimetry. Agricultural Water Management 244, 106533. https://doi.org/10.1016/j.agwat.2020.106533

Wang, T., Verfaillie, J., Szutu, D., Baldocchi, D., 2023b. Handily measuring sensible and latent heat exchanges at a bargain: A test of the variance-Bowen ratio approach. Agricultural and Forest Meteorology 333, 109399. https://doi.org/10.1016/j.agrformet.2023.109399

Warhaft, Z., 2000. Passive Scalars in Turbulent Flows. Annual Review of Fluid Mechanics 32, 203–240. https://doi.org/10.1146/annurev.fluid.32.1.203

Warhaft, Z., 1976. Heat and moisture flux in the stratified boundary layer. Quarterly Journal of the Royal Meteorological Society 102, 703–707. https://doi.org/10.1002/qj.49710243315

Weaver, H.L., 1990. Temperature and humidity flux-variance relations determined by one-dimensional eddy correlation. Boundary-Layer Meteorol 53, 77–91. https://doi.org/10.1007/BF00122464

Weaver, H.L., Campbell, G.S., 1985. USE OF PELTIER COOLERS AS SOIL HEAT FLUX TRANSDUCERS. Soil Science Society of America Journal.

Webb, E.K., Pearman, G.I., Leuning, R., 1980. Correction of flux measurements for density effects due to heat and water vapour transfer. Quarterly Journal of the Royal Meteorological Society 106, 85–100. https://doi.org/10.1002/qj.49710644707

Weltzin, J.F., Loik, M.E., Schwinning, S., Williams, D.G., Fay, P.A., Haddad, B.M., Harte, J., Huxman, T.E., Knapp, A.K., Lin, G., Pockman, W.T., Shaw, R.M., Small, E.E., Smith, M.D., Smith, S.D., Tissue, D.T., Zak, J.C., 2003. Assessing the Response of Terrestrial Ecosystems to Potential Changes in Precipitation. BioScience 53, 941–952. https://doi.org/10.1641/0006-3568(2003)053[0941:ATROTE]2.0.CO;2

Wesely, M.L., 1988. Use of variance techniques to measure dry air-surface exchange rates. Boundary-Layer Meteorol 44, 13–31. https://doi.org/10.1007/BF00117291

Wesely, M.L., Hicks, B.B., 1978. High-Frequency Temperature and Humidity Correlation Above a Warm Wet Surface. Journal of Applied Meteorology 17, 123–128. https://doi.org/10.1175/1520-0450(1978)017<0123:HFTAHC>2.0.CO;2

Wilczak, J.M., Oncley, S.P., Stage, S.A., 2001. Sonic Anemometer Tilt Correction Algorithms. Boundary-Layer Meteorology 99, 127–150. https://doi.org/10.1023/A:1018966204465

Wilson, K., Goldstein, A., Falge, E., Aubinet, M., Baldocchi, D., Berbigier, P., Bernhofer, C., Ceulemans, R., Dolman, H., Field, C., Grelle, A., Ibrom, A., Law, B.E., Kowalski, A., Meyers, T., Moncrieff, J., Monson, R., Oechel, W., Tenhunen, J., Valentini, R., Verma, S., 2002. Energy balance closure at FLUXNET sites. Agricultural and Forest Meteorology, FLUXNET 2000 Synthesis 113, 223–243. https://doi.org/10.1016/S0168-1923(02)00109-0

Wolf, A., Laca, E.A., 2007. Cospectral analysis of high frequency signal loss in eddy covariance measurements. Atmospheric Chemistry and Physics Discussions 7, 13151–13173. https://doi.org/10.5194/acpd-7-13151-2007

Zermeño-Gonzalez, A., Hipps, L.E., 1997. Downwind evolution of surface fluxes over a vegetated surface during local advection of heat and saturation deficit. Journal of Hydrology 192, 189–210. https://doi.org/10.1016/S0022-1694(96)03108-3

Zhang, Y., Liu, H., Foken, T., Williams, Q.L., Liu, S., Mauder, M., Liebethal, C., 2010. Turbulence Spectra and Cospectra Under the Influence of Large Eddies in the Energy Balance EXperiment (EBEX). Boundary-Layer Meteorol 136, 235–251. https://doi.org/10.1007/s10546-010-9504-1

Zhou, Y., Sühring, M., Li, X., 2023. Evaluation of energy balance closure adjustment and imbalance prediction methods in the convective boundary layer – A large eddy simulation study. Agricultural and Forest Meteorology 333, 109382. https://doi.org/10.1016/j.agrformet.2023.109382

Appendices

Appendix A: Variance-Bowen ratio algorithm

Matlab code used to calculate sensible heat flux and latent heat flux using the variance Bowen ratio approach. The annotations are displaying in dark grey italic texts for clarity.

1. Computing the statistics for air temperature
```
% Preconfigure the data size
nres = 8640; % the amount of 0.1 Hz data per day
nf = day_end - day_start + 1; % the number of files
pre_grouped = nf*nres; % total 0.1 Hz data
vial = 180; % half-hourly data: 0.1 (scan/s) * 60 (s) * 30 (min) = 180 (scans per 30 min)
ratio = pre_grouped/vial; % the amount of 30-min data blocks

% Reshaped temperature measurement into 30 min averaging blocks
% TA is the 0.1 Hz air temperature
TA_res = reshape(TA,vial,ratio);

% Compute the half-hourly standard deviation of TA
sigma_T = std(TA_res);
sigma_T = transpose(sigma_T);

% Mean air temperature for each half-hourly data
mean_T = nanmean(TA_res);
mean_T = transpose(mean_T);
```

2. Computing the statistics for relative humidity
```
% Compute the saturation vapor pressure using Clausius-Clapeyron equation
esat=611.2*exp(17.67.*(TA)./(TA+273.16-29.65)); % (Pascal)

r = 18.02 / 28.97; % mixing ratio: molar mass of water over air
P = 101324.6; % standard atmospheric pressure at steam point (Pascal)

% Actual vapor pressure (Pascal)
% RH is the 0.1 Hz air temperature
ea = (RH./100).*(esat);

% Saturation humidity (uniteless)
q_sat = (r.*esat)./P;

% Specific humidity (uniteless)
q= q_sat.*RH.*0.01;

% Reshape the ea and q into 30 min averaging blocks
q_res = reshape(q,vial,ratio);
```

ea_res = reshape(ea,vial,ratio);

% Compute the half-hourly standard deviation of specific humidity
sigma_q = std(q_res);
sigma_q = transpose(sigma_q);
% Compute the mean actual vapor pressure
mean_ea = mean(ea_res);
mean_ea = transpose(mean_ea);

3. Compute air density and specific heat of moist air
R = 8.3144; % universal gas constant (J mol-1 K-1)
Rd = 286.9; % dry air gas constant (J kg-1 K-1)
Rv = 461.5; % vapor gas constant (J kg-1 K-1)
Ma = 28.97/1000; % molar mass of dry air (kg mol-1)
Mv = 18/1000; % molar mass of water vapor (kg/mol)
Cpa = 1004.67; % specific heat of dry air (J Kg-1 K-1)

% Virtual temperature in Kelvin
Tv = (mean_T +273.15).*(1+0.38.*(mean_ea ./P));

% Air density (dry, vapor, and moist) in kg/m3
rhoD = (P-mean_ea)./(Rd.* (mean_T+273.15)); % dry air density
rhoV = mean_ea ./ (Rv.*(mean_T+273.15)); % vapor air density
rho = (P .* Ma)./(R.*Tv); % moist air density
% Moist air specific heat
qs = rhoV./ rho; % specific humidity
Cp = Cpa*(1+0.84*qs); % J kg-1 K-1

% Latent heat of vaporization (J/kg)
Lvap = (2.501-0.00237*mean_T)*1E6;

% Bowen ratio using the variance technique
B = (Cp./ Lvap).*(sigma_T./sigma_q);

% Use Bowen ratio to compute kinematic heat flux (wt) from sonic kinematic heat flux (wts)
wt_vb = wts./(1+((0.51.*Cp.*mean_T)./(Lvap.*B))); % Eq. 4

4. Compute sensible heat flux (H) using the variance-Bowen ratio (Eq. 5)
H_vb = Cp .* rho .* wt_vb;

5. Compute latent heat flux (LE) using the variance-Bowen ratio (Eq. 7)

% RNET is the net radiation
% G_corr is the heat storage corrected ground heat flux
LE_vb = (RNET-G_corr)./ (1 + B);
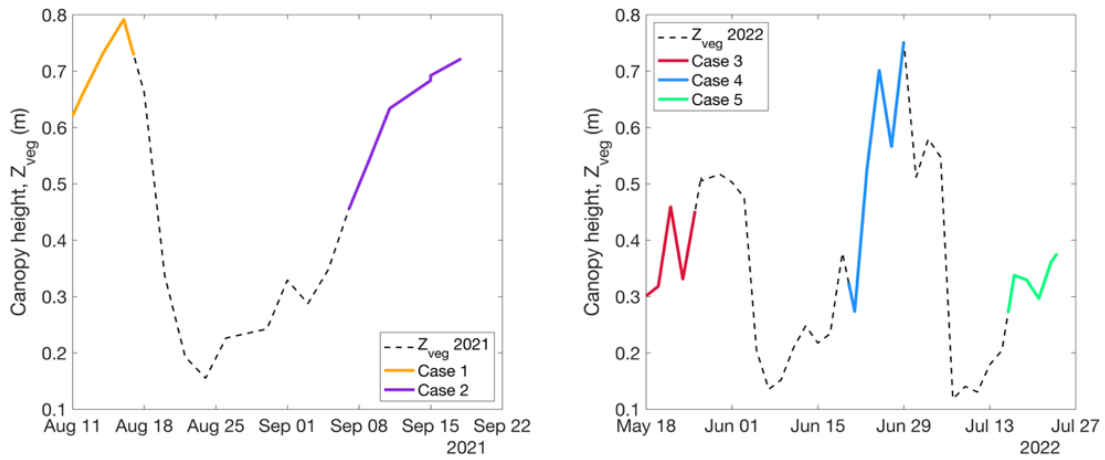
Appendix B: Aerodynamic canopy height

Figure B1. Aerodynamic canopy height throughout the analysis period.

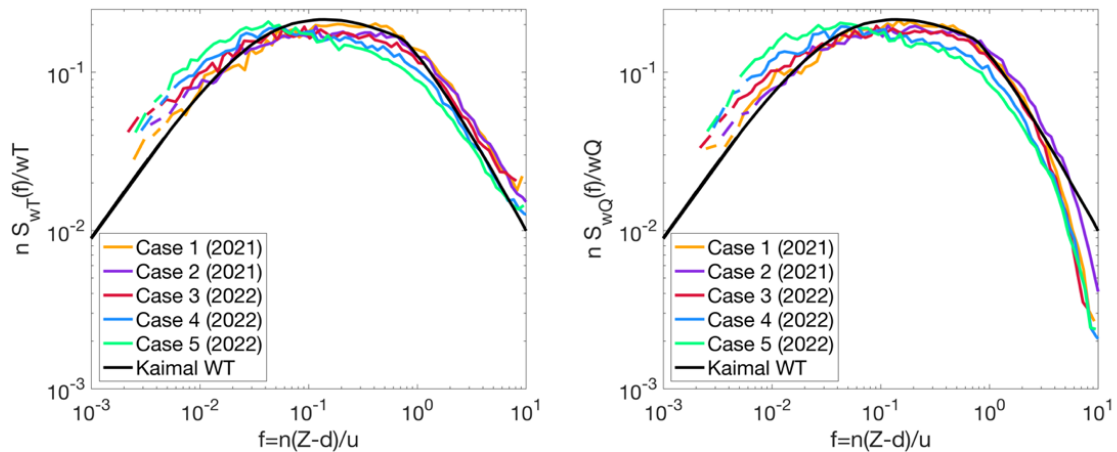Appendix C: Normalized cospectra of heat and water fluxes

Figure C1. Normalized co-spectra of vertical velocity, W, with temperature, T (left) and moisture, Q (right) at the main tower for Case 1 (orange), Case 2 (purple), Case 3 (red), Case 4 (blue), Case 5 (green), and idealized Kaimal cospectra of heat (black) in log-log scale prior to spectral correction. For each case, the half-hourly data are averaged over the case duration between 1000 to 1800 hours.
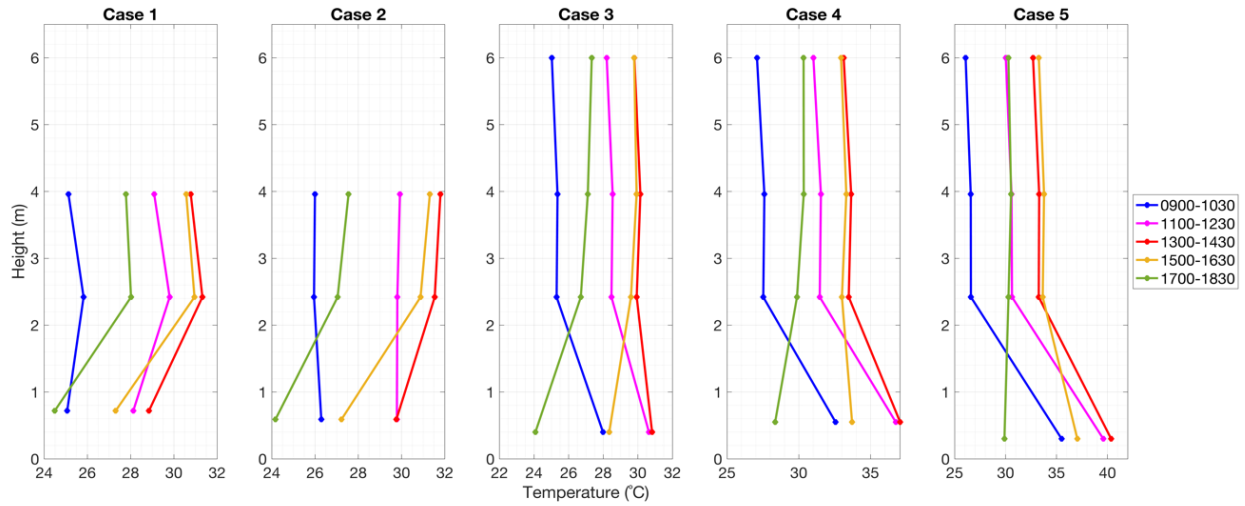
Appendix D: Temperature profile

Figure D1. Temperature profile in 2021(Case 1 & 2) and 2022 (Case 3, 4, & 5). The lowest height of the temperature represents aerodynamic temperature, derived with a gradient-resistance method. The height of the aerodynamic temperature is estimated through the mean aerodynamic vegetation height. All other heights, 2.42 m, 3.96 m, and/or 6.00 m, represent air temperature.

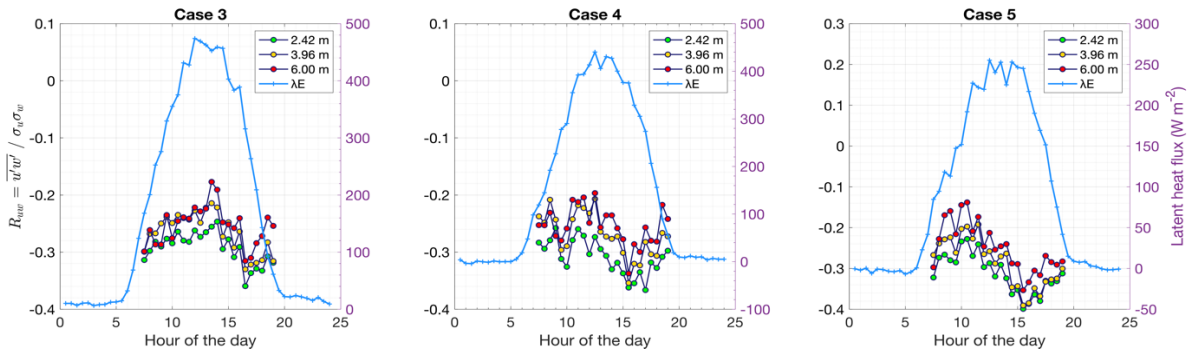Appendix E: Correlation coefficient of momentum fluxes

Figure E1. Correlation coefficient of momentum fluxes (R_{uw}) at 2.42 m, 3.96 m, and 6.00 m in 2022.
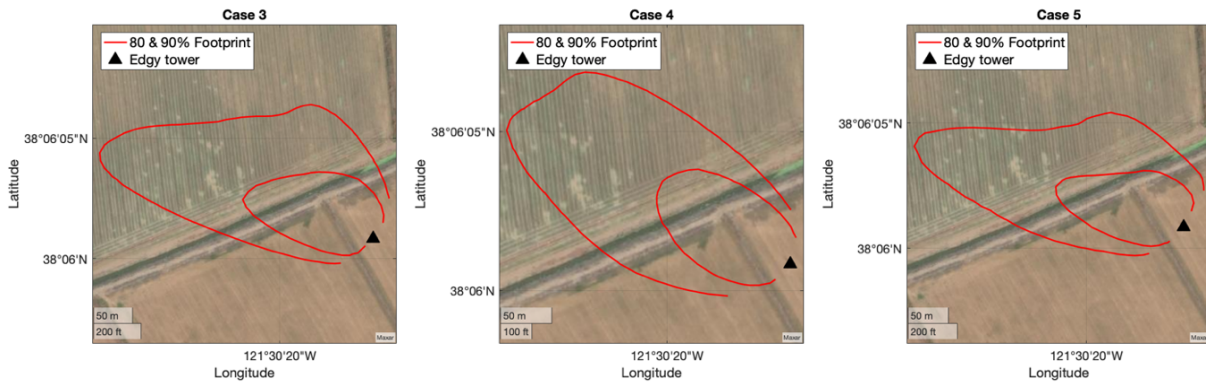
Appendix F: Footprint climatology at Edgy tower

Figure F1. 80% and 90% daily footprint at the Edgy tower in 2022. Basemap credit: Maxar Technologies.

The omega factor was used as a coupling strength between the land and the atmosphere. A lower omega value indicates a stronger coupling with stomatal control. A higher omega value indicates a stronger decoupling with energy control (McNaughton and Jarvis, 1991). Left side is bouncer tower, and right side is main tower.
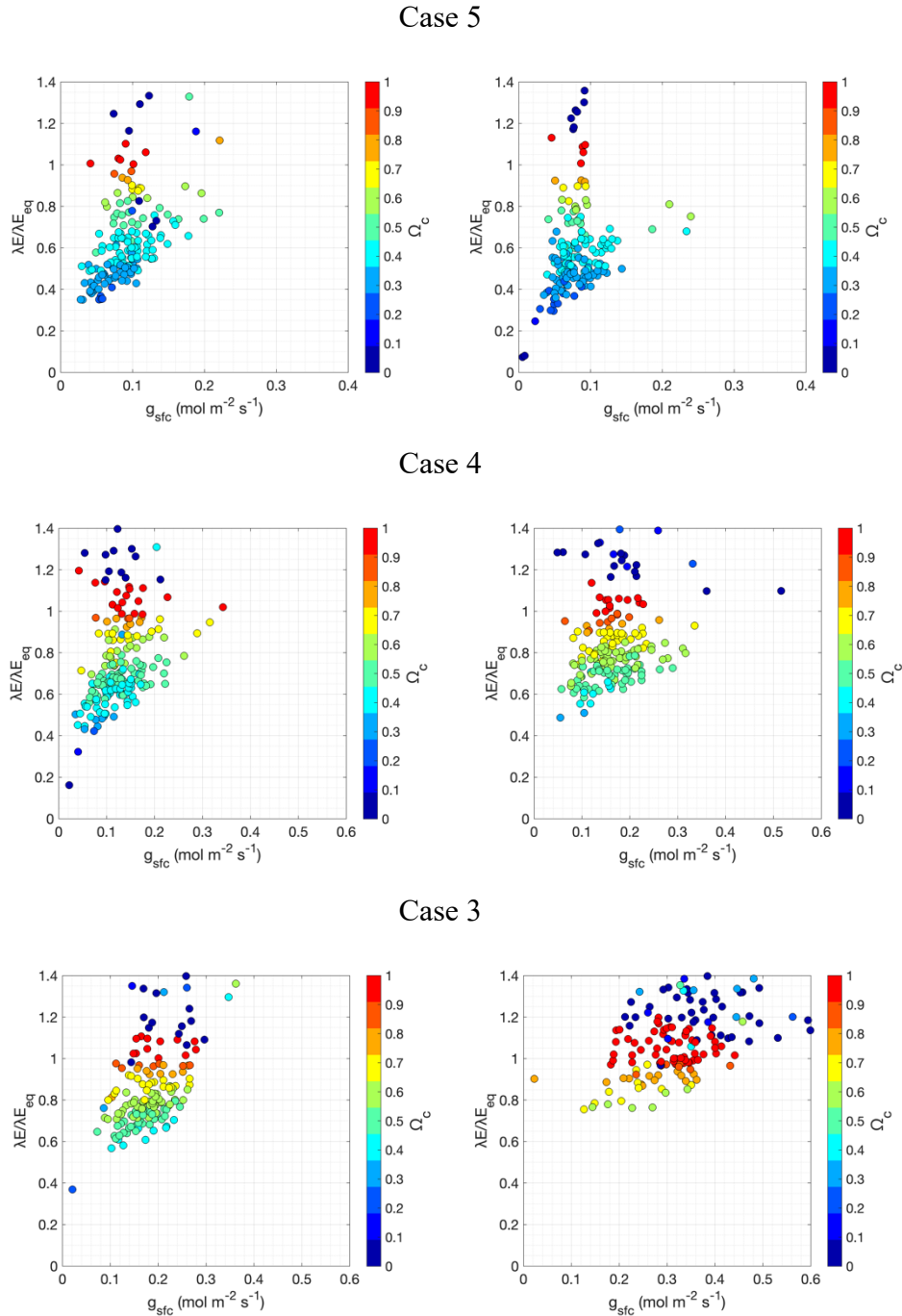
Case 5

Case 4

Case 3

Figure G1. Scatter plot of latent heat flux normalized by it equilibrium part (y-axis) and surface conductance (x-axis). The filled color indicates the coupling strength based on omega factor (z-

axis). Case 5 includes data from 2022-07-16 00:00 to 2022-07-23 23:30; Case 4 includes data from 2022-06-20 00:00 to 2022-06-28 23:30; Case 3 includes data from 2022-05-18 00:00 to 2022-05-25 23:30.

Appendix H: Intercomparison of sensors

To minimize potential errors from different sensors and ensure data quality, we conducted side-by-side intercomparisons as shown in Figure S1. It is important to acknowledge that each sensor may be different and behind our careful intercomparison still lies the question: which sensor is the truth sensor? Given that the reference sensor may be the biased one, or the different logistics one may take to conduct intercomparison, this document serves as an acknowledgement of the potential uncertainty in our measurements. Nevertheless, we used best judgement and calibrated the biased sensor accordingly.

Figure H1. Examples of the side-by-side intercomparison for temperature and relative humidity sensors used in 2021 (left) and sonic anemometers used in 2022 (right).

A. Intercomparison in 2021

Sonic anemometers

All sonic anemometers were tested and compared against each other prior to the 2021 field campaign (Table S1) from 2021-07-16 18:00 to 2021-07-19 07:30. From the intercomparison, measured mean horizontal wind speed ($\bar{u}$) and sonic kinematic heat flux ($\overline{w'T_s'}$) from different sensors agreed with the reference sensor measurement with $r^2 > 0.99$ and differences within 10%. In terms of the standard deviation of the vertical wind speed (σ_w), sensors from 2.42 m height of both bouncer and main towers compared well with the reference sensor. However, σ_w at 3.96 m height of the bouncer tower was systematically high by ~40%. **No calibrations** were applied to $\bar{u}$ since the measurements from other sensors agreed well with the reference sensor. However, for

$\overline{w'T_s'}$ at 2.42 m height of the bouncer tower, a calibration was applied to ensure a better representation of the vertical flux divergence calculation. Specifically, $\overline{w'T_s'}$ from 2.42 m height of the bouncer tower was reduced by 5% based on the regression shown in Table S1.

Table H1. Intercomparison of sonic anemometers used in 2021 campaign. $\bar{u}$ is the mean horizontal wind speed, $\overline{w'T_s'}$ is the sonic kinematic heat flux, and σ_w is the standard deviation of the vertical wind speed. The dark grey fill indicates out of spec.

	$\bar{u}$ (n=124)		$\overline{w'T_s'}$ (n=124)		σ_w (n=124)	
	Regression	r^2	Regression	r^2	Regression	r^2
Bouncer 3.96 m	0.97	>0.99	1.07	>0.99	1.42	>0.99
Bouncer 2.42 m	1.06	>0.99	1.01	>0.99	1.08	>0.99
Main 3.96 m	**Reference sensor**					
Main 2.42 m	0.94	>0.99	0.95	>0.99	0.98	>0.99

Temperature and relative humidity sensors

After the campaign in 2021, all temperature and relative humidity sensors were mounted on the main tower for side-by-side intercomparison (Figure S1, left) from 2021-11-05 15:00 to 2021-12-14 13:00. Some of these sensors were swapped during the campaign (Main 2.42 m, Bouncer 2.42 m, and Bouncer 3.96 m). We also included these sensors, before and after the swap, in the intercomparison (Table S2). From the intercomparison, all sensors were within spec, and **<u>no calibrations</u>** were applied to these measured variables.

Table H2. Intercomparison of temperature and relative humidity sensors used in 2021 campaign. $\overline{T}$ is averaged air temperature, and RH is relative humidity. Deployment dates reflect when the sensors were deployed in the field.

	Deployment dates	$\overline{T}$ (n=1681)		RH (n=1681)	
		Regression	r^2	Regression	r^2
Main 3.96 m	**2021-07-20 to 2021-11-05**	**Reference sensor**			

Main 2.42 m	2021-07-28 to 2021-09-03	0.95	>0.99	0.98	>0.99
	2021-09-03 to 2021-11-05	1.00	1.00	1.00	1.00
Bouncer 3.96 m	2021-09-03 to 2021-11-05	1.01	>0.99	0.99	1.00
	2021-07-28 to 2021-09-03	1.00	>0.99	1.05	>0.99
Bouncer 2.42 m	2021-09-03 to 2021-11-05	0.99	>0.99	1.00	>0.99
	2021-07-28 to 2021-09-03	**BAD SENSOR, DATA OMITTED**			

B. Intercomparison in 2022

Sonic anemometers

After the campaign, sonic anemometers and temperature/relative humidity sensors were mounted at the 3.96 m level of the main tower for intercomparison (Figure S1, right) from 2022-11-02 14:00 to 2022-11-30 14:30. For this intercomparison, we used the newest sonic anemometer (Bouncer 2.42 m) as the reference sensor. For $\bar{u}$, all sensors compared very well with the reference sensor with systematic differences within 5% and $r^2 \geq 0.99$, and **no calibrations** were applied to $\bar{u}$. For $\overline{w'T_s'}$, measurements at edgy (2.42 m), bouncer (3.96 m), and main (3.96 m and 6.00 m) all had underestimations for 15-19% but with good R^2 values. Given that sensors at the 3.96-m-height were used to investigate the flux evolution across towers (i.e., Fig. 9 in the paper), calibration was applied to $\overline{w'T_s'}$ at 3.96 m height of the bouncer and main tower. $\overline{w'T_s'}$ at this height of the bouncer tower was increased by 19% while $\overline{w'T_s'}$ at this height of the main tower was increased by 16% based on the regression shown in Table S3.

In term of vertical flux divergence, we did additional analysis for $\overline{w'T_s'}$, comparing the sonic anemometers at the main tower with the 3.96 m one as the reference sensor. The sonic anemometer at 2.42 m height underestimated $\overline{w'T_s'}$ by 18% ($r^2 = 0.93$) while the one at 6.00 m height underestimated $\overline{w'T_s'}$ by 15% ($r^2 = 0.89$). As a result, $\overline{w'T_s'}$ from 2.42 m height was

increased by 18% while $\overline{w'T_s'}$ from 6.00 m height was increased by 15% to account for the systematic differences.

Table H3. Intercomparison sonic anemometers used in 2022 campaign. $\bar{u}$ is the mean horizontal wind speed, $\overline{w'T_s'}$ is the sonic kinematic heat flux, and σ_w is the standard deviation of the vertical wind speed. The dark grey fill indicates out of spec.

	$\bar{u}$ (n=1345)		$\overline{w'T_s'}$ (n=1345)		Sigma w (n=1345)	
	Regression	r^2	Regression	r^2	Regression	r^2
Edgy 3.96 m	1.01	0.99	1.02	0.97	1.20	1.00
Edgy 2.42 m	0.97	1.00	1.15	0.98	0.94	0.88
Bouncer 3.96 m	0.99	1.00	1.19	0.99	1.20	0.99
Bouncer 2.42 m	**Reference sensor**					
Main 2.42 m	0.98	0.99	0.94	0.93	1.14	0.98
Main 3.96 m	0.96	0.99	1.16	0.94	0.95	0.97
Main 6.00 m	1.00	0.99	1.18	0.96	1.15	0.97

Temperature and relative humidity sensors

After the campaign in 2022, all temperature and relative humidity sensors were mounted on the main tower for side-by-side intercomparison from 2022-11-02 15:00 to 2022-11-30 14:00. From the intercomparison, all sensors were within spec, except for the relative humidity measurement at 3.96 m height of the Bouncer tower. **No calibrations** were applied to these measured variables. To elaborate, we did not calibrate the out of spec RH measurement here since it would not change any of the results presented in this paper. Both sensible and latent heat fluxes were

measured with eddy covariance instead of the variance-Bowen ratio technique. Additionally, for moisture advection, we derived specific humidity from the infrared gas analyzer instead of using the out of spec measurement.

Table H4. Intercomparison of temperature and relative humidity sensors used in 2022 campaign. $\overline{T}$ is averaged air temperature, and RH is relative humidity. The dark grey fill indicates out of spec.

	$\overline{T}$ (n=1343)		RH (n=1343)	
	Regression	r^2	Regression	r^2
Main 3.96 m	**Reference sensor**			
Main 2.42 m	0.99	0.99	1.00	>0.99
Main 6.00 m	0.99	0.99	0.99	>0.99
Edgy 2.42 m	1.01	>0.99	0.96	>0.99
Edgy 3.96 m	0.99	>0.99	1.03	>0.99
Bouncer 2.42 m	0.99	0.99	0.97	>0.99
Bouncer 3.96 m	0.97	0.99	1.04	>0.99

Appendix I: Deployed sensors

Table I1. Sensors used in this study as well as their location and corresponding data. The (+) sign indicates height above ground and (–) sign indicates depth below ground.

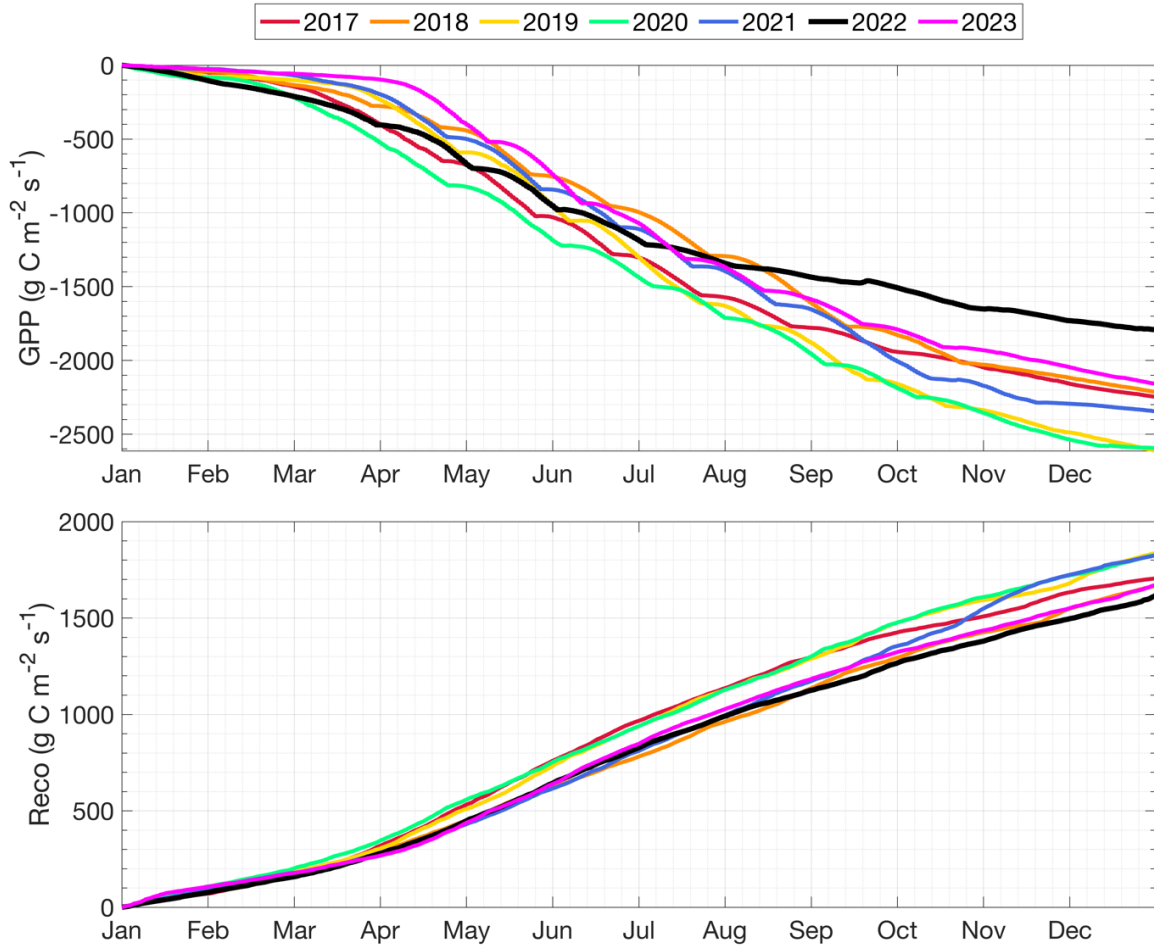| Sensor	Height (+) or depth (-)	Sampling frequency	Corresponding data
Sonic anemometer (WindMaster 1590)	+3.9 m	20 Hz	Sensible heat flux
Gas analyzer (LI-7500)	+3.9 m	20 Hz	Carbon and water fluxes
Net radiometer (NR-01)	+2.7 m	0.1 Hz	Net radiation
Temperature and Relative humidity (HMP155)	+3.5 m	0.1 Hz	Air temperature and relative humidity
Soil moisture (CS655)	- 0.02 m - 0.20 m	0.1 Hz	Soil moisture
Tipping bucket (TE525MM)	+3.5 m	0.1 Hz	Precipitation

Figure J1. Cumulative gross primary productivity (GPP) and ecosystem respiration (Reco) for each year from 2017 to 2023. The sharp decline in carbon uptake rates and steady respiration in 2022 motivated this study. Compared to other years, GPP accumulated very slowly after July in 2022.

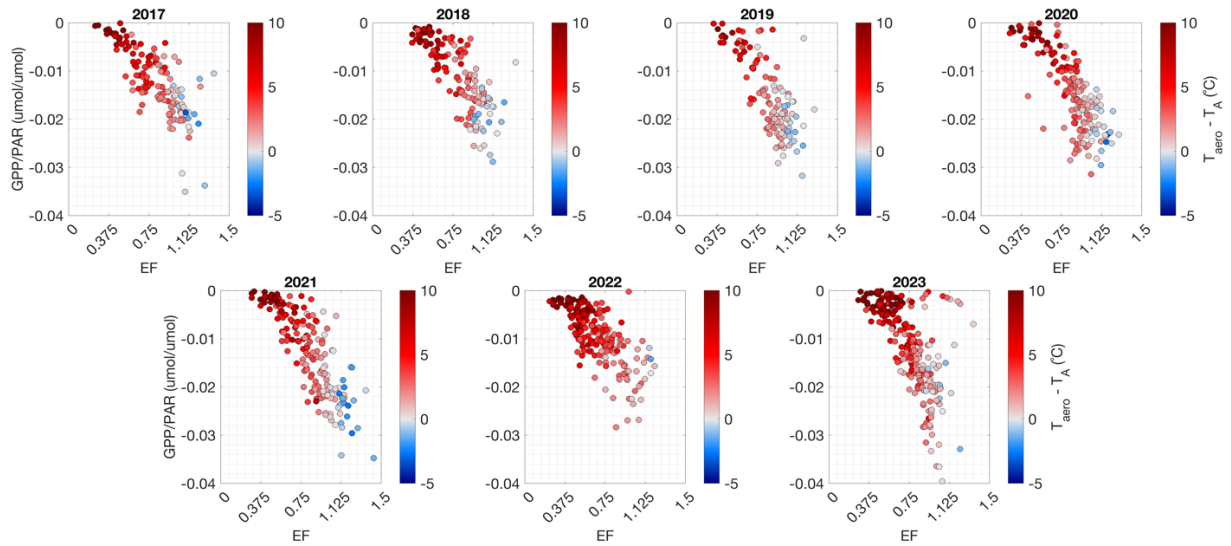Appendix K: Distribution of temperature gradient

Figure K1. Scatterplots of daily daytime (10:00 to 18:00) sum of gross primary productivity (GPP) normalized by photosynthetic active radiation (PAR) in micromole of CO2 per micromole of photon vs. evaporative fraction (EF) as a function of temperature gradient (colorbar) between aerodynamic temperature (T_{aero}) and air temperature (TA).
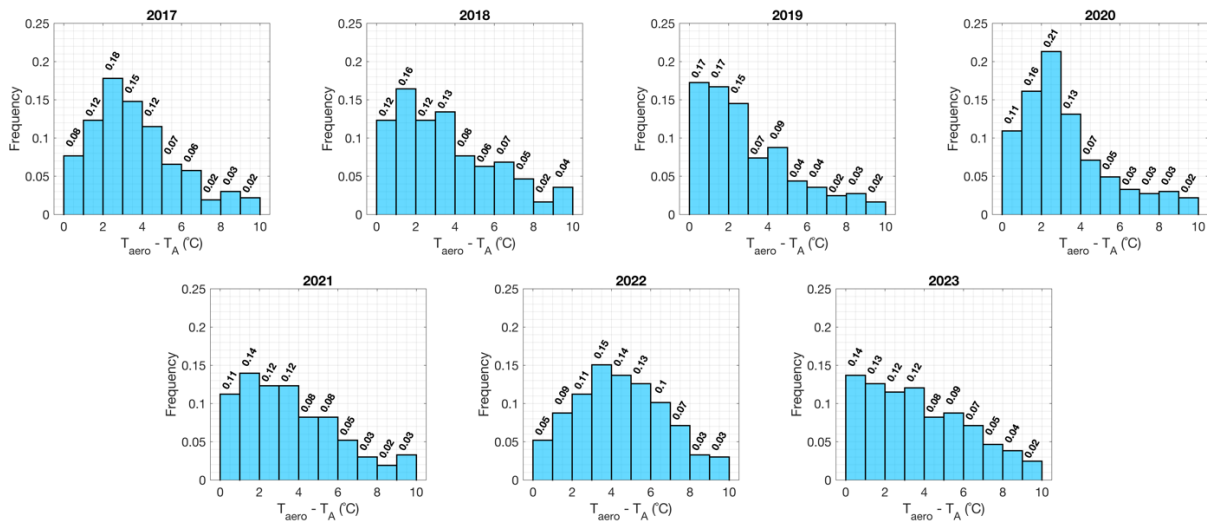

Figure K2. Histograms showing the interannual variability in temperature gradient shown as daily averages during daytime from 10:00 to 18:00 local time. ~50% of the days in 2022 had temperature gradients larger than 4 ºC, compared to 2017 (~32%), 2018 (~32%), 2019 (~24%), 2020 (~23%), 2021 (~29%), and 2023 (35%). The larger temperature gradient in 2022 enhanced sensible heat transfer from the biosphere to the atmosphere, yielding an overall high sensible heat flux in this year (Table 4).

Appendix L: Soil water potential from pedotransfer function

To inspect whether the alfalfa was under water stress, we used a pedostransfer function to compute the soil water potential -Ψ_S. Field samplings were conducted at the nearby site (Site ID: US-Bi2, Lat: 38.1991, Lon: −121.5351, DOI: https://doi.org/10.17190/AMF/1419513) to obtain the Van Gunutchen parameters. Although the soil texture between US-Bi1 (study site) and US-Bi2 (nearby site) are different, the main goal of this is to see if there were any significant differences in the magnitude and pattern of soil water potential. To calculate -Ψ_S, soil water retention curves (SWRC) were measured with HyProp and WP4C (METER Group, Inc. USA) to best represent the wet and dry ends of the SWRC, respectively. For saturated soil, water in HyProp was allowed to slowly evaporate while measuring soil tensions and mass. Unsaturated soils were removed from HyProp container, and two subsamples were selected. These subsamples were then transferred to WP4C sampling containers, where they were measured repeatedly until soil reached -15 MPa. Data from these measurements were compiled to form SWRC spanning entire spectrum of soil moisture condition. The Van Gunutchen parameters, including saturated soil moisture (0.6086926 cm^3 cm^{-3}), relative soil moisture (-0.4958455 cm^3 cm^{-3}), alpha (573.5568 1/cm), and n (1.099796), were then used to calculate -Ψ_S at the alfalfa site (Figure L1).
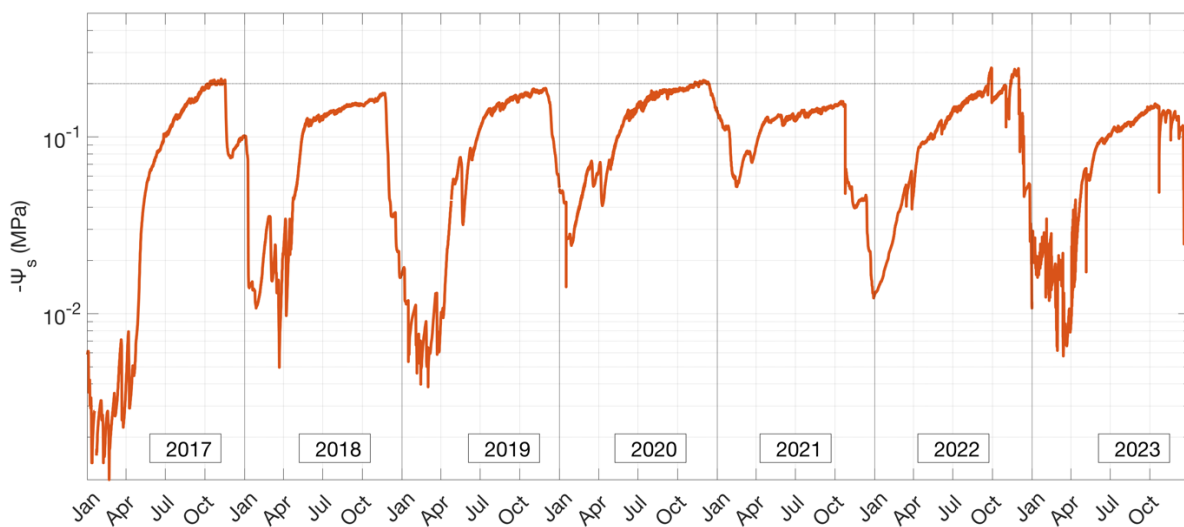

Figure L1. Time-series showing the interannual variability in soil water potential (-Ψ_S) at 20cm (orange).

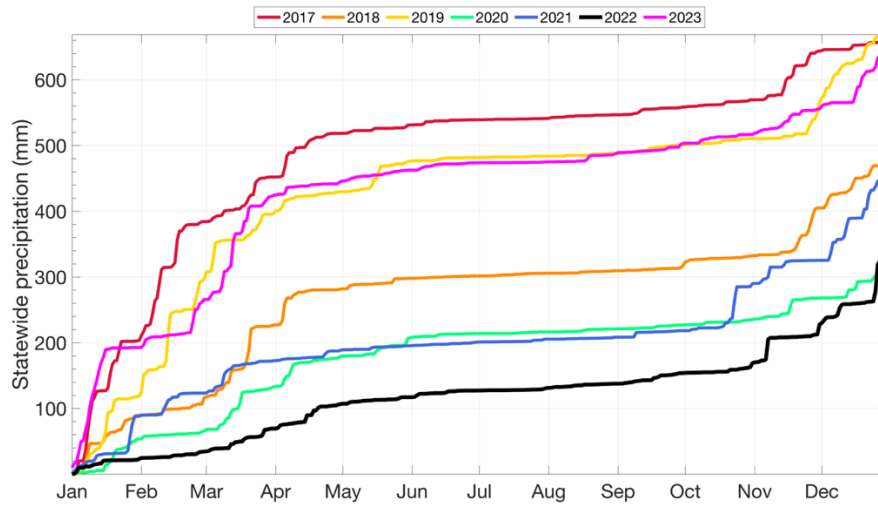Appendix M: Statewide and site level precipitation from 2017 to 2023

Figure M1. Cumulative statewide precipitation from 2017 to 2023. We used data from UCSB Rainfall Estimates from Rain Gauge and Satellite Observations (CHIRPS) on Google Earth Engine. Note that alternative statewide data can also be accessed from NOAA National Centers for Environmental information (https://www.ncei.noaa.gov/access/monitoring/climate-at-a-glance/statewide/time-series/4/pcp/ytd/0/2017-2023).
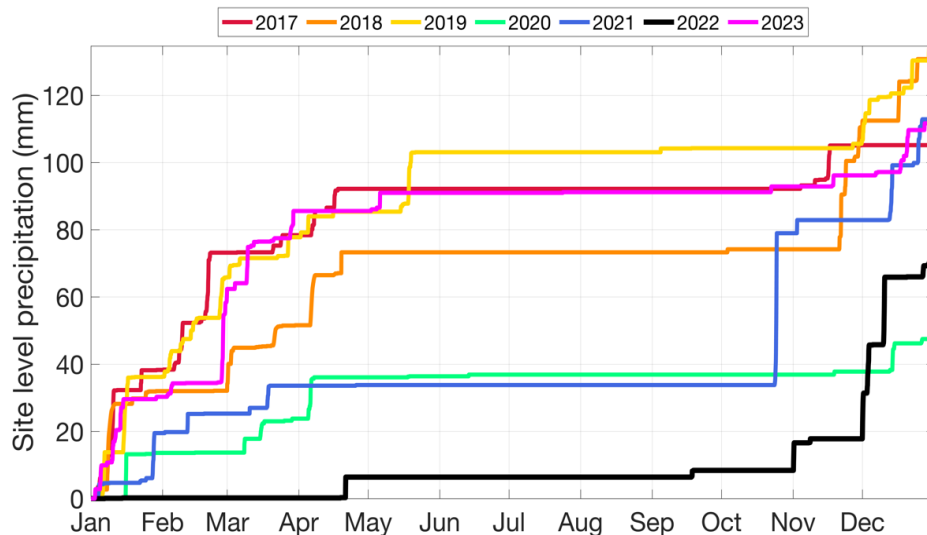

Figure M2. Cumulative precipitation at the alfalfa site from 2017 to 2023.